

Politecnico di Torino

Laurea Magistrale in Ingegneria Meccanica

A.A. 2017/2018



Analytical, numerical and experimental analysis of micro-cantilevers

Candidate

Antonio Montanarella

Supervisors

Alessandro Fasana

Fabrizio Scarpa

ABSTRACT

This thesis is focused on a study on vibrations of T-shape micro cantilevers produced for Micro Electro-Mechanical System (MEMS). The study was realized in a six months project (March 2017 – August 2017) at the University of Bristol (United Kingdom), in a collaboration between Departments of Mechanical engineering and Electronic engineering. It was completed in the last year at the Politecnico of Torino.

Micro cantilever beams were analyzed in multilayer configurations composed by 2 or 3 layers, made by Gallium Nitride, Aluminum Nitride and Silicon substrate. Some micro cantilever beams have been analyzed with a Laser Doppler Vibrometer (LDV) in Bristol University to obtain the first natural frequency. After checking the coherence of results through a Finite Element Model (FEM), the goal of this thesis was to obtain a mathematical model that calculates, as accurately as possible with a single formula, the first natural frequency.

The mathematical model was required by the electronic department of University of Bristol, because there was the necessity of a quick formula to obtain the first natural frequency, without resorting to prototypes, or slow methods such as FEM.

INDEX

1 MICRO ELECTRO-MECHANICAL SYSTEMS (MEMS)	3
- 1.1 Materials for MEMS technology	4
- 1.2 Basis manufacturing processes for MEMS	5
- 1.3 Applications of MEMS	10
2 GaN-BASED MICRO CANTILEVER BEAM	13
- 2.1 Characteristics of Gallium Nitride	13
- 2.2 Characteristics of Aluminum Nitride	16
3 FABRICATION OF GaN-based MICRO CANTILEVER BEAM	19
- 3.1 Fabrication of GaN-on-Silicon substrate	19
- 3.2 Gallium Nitride on patterned silicon (GPS) technique for GaN-based suspended cantilevers	21
- 3.3 Fabrication of T-shape GaN-based micro cantilever (3-layers configuration)	23
4 EXPERIMENTAL TESTS WITH LASER DOPPLER VIBROMETER (LDV)	26
- 4.1 LDV operating principle	26
- 4.2 Experimental test on micro cantilever with LDV	28
5 MATHEMATICAL MODELING OF THE FIRST NATURAL FREQUENCY	31
- 5.1 Determination of the mass “m”	33
○ 5.1.1 Mass in 2-layers configuration	34
○ 5.1.2 Mass in 3-layers configuration	35
- 5.2 Determination of the stiffness “k”	37
○ 5.2.1 Stiffness “k” in Bending 1	37
○ 5.2.2 Stiffness “k” in Bending 2	40
- 5.3 Determination of First Natural Frequency “ ω_{1f} ”	41
- 5.4 Determination of Equivalent Young’s	46
○ 5.4.1 Approximate method for equivalent Young’s modulus	47
○ 5.4.2 Controlling vibration using viscoelastic damping	48
▪ 5.4.2.1 Free layer treatments	49
▪ 5.4.2.2 Constrained layer damping treatments	51
○ 5.4.3 Oberst’s equation for equivalent Young’s modulus	54
▪ 5.4.3.1 First natural frequency in Bending 1 in 2-layers configuration implementing Oberst’s equation	57
▪ 5.4.3.2 First natural frequency in Bending 1 in 3-layers configuration implementing Oberst’s equation	59
▪ 5.4.3.3 First natural frequencies in Bending 2 implementing Oberst’s equation	60

6 COMPARISON OF RESULTS OF MATHEMATICAL MODEL, FEM AND EXPERIMENTAL TESTS.....	61
- 6.1 Modeling of the micro cantilever by Finite Element Model (FEM).....	61
- 6.2 Comparison of results between experimental tests, FEM and mathematical model.....	64
7 THE LIMITS OF THE MATHEMATICAL MODEL.....	67
- 7.1 Evidence with Euler – Bernoulli theory.....	67
○ 7.1.1 Euler – Bernoulli beam theory.....	67
○ 7.1.2 Correspondence between mathematical model, FEM and Euler – Bernoulli beam theory.....	70
○ 7.1.3 Calculation of the equivalent mass of “Cantilever 1.1”.....	73
○ 7.1.4 New mathematical model in “Cantilever 1.1” and comparison with FEM results.....	75
- 7.2 Calculation of the equivalent mass in T-shape cantilever.....	78
- 7.3 NEW mathematical model in T-shape cantilever.....	81
8 COMPARISON OF RESULTS OF NEW MATHEMATICAL MODEL, FEM AND EXPERIMENTAL TESTS.....	82
9 CONCLUSIONS.....	85
REFERENCES.....	86

1. MICRO ELECTRO-MECHANICAL SYSTEMS (MEMS)

Micro Electro-Mechanical System (MEMS) are microscopic system, nowadays used in electronic or mechanical micro devices. Their nanoscale version is Nano Electro Mechanical System (NEMS). In Europe MEMS are also called Micro System Technology (MST).

The first MEMS (Resonant Gate Transistor in *figure 1.1*) was realized by Harvey C. Nathanson (an electrical engineer) in 1965.

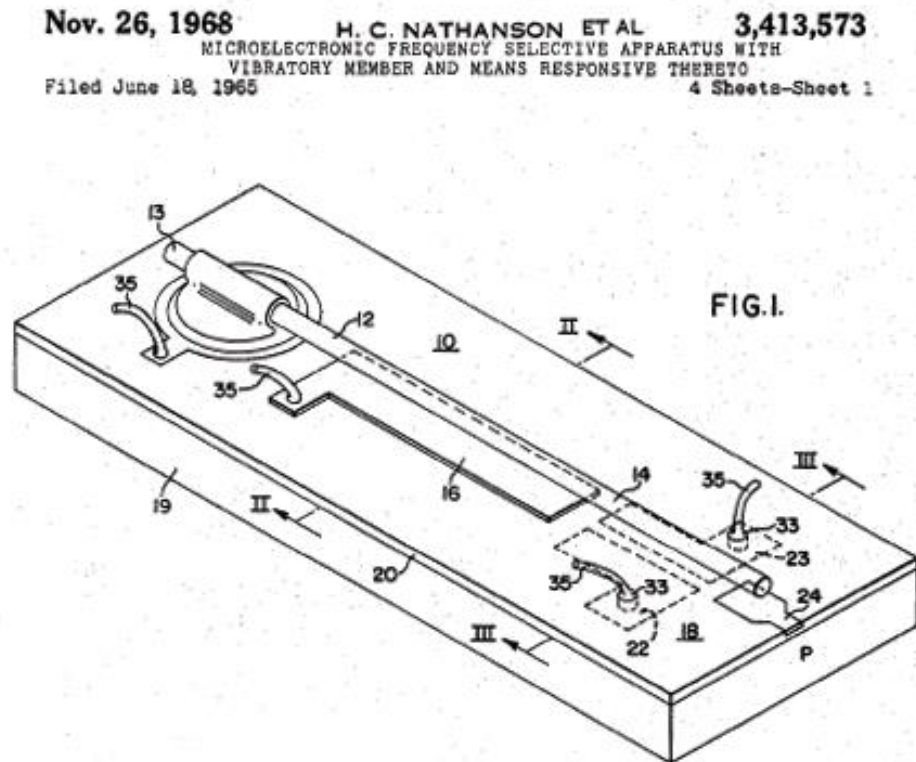


Figure 1.1 – Resonant Gate Transistor invented by Harvey C. Nathanson (source: Wikipedia.com)

His first MEMS was used as a tuner for microelectronic radios. It was developed by Robert A. Wickstrom and William E. Newell in Pittsburgh, PA, and patented as Microelectric Frequency Selective Apparatus.

Nathanson developed a method of batch fabrication where layers of insulators and metal on silicon wafers are shaped and undercut using masks and sacrificial layers. This process is the principal process in MEMS manufacturing. In 1973 Nathanson developed the use of million of microscopically small moving mirrors to create a video display, that now it is possible to observe in digital projectors.

Another pioneer of the MEMS technology was Raymond J. Wilfinger that patented an electromechanical monolithic resonator.

MEMS are made by components between 1 and 100 micrometers in size, while MEMS devices are generally in range from 20 micrometers to millimeter. Instead, MEMS arranged in arrays, could reach a dimension of 1000 mm² such as digital micromirror devices.

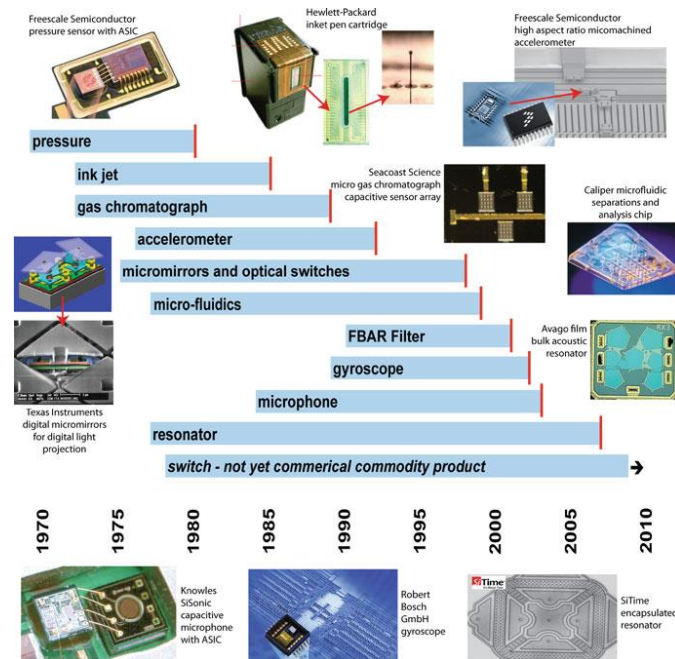


Figure 1.2 – Evolutions of MEMS technology from 1970 to 2010 (ref. 1.1)

These devices are considered as one of the most rising technology of the XXI century that revolutionized the world of electro-mechanical industry (in scheme 1.2 there is an evolution of MEMS technology from 1970 to 2010). MEMS are “smart” system that combine electronic, fluidic, optical, biological, chemical and mechanical management functions in very small dimensions, integrating sensors and actuators technology. They are characterized by a large surface to volume ratio. Due to this characteristic, the electromagnetic or fluid dynamic forces produced by the ambient require more design considerations than larger scale mechanical devices. MEMS technology is different from molecular nanotechnology or molecular electronics, because these must consider surface chemistry.

1.1 Materials for MEMS technology [ref. 1.1]

Generally, silicon is the material used to realize integrated circuits because it is an inexpensive high-quality material. Another advantage of silicon is that, it is considered as an almost perfect Hookean material. This characteristic guarantees no dissipation of energy during a hysteresis cycle, so it can provide a repeatable motion. In this way, it could have very long lifetimes (in a range of billions to trillions cycles without breaking). Nowadays polycrystalline silicon is used much in modern industry, but it is still relatively expensive. This is an advantage of silicon.



Figure 1.3 – Pure Silicon

Polymers are other materials used to produce MEMS because they can be produced in great volumes, with a huge variety of characteristics. This characteristic solves the problem occurring in silicon. MEMS made by polymers are often used for microfluidic applications, for example to realize blood-testing cartridges.

Metals are also used to realize MEMS. If they are used with some limitations, they can insure a high reliability. Silver, chromium, copper, aluminum, titanium, gold, tungsten, platinum and nickel are used commonly in MEMS applications.

The last category of materials used to realize MEMS are ceramics. Nitrides of silicon, aluminum, titanium, silicon carbide and other ceramics presents important advantage about mechanical properties. For example, the AlN is a material used to realize particular types of MEMS. In fact, due to its characteristic to crystallize in wurtzite structure, AlN could have piezoelectric and pyroelectric properties. For example, it is possible to realize micro-sensors sensitive to shear forces.

Another ceramic material is TiN that presents a high elastic modulus, electrical conductivity, and resistance against biocorrosion. These characteristics, especially the last, make TiN available for applications in biosensors and biogenic environments.

1.2 Basis manufacturing processes for MEMS [ref. 1.1]

The basis processes used to realize MEMS in modern industry are “Deposition processes”, “Patterning” and “Etching processes”:

- DEPOSITION PROCESSES: This process deposits thin films of material with thicknesses between 1 to 100 micrometers. This process is used also in manufacturing of NEMS. In this case, thicknesses consist in deposition films from 1 nanometers to 1 micrometers. The Deposition processes are:
 - PHYSICAL VAPOR DEPOSITION (PVD): This technique uses the sputtering process, where an ion beam releases atoms from a target, moving them in space until they deposit on a surface that represents the substrate, and the evaporation process from a target to substrate using thermal evaporation or electron beam evaporation in vacuum condition;
 - CHEMICAL VAPOR DEPOSITION (CVD): This technique consists in a reaction of a gas on a substrate to permit the growing of material. There are techniques of PECVD (Plasma-enhanced chemical vapor deposition in *figure 1.4*) and LPCVD (Low Pressure chemical vapor deposition in *figure 1.5*)

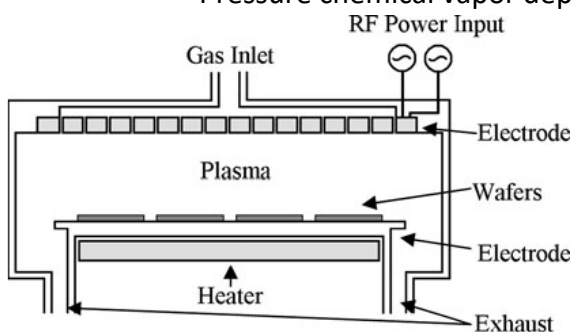


Figure 1.4 – Schematic diagram of PECVD system (1.1)

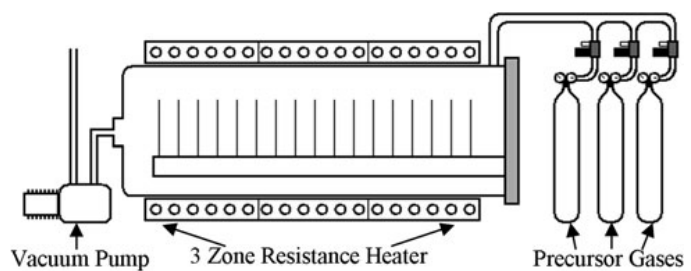


Figure 1.5 – Schematic diagram of PECVD system (1.1)

- **PATTERNING:** It is a process where a pattern is transferred into a material. It groups different processes:

PHOTOLITHOGRAPHY: A patterning process that uses a photosensitive material (a material that changes its physical properties when exposed to a radiation). If this photosensitive material is selectively exposed to a light, using for example a masked surface, it transfers a pattern to underlying surface, defining the desired pattern. A scheme of photolithographic elements and photolithographic process is showed in *figure 1.6*:

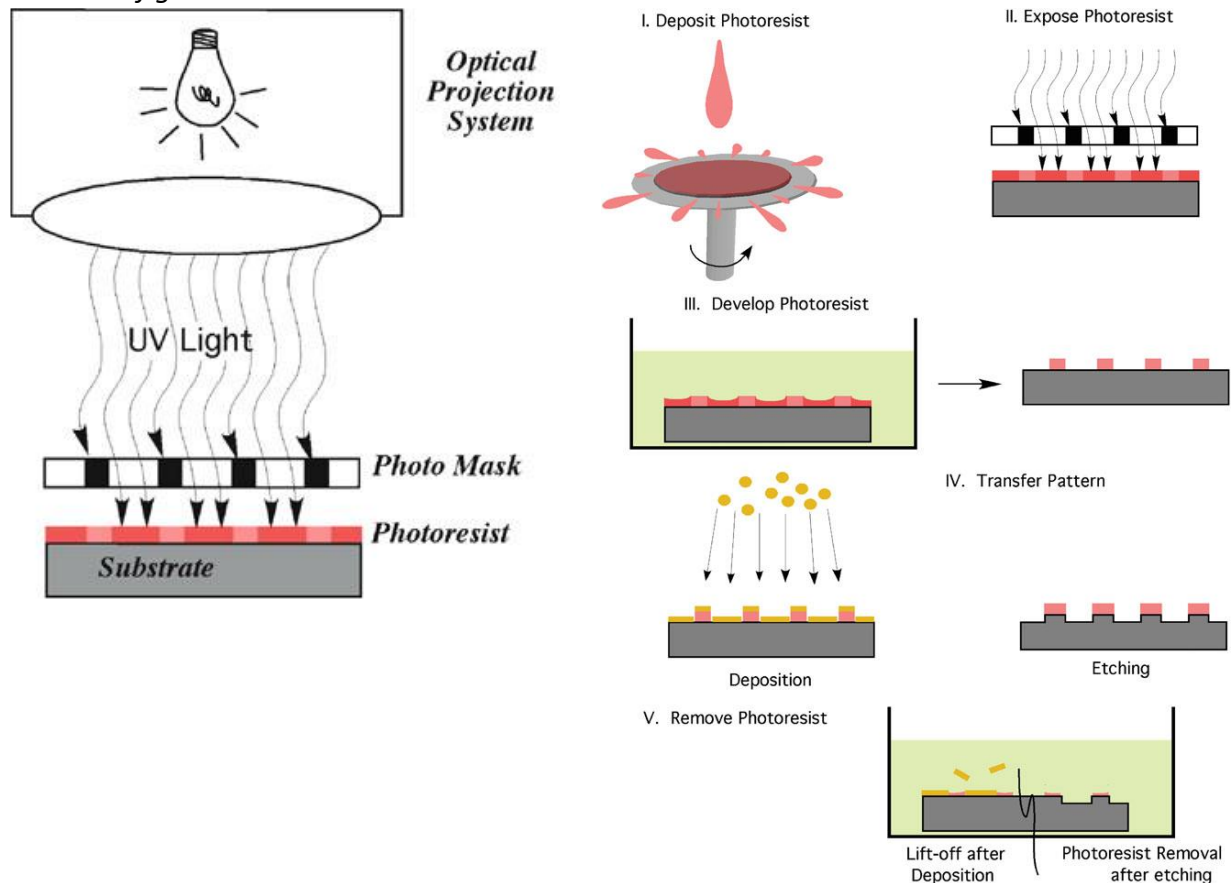


Figure 1.6 – Scheme of photolithographic process (ref. 1.1)

This is a two-dimensional method to produce MEMS. It could be repeated many times to produce various devices. Photolithography is typically used with metals, and for fabrications of transistors on a silicon substrate.

- **ELECTRON BEAM LITHOGRAPHY:** This technique uses electrons to expose a “resist” layer. Scanning a beam of electrons, it is possible to draw shapes on a surface covered with a film called “resist”. Due to that, the solubility of the resist changes, permitting a selective removal of exposed or non-exposed regions of the resist with a solvent. The goal of this technique is to create micro or nano structures in the resist film that could be transferred on a substrate material, often by etching. The resolution of this technique is 10 nm, but this method to produce pattern is very expensive. A scheme of e-beam lithography is showed in *figure 1.7*:

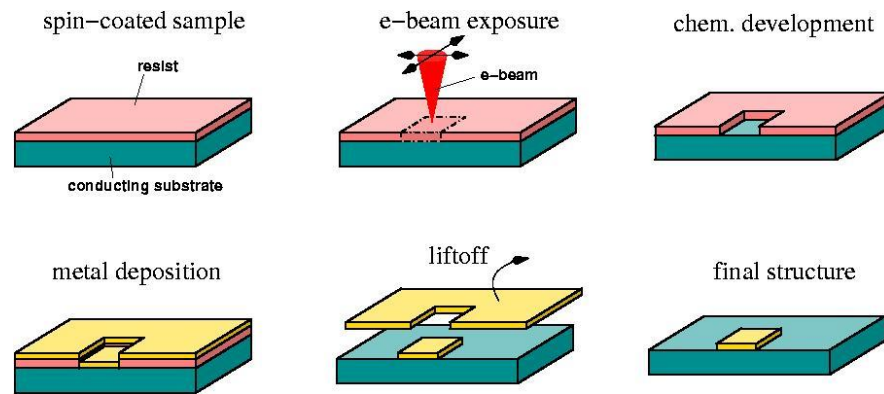


Figure 1.7 – E-beam lithography steps (source: http://nanooptics.uni-graz.at/ol/work/m_ebl.html)

- ION BEAM LITHOGRAPHY: A practice that provides a scanning of a focused beam of ions in a pattern across a surface. This method presents a fine resolution, more than other patterning method. The process is similar to electron beam lithography, but in this case, it uses ions. Ions move in straighter paths than electrons through vacuum but also in matter. Therefore a high resolution is guaranteed.
- ION TRACK TECHNOLOGY: A technology that uses the Ion Tracks, that are damages created by a swift heavy ions that penetrate in a solid. It is a deep cutting tool, that could generate holes with a resolution limit around 8 nm. This technique can realize devices with defined inclination angle.
- X-RAY LITHOGRAPHY: Similar to photolithography, where it is possible to selectively remove parts of a film. To transfer a pattern from a mask to a substrate, this method uses X-rays. Later some chemical treatments engraves produced pattern into the material under the photoresist. In *figure 1.8* there is a scheme with 6 steps to realize a MEMS. The mask is realized with a transparent membrane and a metal absorbing pattern and brought to a conductive substrate that is coated by a X-ray photoresist material. Later, X-ray radiation affects the resist, and after a developing of material, metals are inserted in the mold. After the material is removed and metal mold parts are ready to be assembled.

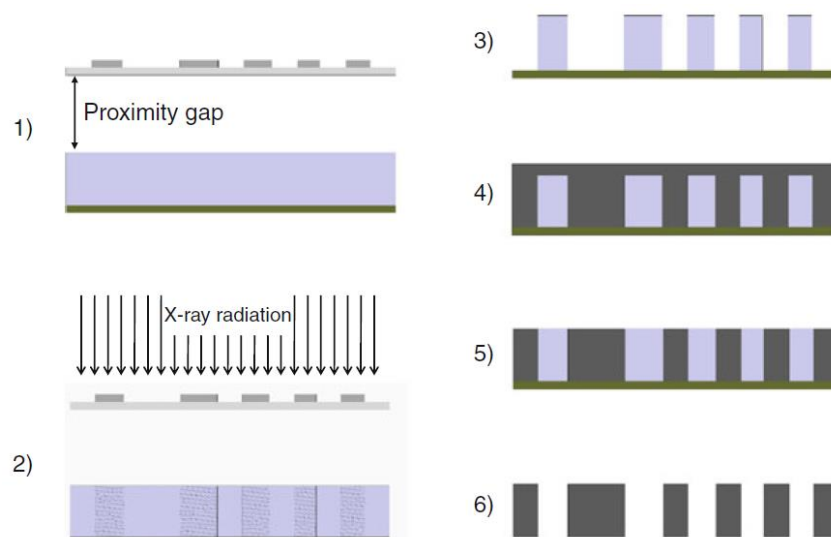


Figure 1.8 – X-ray lithography scheme (ref: 1.1)

- DIAMOND PATTERNING: A technique where it is possible to create MEMS made by diamond. It is a method that avoids to damage the diamond. The patterns can be formed by selective deposition using a silicon dioxide mask. There is a lithographic application of diamond films on a substrate.
- ETCHING PROCESSES: A method that chemically removes layers from a surface. In the first steps, the pattern is protected from a masking material that resists etching. In many cases, the etching process is used subsequently a photolithography process. For example, the etch could make a cavity into a material. The thickness of cavity could be controlled using both the etching time and the etch rate. In other cases, etching process is used to remove a whole layer of a multilayer without damaging the underlying layers. Furthermore, it is possible to realize cavities with oblique sidewalls. The distance of undercutting is called *bias*. If an etchant presents a large bias, it is defined isotropic, because it erodes the substrate in all direction on space. In modern industry, anisotropic etches are preferred because it is possible to produce controlled patterns. Etching processes include two macro technologies that are Wet Etching and Dry Etching:
 - WET ETCHING: In this technology a liquid etchants is used. The wafer is completely immersed in etchant and, to obtain optimal results, it must be agitated. An example of largely used etchant in this process is the hydrofluoric acid (BHF) that is used principally to etch silicon dioxide. Instead of submerging the entire wafer, it is possible to use the Bernoulli principle, where a gas (nitrogen) is used to protect a side of a wafer, while the other side is immersed. A scheme of wafers in etch bath and later in rinse bath is showed in *figure 1.9*:

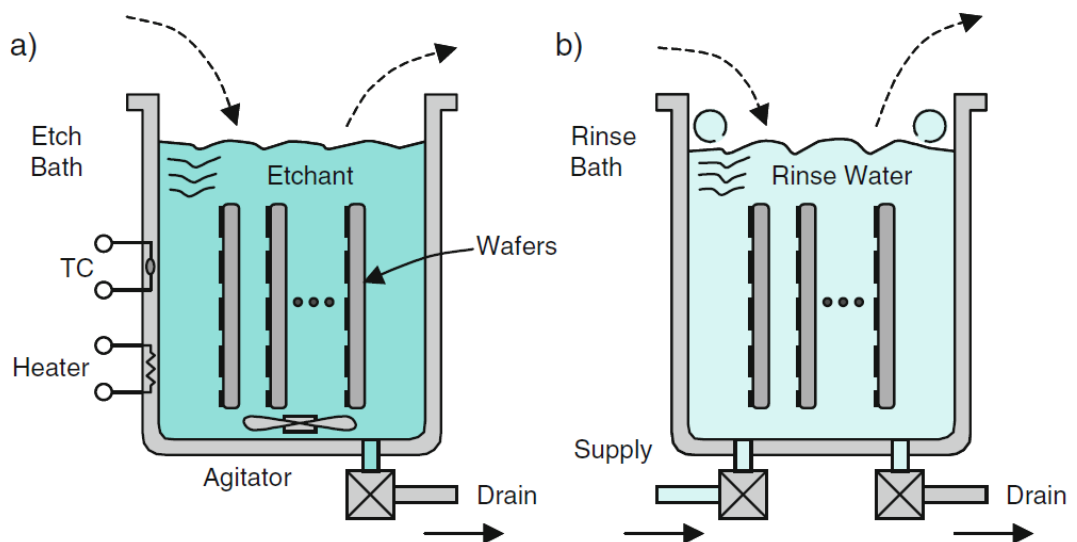


Figure 1.9 – Wafers in Etch bath (a) and later in Rinse bath (b) (ref: 1.1)

Often, these processes are isotropic, because these etchants are characterized by a large bias. This characteristic produces large amount of toxic waste. The most important Wet etching processes are isotropic etching, anisotropic etching, HF (hydrofluoric) etching and electrochemical etching;

- **DRY ETCHING:** A process often useful for semiconductors that are chemically resistant to wet etching. The materials where this process is more used are Silicon Carbide and Gallium Nitride. It is a process that removes parts of a material often using a bombardment of ions actuated by a plasma made by very reactive gases, such as fluorocarbons, oxygen, chlorine, boron trichloride with a mix of non-reactive gases such as nitrogen, argon or helium. Typically, dry etching processes are anisotropic.

Dry etching is used with photolithographic process to remove some part of a semiconductor to form for example contact holes that electrically communicate with underlying substrate, and via holes that can guarantee connection in conductive layers of a multilayer MEMS.

The most common Dry Etching processes are Vapor etching, Xenon difluoride, Plasma etching and Reactive-ion etching (RIE). The RIE configuration is showed in *figure 1.10*:

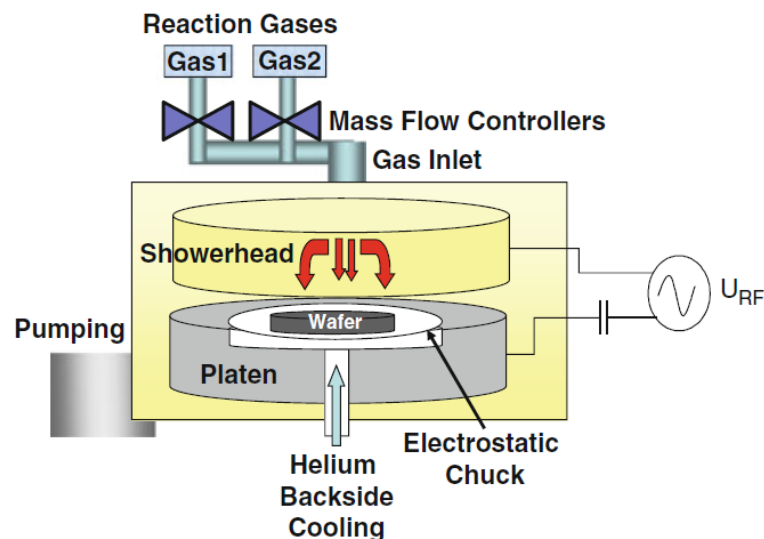


Figure 1.10 – Scheme of RIE configuration (ref: 1.1)

After a large number of MEMS are realized on a single silicon wafer, they must be separated. The processes that deals with this are “Die Preparation”. In these processes, there are “Wafer backgrinding” that reduce the wafer thickness, “wafer dicing” and a dry laser process called “stealth dicing”.

The MEMS manufacturing technologies are:

- **BULK MICROMACHINING:** Realizes structures using a selective etching inside a substrate. The substrates often are made by silicon wafers, so it is possible to use a anisotropic wet etching process, to form structure with an high precision. After an exposition using a photolithography to transfer a pattern from a mask to a surface, the silicon is dissolved from wet etchants such as Potassium hydroxide (KOH) or tetramethylammonium hydroxide (TMAH) that are alkaline liquid solvents. It is also possible to use wet etchants for this technology. But the wet etchant presents some advantages because the silicon has a crystal structure, so its atoms are arranged in periodically in planes or lines. This method is often used to realize grooves with angled walls or V-shape grooves, due to its precision.

Bulk micromachining technique is principally used to create micro pressure sensors. Bulk micromachining manufacturing technologies are often inexpensive.

- **SURFACE MICROMACHINING:** It builds microstructures by deposition of layers on a substrate that is structural material, and after etching them by a pattern. It is different from bulk micromachining, where a silicon substrate wafer is selectively etched to produce structures, while in surface micromachining a material is added to a structure layer, and later it is selective removed. The structures are built on a substrate and not inside it as in bulk micromachining. Polysilicon is often used as a substrate layers and silicon dioxide is used as sacrificial layer that later will be removed to create for example groove in thickness direction. This technology has the ability to build electronic and mechanical components on the same substrate. The components realized with this technology are smaller if compared to bulk micromachining components.
The difference between surface micromachining and bulk micromachining permits to substitute the silicon wafer by a cheaper substrate like glass or plastic.
“Surface micromachining” permits to realize low-cost micro accelerometers that are often used in automotive application, for example in realization of air-bag systems, or it is used to realize thin-film transistors on large glass, for example to realize displays.
- **HIGH ASPECT RATIO (HAR) SILICON MICROMACHINING:** A technology that combines the good performance of Bulk micromachining with comb structures and in-plane operations of surface micromachining. In HAR silicon micromachining the thickness can be in a range from 10 to 100 μm . In HAR silicon micromachining are often used polycrystalline silicon, and bonded silicon-on-insulator (SOI) wafers. Typically, HAR silicon micromachining is not used to realize integrated circuits.

1.3 Applications of MEMS [ref. 1.1]

The most important applications of MEMS in modern technology are in physical, chemical, biological and medical technology (in *figure 1.11*)

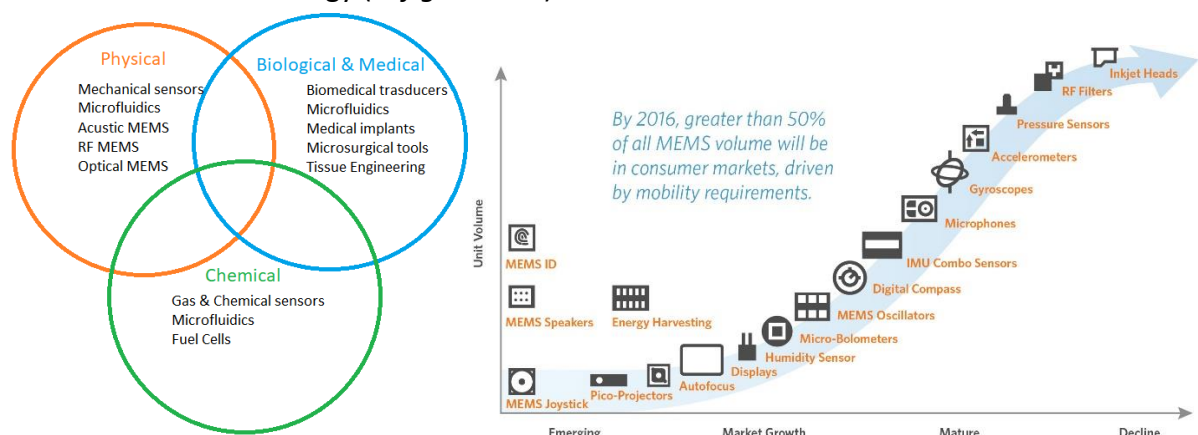


Figure 1.11 – Physical, chemical and Biological-medical applications, and Unit volumes in function of productions of MEMS in modern industry

- **ACCELEROMETERS:** realized in MEMS both in automotive technology, for example to realize air-bag technology, or electronic stability control. Accelerometers are diffused also

in consumer electronic, for example there are MEMS in game controllers, cell phones and digital cameras. These accelerometers are also used in PC to hide the hard disk head during a free-fall. In this way, it is possible to prevent damage and data loss.



Figure 1.12 – MEMS accelerometer (Pyroelectro.com)

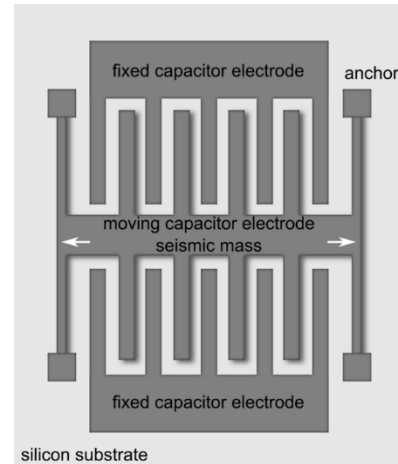


Figure 1.13 –Scheme of MEMS accelerometer (innomic.com)

- INKJET PRINTERS: Uses piezoelectric or thermal bubble ejection to deposit ink on paper.

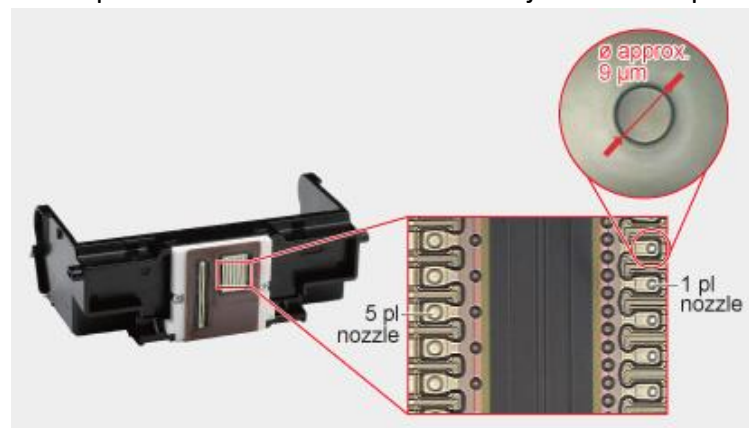


Figure 1.14 – Inkjet print-head nozzle (source: canon.com)

- MICROPHONES: All microphones in portable devices, mobile phones are made by MEMS.

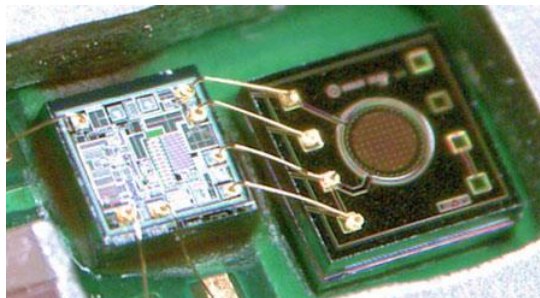


Figure 1.15 – A MEMS microphone (ref. 1.1)

- PRESSURE SENSORS: Realized for car tire pressure sensors or blood pressure sensors.
- DISPLAYS: or digital micromirror device (DMD) or chip in projectors.
- ULTRASOUND TRASDUCER;
- INERTIAL MEASUREMENT UNITS (IMUs): Includes accelerometers or MEMS gyroscope to control helicopters, planes and drones. These MEMS could balance the flight in roll, pitch and yaw. They could be used also for an autopilot of an airplane;

- BIO-MEMS: there are biosensors or chemosensor in medical and health devices. Some bio-MEMS are present in very innovative devices such as MEMS defibrillator (figure 1.16), MEMS hearing-aid transducer (figure 1.17) or Sensimed's Triggerfish™ implantable MEMS (figure 1.18). The latter is an implantable MEMS pressure sensor that is used to monitoring glaucoma evolution in patients. It is composed by a contact lens with a MEMS pressure sensor element, a loop antenna (golden rings) and a small microprocessor. This device measures how corneal curvature changes in response to intraocular pressure (IOP).

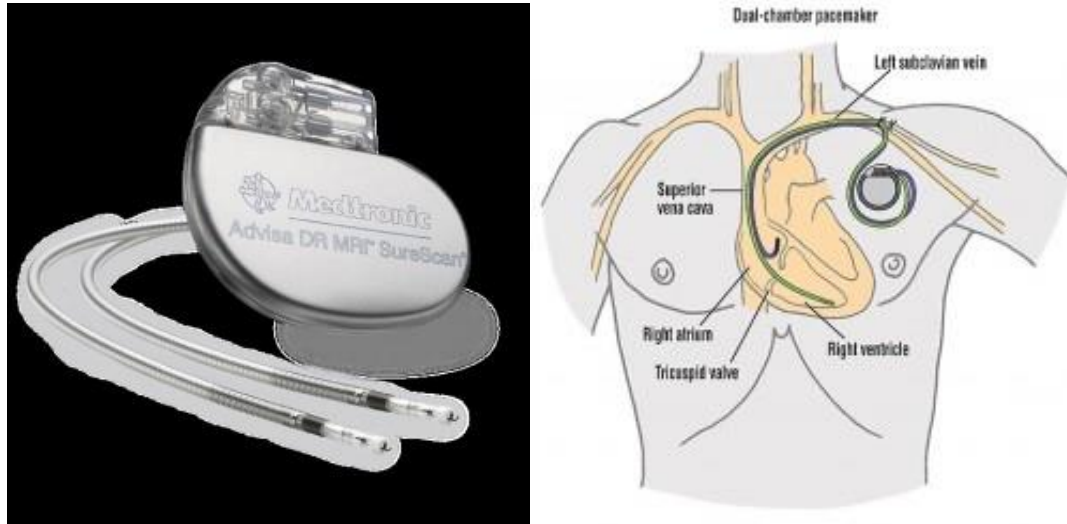


Figure 1.16 – MEMS defibrillator (source: electroiq.com)



Figure 1.17 - MEMS hearing-aid transducer (source: analog.com)

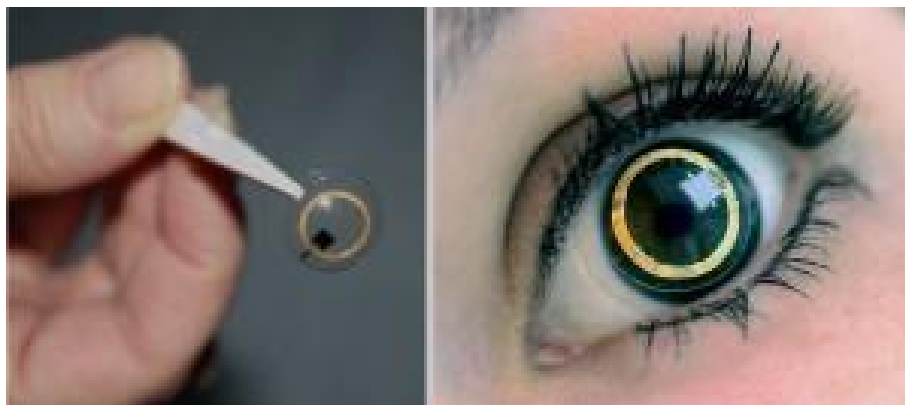


Figure 1.18 - Sensimed's Triggerfish™ implantable MEMS (source: sensimed.com)

2. GaN-BASED MICRO CANTILEVER BEAM

The micro cantilevers treated in this thesis will be analyzed in this chapter from a chemical point of view, explaining the characteristics of their constitutive materials. The cantilevers will be treated in multilayer configuration, in particular in 2-layers and 3-layers. 2-layers configuration presents Gallium Nitride and Silicon, while 3-layers configuration presents Gallium Nitride, Aluminum Nitride and Silicon. The materials are considered perfectly bounded.

These cantilevers are produced to realize micro sensors, and they are mechanically single supported beam structures, often manufactured from silicon. These sensors respond to physical changes, due to chemical or biological interactions occurring in their free end. Current cantilever sensor systems are realized in MEMS or NEMS. For example, these devices could be used to create an electronic nose, for example to mimic a dog nose, to detect the volatile elements and vapors. The use of these cantilevers principally refers to biological and chemical field of applications. These sensors are highly sensitive, and could detect biomarkers from small sample quantities, despite the fabrication techniques affect the sensitivity and create surface stress on sensors. In MEMS applications, when these sensors are excited by an external disturbance, the micro cantilever of the sensor bends. These bending moments are electronically detected by a change in resistance of doped silicon piezoresistor. Alternatively, the bending moments could be detected by a laser-detector system. Instead, in NEMS applications, these micro sensors are incorporated into lab-on-a-chip devices, and they could be used to monitor minuscule biomolecular interactions, for example to aid early diagnosis of diseases. There are also electrical and optofluidic biosensors in nanoscale.

The studies conducted until now, represents nanosensors with either silicon or silicon nitride, and not Gallium Nitride (GaN). The idea of incorporating GaN cantilevers at the nano and microscale level is a new field of interest that is still being researched.

2.1 Characteristics of Gallium Nitride

The recent interest in MEMS realized in GaN on Silicon(111) has been motivated by the characteristic of silicon, that is less expensive than Silicon Carbide technology, that has a great importance in fabrication of III-nitride light emitting devices (LED).

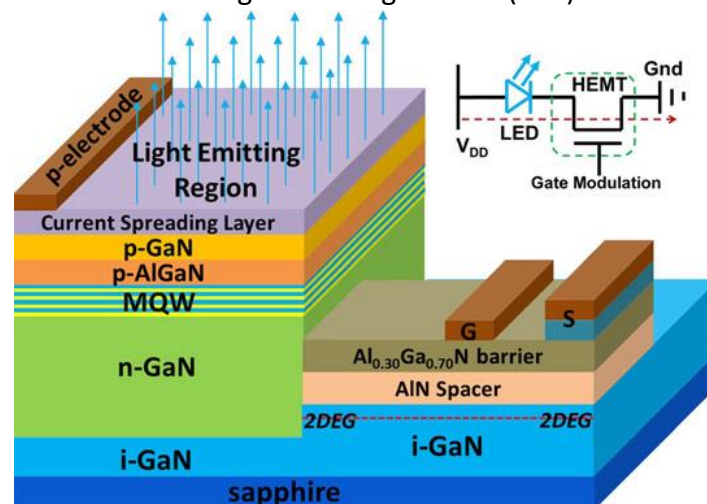


Figure 2.1 – Scheme of Light Emitting Diodes (source: semiconductor-today.com)

A scheme of a LED made by GaN is showed in *figure 2.1*.

The advantage to use GaN is to integrate it in an established silicon process technology. In this way, the characteristics of piezoelectricity and piezoresistivity of III-nitrides could be used in silicon MEMS. The problem of fabrication of GaN-based MEMS devices is the etching associated with GaN. In fact, it is chemically stable and insoluble in most common etchants at room temperature. Anisotropic etching is crucial in fabrications of these MEMS devices. Wet chemical etching of GaN, that slowly produces isotropic etch profiles, makes devices undesirable for commercial applications. Dry etching is a better alternative because it is an anisotropic process. Until now, fabrications of GaN were focused just on GaN grown on sapphire substrates. These fabrications use wet photoelectrochemical etching to reduce GaN removing the sacrificial interlayers.



Figure 2.2 – Beam of Gallium Nitride (source: Wikipedia.com)

Gallium Nitride (in *figure 2.2*) is a hard, ceramic, transparent, piezoelectric semiconductor material and presents a chemical inertness and large band gap. These characteristics make the GaN perfect for harsh environment applications. Due to its piezoelectric property, GaN can be used for example in piezoelectric actuation systems. They have a higher efficiency than actuation systems that actually work through capacitive, thermal or magnetic characteristics. GaN is capable of withstanding high temperatures, and it is an optoelectronic material due to its direct band gap in blue region of the visible electromagnetic spectrum. It is also transparent from the visible to the mid-infra-red part of the spectrum. In fact, GaN is the basis of most blue light emitting devices such as LEDs and lasers. Furthermore, these cantilever systems could also incorporate light sources, for example to be useful as light guides along the length of cantilevers.

In ambient conditions, GaN crystallizes in a hexagonal wurtzite structure showed in *figure 2.3*:

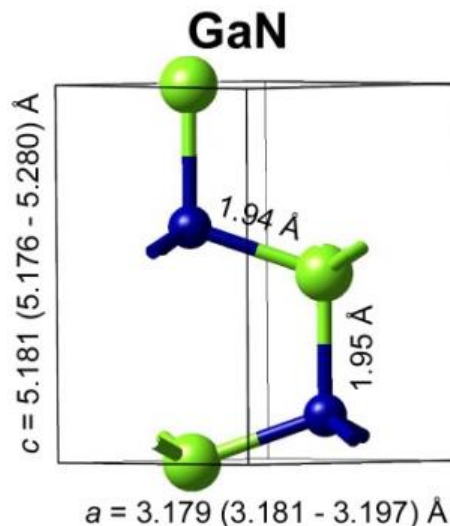


Figure 2.3 – Hexagonal GaN Wurtzite

As regards mechanical characteristics, in comparison to silicon, GaN has a higher elastic modulus. Mechanical properties of GaN were taken from a study in [ref. 2.1] where a layer of 1,5 μm of GaN was analyzed by an iterative process of experimental and simulation data due to difficulty of its analytical calculation. In experiment, the load-displacement was applied on a double-anchored cantilever. It was used a double-anchored cantilever, because in a single anchored cantilever, when the surface reaches a certain bending angle, the needle selected to apply the load would slip off the surface.

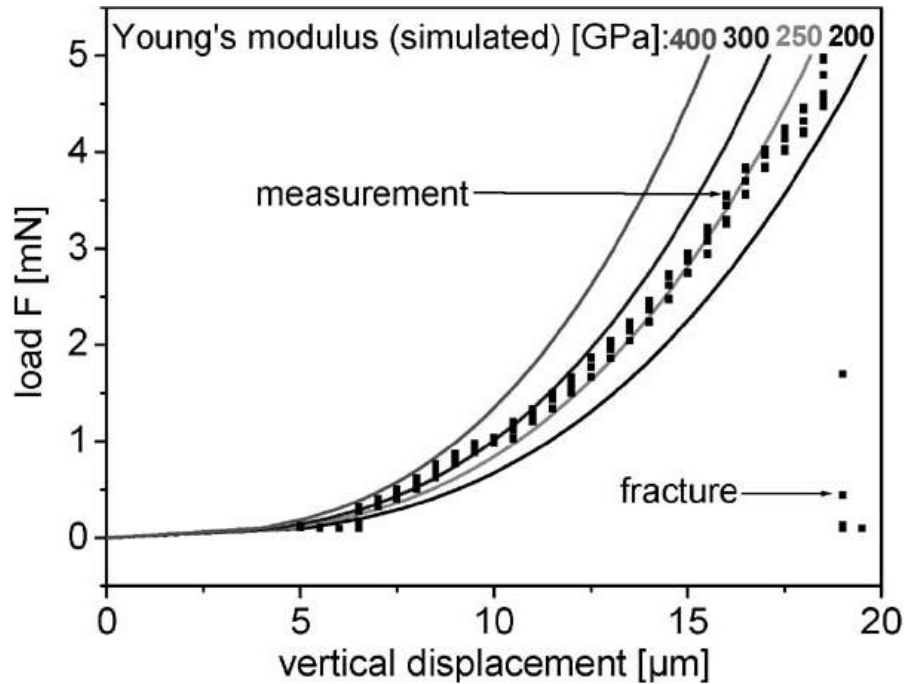


Figure 2.4 – Load-displacement experiment [ref. 2.1]

In graph in *figure 2.4*, each curve represents a different simulation with a different elastic modulus. Comparing the theoretical curve with experimental data, the estimated Young's Modulus results approximately 250 GPa as showed in *figure 2.4*. The fracture of the cantilever occurred around 350 MPa as showed in *figure 2.5*:

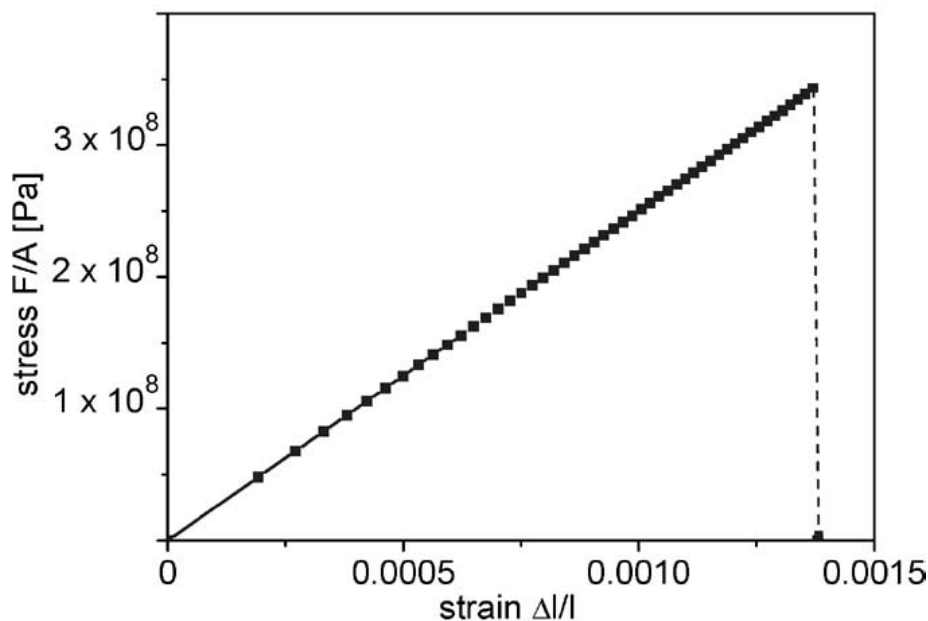


Figure 2.5 – Stress-strain curve of experiment [ref. 2.1]

GaN-on-silicon microcantilevers in this thesis will be evaluated in dynamic studies, in order to determine their first natural frequency. Before the studies in this thesis, different shaped cantilevers were designed to obtain resonance frequencies lower than 500 kHz, in order to meet the requirements of Bristol based laser Doppler vibrometry systems. These results are a first step to produce nanoscale opto-electro-mechanical based sensors system, potentially with integrated light sources and detectors.

As regards density of GaN, the value of 6150 kg/m³ was used.

2.2 Characteristics of Aluminum Nitride

The Aluminum Nitride (AlN) crystallizes in wurtzite structures, in hexagonal space. Therefore, its principal phase is Wurtzite (w-AlN). In nitrogen atmosphere, AlN presents a melting point and sublimation of 2000 °C and it has a Mohs hardness of 9.

Aluminum Nitride is a ceramic material, it has a large bandgap (6.2 eV), and it has an excellent thermal conductivity (180 W/mK), which makes it a substrate with high performances in electronics, because it is an electric semiconductor, but an excellent heat conductor. The particularity is that when the heat is effectively transported, aluminum nitride is not a good electrical conductor.

The main applications of aluminum nitride are defined in the field of electrical conductivity. Experimental studies focused mainly on wurtzite phase, in fact, the high bandgap of AlN, makes it as the only direct gap semiconductor containing a significant amount of aluminum from a technological point of view. Among semiconductors, AlN possesses the largest energy gap. In modern studies the attention is focused on Al_xIN_{1-x}N (x=0,83). This material presents the same reticular step of GaN. The structure is showed in figure 2.6. In experimental studies on AlN/GaN compounds, there is a bending of bandgap comparing with GaN.

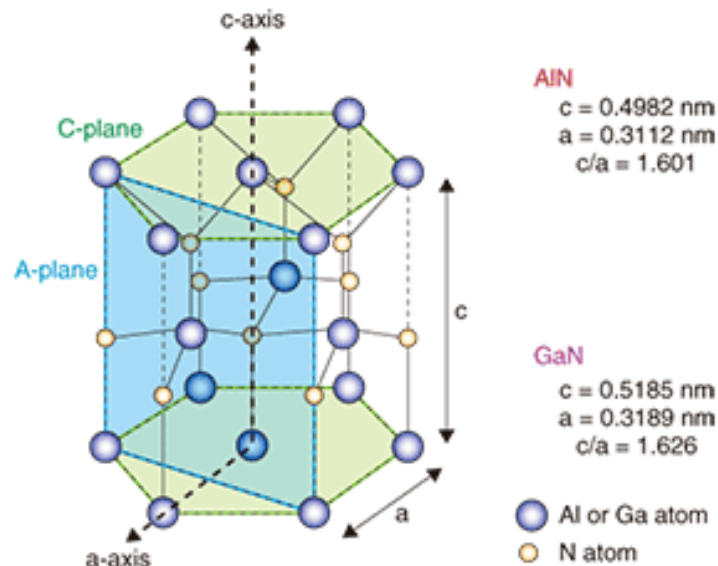


Figure 2.6 – Crystal structure of AlN and GaN [ref. 2.2]

Currently, there are many researches on light emitting diodes (LED) that use ultraviolet rays through Gallium Nitride.

Using alloys of Gallium/Aluminum Nitride in [ref. 2.2], a wavelength of 210 nm has been obtained, in *figure 2.7*. However, some difficulties must be overcome before these LEDs become commercial reality. The applications of UV light sources are showed in *figure 2.8*:

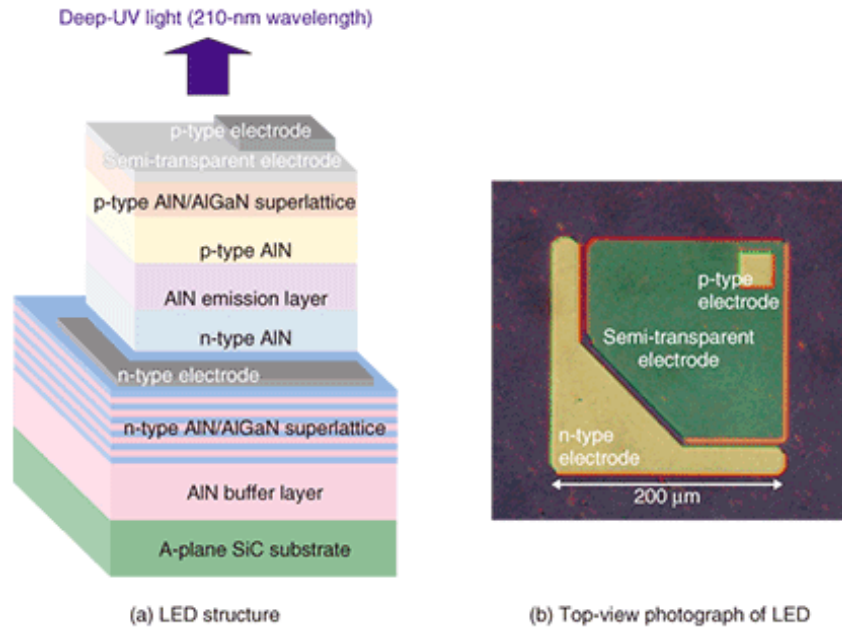


Figure 2.7 – LED structure of 210 nm wavelength [ref. 2.2]

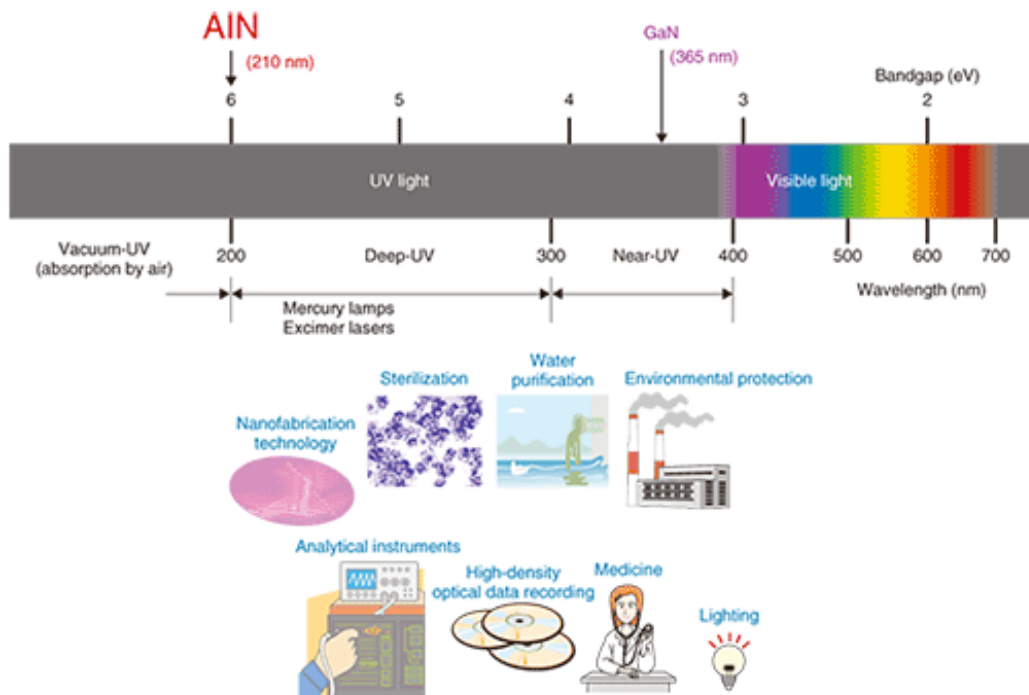


Figure 2.8 – Applications of UV light sources [ref. 2.2]

The crystalline nitride aluminum is used for surface acoustic wave sensors (SAW's) due to piezoelectric properties of AlN. SAW's are obtained from wafers made by aluminum nitride deposited on silicon substrate. Another application that is very close to field of MEMS is the realization of RF filter (FBAR), used in mobile telephony.

Among the application of AlN there is the optoelectronics. It has been used in optical diffusion, in electronic substrates, as a chip carrier where thermal conductivity is indispensable and in the field of war.

As regards mechanical characteristics of AlN, the *table 2.9* was taken as reference:

	PROPERTY	UNITS	
GENERAL	Chemical formula	n/a	AlN
	Density	g/cm ³	3.3
	Water Absorption	%	0
MECHANICAL	Compressive Strength	MPa	-
	Flexural Strength	MPa	200
	Young's Modulus	GPa	320
THERMAL	Max. use temperature	°C	-
	Thermal Conductivity	W/mK	170
	Coefficient of Linear Thermal Expansion	10 ⁻⁶ / °C	5.6
ELECTRICAL	Volume Resistance	Ωcm	>10 ¹⁵
	Dielectric Constant		8.9
	Dielectric Strength	kV/mm	-

Table 2.9 – Properties of AlN (source: goodfellow-ceramics.com)

Aluminum nitride is often modeled by spraying techniques.

As regards the silicon layer, it should have been removed completely after fabrication process. Unfortunately, a thin layer (0.5μm) remains in model, that will be considered in mathematical and FEM model. As mechanical characteristics the value in *table 2.10* were taken:

Density [kg/m³]	2330
Young's modulus [GPa]	150
Poisson's ratio	0.17

Table 2.10 – Mechanical characteristics of silicon

3. FABRICATION OF GaN-BASED MICRO CANTILEVER BEAM

The process to fabricate micro cantilevers analyzed in this thesis will be treated in this chapter. Two cantilevers were produced in Bristol University laboratories, both in a 3-layers configuration that contains GaN and AlN on a Silicon substrate.

To fabricate the cantilevers in 3-layers configuration, could be used the method explained in [ref. 3.1], and a GPS technique in [ref. 3.2]. The technique to realize T-shape micro cantilevers will be explained in the last part of this chapter.

3.1 Fabrication of GaN-on-Silicon substrate [ref. 3.1]

The wafers of silicon were initially cleaned, were dipped in a buffer solution of HF and then immersed in de-ionized water. Later they were dried and placed into MBE vacuum system. The growth of AlGaIn/GaN or GaN thicknesses were measured by a Scanning Transmission Electron Microscopy (STEM). The cross section were examined by VG 601 STEM that acquired images and three-dimensional data that contains an electron energy loss spectrum in each pixel analyzed. Before proceeding to the deposition of nitride layers, a film of 120nm of Ni was deposited by e-beam photolithography. The pattern was transferred in Ni film using an etching process with a solution made by 70% of HNO₃ and 30% of H₂O at room temperature. The growth of Ni film was calculated as 60nm/min.

To fabricate nitride material it was used the dry etching process, using an etch system that consists of STS vacuum load-locked Inductively Coupled Plasma (ICP). To etch nitride film, Cl₂ and Ar gases are used in a ratio Cl₂/Ar of 5/15. The plasma was ignited with a power of 200W, with substrate platen powered at 35W. These powers generate a self-bias of 2140V at pressure of 2m Torr. The dry etching made by ICP is anisotropic, so that forms a vertical "sidewall" in the nitride. Using KOH-based solutions (wet etching), it was difficult to release GaN films on Si. In fact, KOH-based solutions do not have etchant effect on GaN, but they are very aggressive on AlN and Si. In fact, these solutions are used much in etching fabrication of Si or AlN MEMS, in processes of isotropic dry etching. KOH is an anisotropic etchants. After Cl₂/Ar wet etching of nitride film, an etchant made by CF₄ was used in a dry etch of the Si (111) substrate. Later an ICP plasma made by CF₄ – O₂ – Ar in a pressure of 5 m Torr, was used to etch some micrometers in Si (111) layer, without etching of nitride layer. To undercut the nitride film, a solution of KOH/H₂O was used in a temperature of 50°C. It gave an insignificant etch in GaN film. Therefore, after 15 min the GaN was released from Si substrate. In *figure 3.1* there is a freestanding Gan-on-Si cantilever realized in this process.

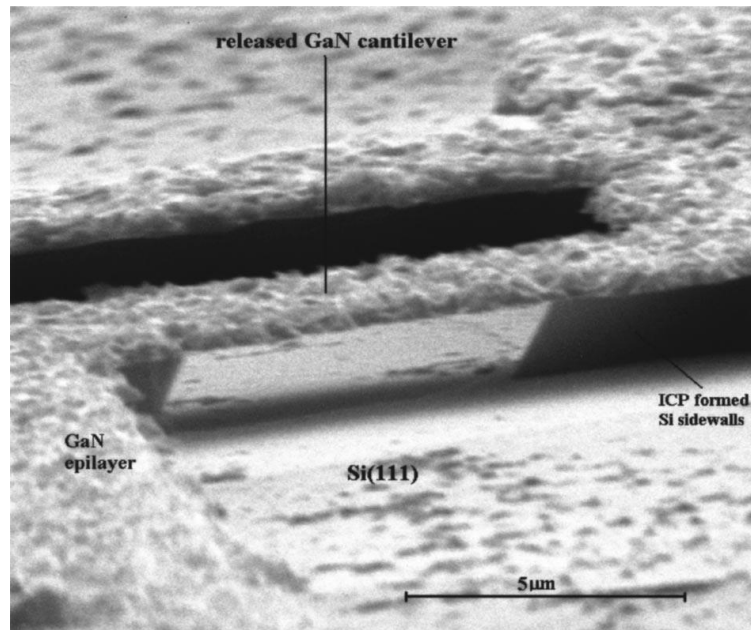


Figure 3.1 – Freestanding GaN cantilever on Si (111) [ref. 3.1]

Figure 3.2 shows a bright field image of a cross section of AlGaIn/GaN/AlN/Si. This image derives from STEM. Red and blue colors represent the AlGaIn and GaN layers, while the green color represents the energy loss frequency, which denotes the AlGaIn/GaN interface.

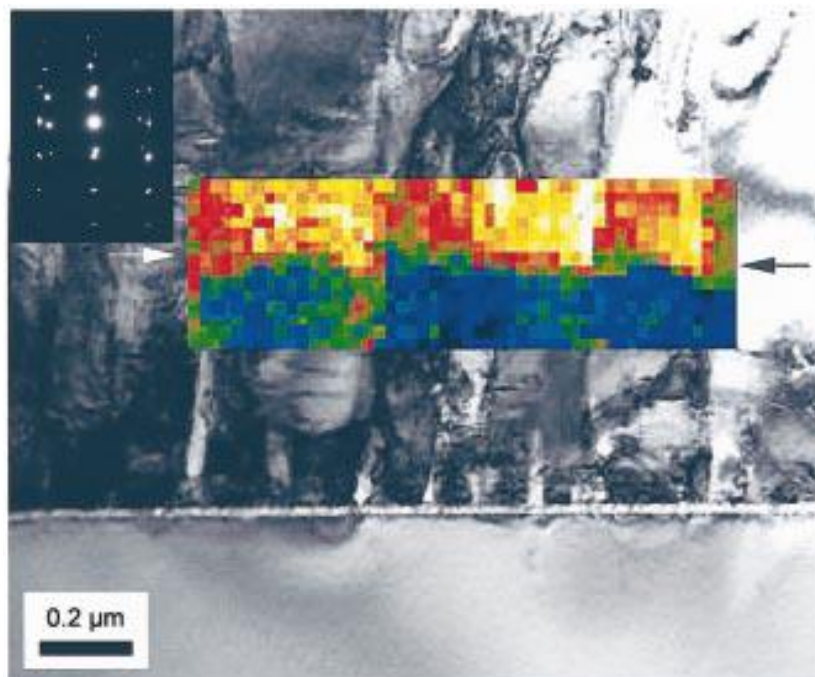


Figure 3.2 – Cross section of AlGaIn/GaN/AlN/Si [ref. 3.1]

It is interesting to notice that a same mosaic structure was observed in GaN-on-Si, using an AlN layer. It was used an high resolution electron microscopy, that was used to show that inversion domains were formed in the AlN layer due to difference in symmetry between the hexagonal buffer layer and the cubic substrate. In figure 3.2 there is a diffraction pattern, that shows the diffraction characteristics of the silicon substrate, AlN inner layer and GaN outer layer. The bright

circular dots represents the silicon planes, while the larger elongated dots represents the planes of GaN layer.

The cross sectional area was determined with Electron Energy Loss Spectrometry (EELS), measured in a STEM system.

The possibility to deposit GaN on Silicon by MBE it is possible using AlN buffer layer, with a combination of dry etching and wet etching processes. The AlGaIn/GaN layers growth in columnar, and presents an hexagonal polytype. The III-nitride cantilevers integrated in Si substrate could be used as piezoresistive transducer elements, which could have applications in MEMS devices.

3.2 Gallium Nitride on patterned silicon (GPS) technique for GaN-based suspended cantilevers [ref. 3.2]

GaN is very resistant from a chemical point of view, therefore, to overcome its inertness it was developed GaN patterned on silicon (GPS) technique in [ref. 3.2]. This technique consists in undercutting GaN film without using the GaN etching process. This technique has the advantage that it could be adapted to the fabrication of AlGaIn/GaN High Electron Mobility Transistors (HEMT) process.

The process to produce this suspended GaN-on-Si cantilever is showed in *figure 3.3*:

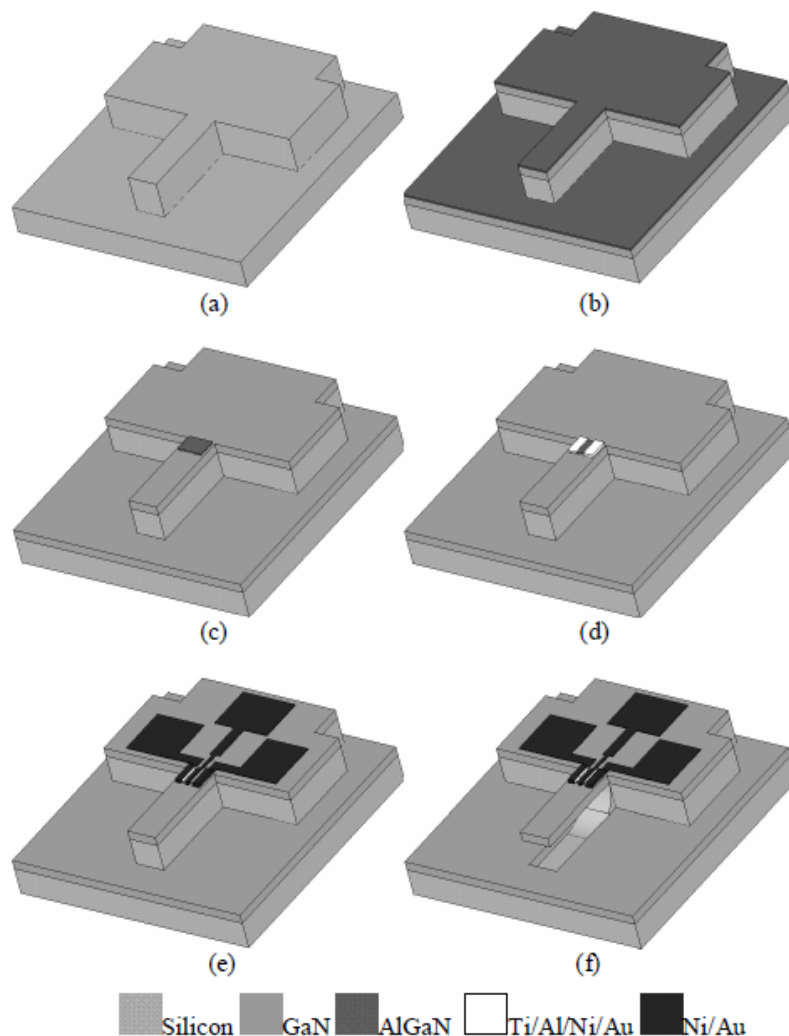


Figure 3.3 – Scheme of GPS technique [ref. 3.2]

In step (a), a pattern of Silicon (111) was realized by using photolithography and inductively plasma ICP RIE. In step (b) GaN layer and AlGaN/GaN layer heterostructures are realized with Metal Organic Chemical Vapor Deposition (MOCVD) process. The growth process is realized in a way that the single crystal III-nitride layers grows only on silicon ridges and on the bottom of the grooves between ridges. During this process (b), a thin nitridation layer grows on the sidewall of the silicon ridges. This thin layer could be removed after 30 second of an immersion in KOH or TMAH solution. After the growth, the GaN patterns are transferred from silicon substrate to GaN films. Therefore, the HEMT process is realized on GaN films.

In step (c), it was realized an etching in Cl_2 -based ICP on the top of cantilever, in order to define the active region. In step (d), it was used an evaporating Ti/Al/Ni/Au multilayer metals in a temperature of 850 °C in N_2 ambient for 30 second, in order to create ohmic contacts. In step (e), other contacts were formed by e-beam evaporated Ni/Au. In the last step (f), the silicon under the cantilever was removed by etching by an anisotropic etchant (25% tetra-methylammonium hydroxide (TMAH)) working at a temperature of 80 °C, and an isotropi etchant $\text{HNO}_3/\text{HF}/\text{H}_2\text{O}$ at room temperature. These two etchants are used separately. The undercut of an anisotropic etchant depends on both the size of GaN structure and the crystalline orientations; therefore, there is the necessity to carefully design the GaN structures in order to ensure the release by anisotropic etchants. GaN results inert by etchants, but if the undercut time is more than 20 minutes, the suspended GaN structures could be attacked by TMAH from the backside. Instead, the isotropic etchant do not attack GaN structures. To realize these structures with an isotropic etchant a photoresist such as AZ4620 could be used to protect the surface from the etching process.

The GPS technique results after all step is represented in figure 3.4. It is showed the suspended cantilever in GaN.

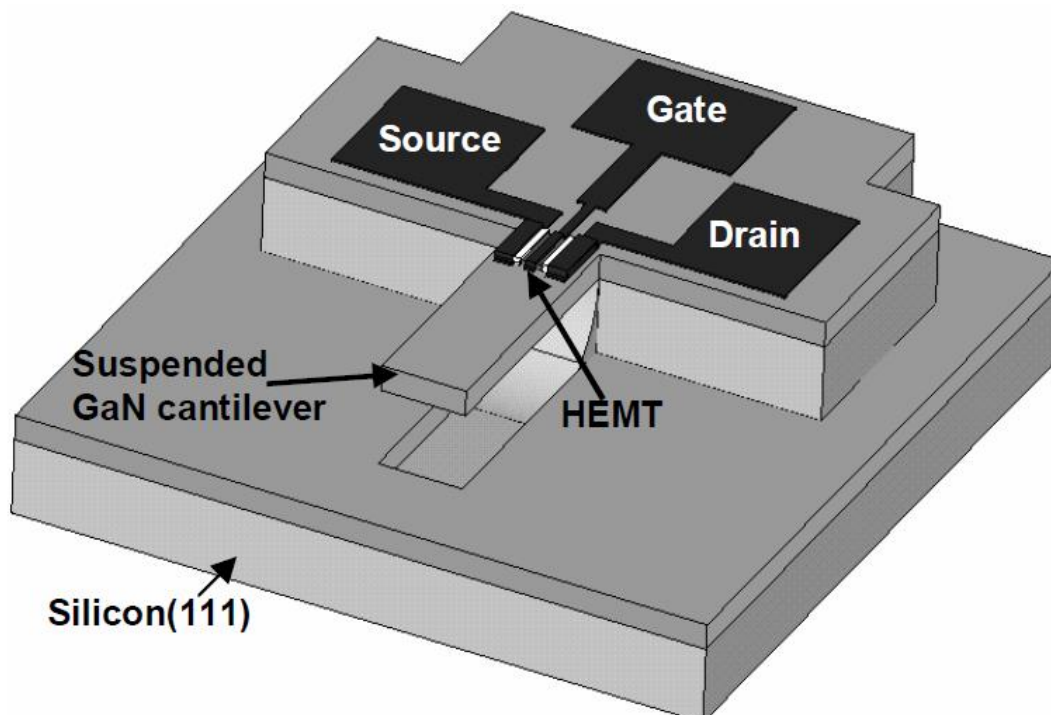


Figure 3.4 – Suspended GaN cantilever result after GPS technique [ref.3.2]

3.3 Fabrication of T-shape GaN-based micro cantilever (3-layers configuration)

Before the fabrication of T-shape cantilevers in Bristol University laboratories, two cantilever were modeled. They are called Cantilever 1 and Cantilever 2 (in *figure 3.5*). These cantilevers are both in T-shape, but they have different dimensions.

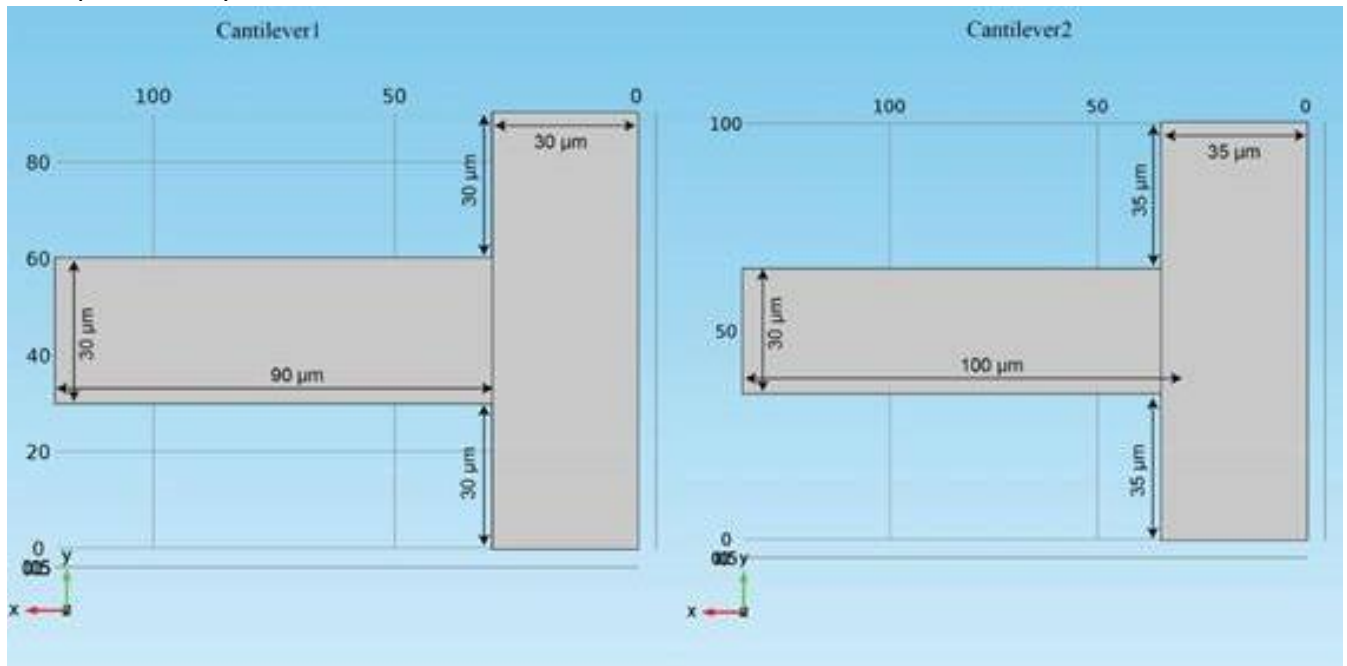


Figure 3.5 – Modeled Cantilever 1 and Cantilever 2

The fabrication of the GaN-on-Silicon T-shape cantilevers was carried out using the BOSCH deep etching process in order to create a window in the backside of the GaN-on-Silicon chip. This process left a residual layer of silicon on the backside of GaN, which will be treated in this thesis. To form the cantilevers in the remaining GaN-Silicon structure it as used a Focused Ion Beam etching (FIB) process. This process uses ion beam from a Liquid Metal Ion Source (LMIS) that contains a reservoir of gallium ions that are emitted from a heated tungsten needle into a large electric field (around 108 volts/cm). Electrostatic lenses were used to aid focus adjustment. When gallium ions (with a high energy) beat the surface, atoms are sputtered while few nanometers of gallium ions are inserted on the surface, making it amorphous. FIB process works in similar way as Scanning Electron Microscope (SEM). The difference is that FIB deals with beam of ions while SEM emits a beam of electrons. It was also used a layer of AlN because it is required to decrease defects density of GaN.

In *figure 3.6* there are the steps to realize the Cantilever 1 and Cantilever 2.

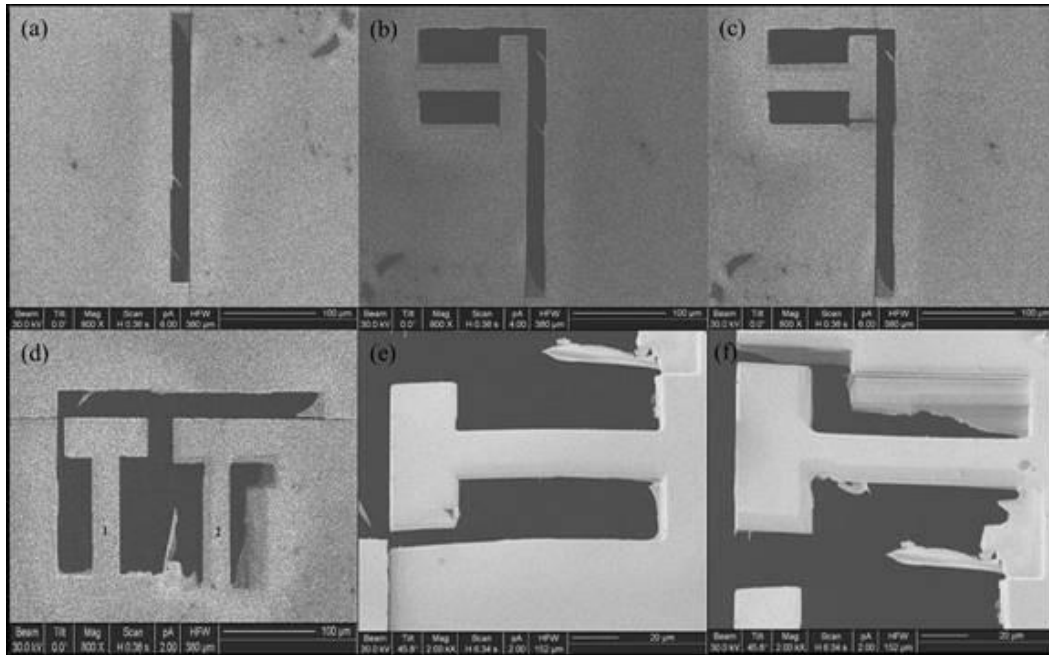


Figure 3.6 – Fabrication process of the Cantilever 1 and Cantilever 2

The instrument FEI Strata FIB201 was used; in fact, the sample was inserted in its chamber. It was fixed with silver paint into a circular stub and it was mounted onto a joystick controlled movable stage, which allows movements in the horizontal plane. In the chamber, vacuum was obtained (below 2.5×10^{-5} mbar) before the Gallium ion source with high beam energy of 30 keV was turned on. Initially, a current of 1pA was used because fractions of the sputtered atoms were ionized since they contained information about the sample. These sputtered atoms and released electrons were used to form simultaneous images to find the sample. In the next step, the sample was put at a certain height at which the stage can be inclined with no movement of the sample. A current of 11.5 nA was used to generate a crack in the membrane as shown in *figure 3.6 (a)*. With same process, the material was removed around the cantilever on the either side. Cleaning-Cross Section (CCS) etches were used to leave a clean edge around the cantilever (in *figure 3.6 (b)*). Using the CCS etch as shown in *figure 3.6 (c)*, the cantilever was released from the bulk material. The Cantilever 2 was realized in the same way, near Cantilever 1 as shown in *figure 3.6 (d)*. It is interesting to notice that the two cantilevers appear bent. Bending occurs due to the high strain in gallium nitride as a material. Using SEM, images of Cantilever 1 and Cantilever 2 were obtained as zoomed images, as *figure 3.7 and 3.8* show.

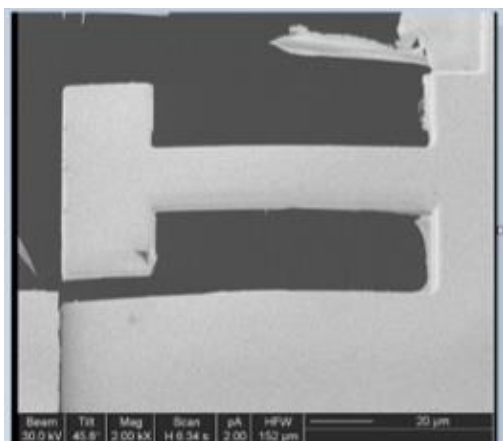


Figure 3.7 – Cantilever 1

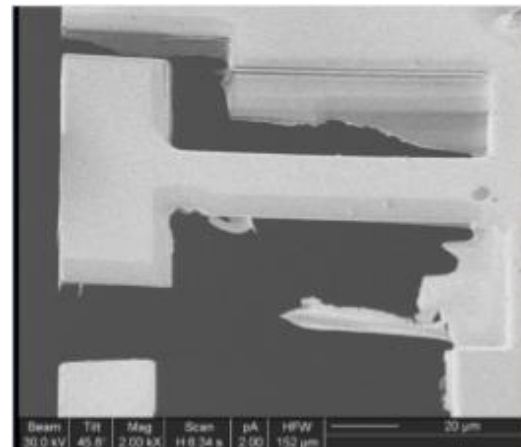


Figure 3.8 – Cantilever 2

Both Cantilever 1 and Cantilever 2, realized in the same sample, present the 3-layers configuration. The thickness of GaN is 1 μm , the thickness of AlN is 0,2 μm and the thickness of Silicon is 0,5 μm .

4. EXPERIMENTAL TESTS WITH LASER DOPPLER VIBROMETER (LDV)

LDV technology is the best method, in term of displacement and velocity resolution, to evaluate the resonance frequency of an object. The output signal of the LDV is a continuous analog voltage that is proportional to velocity of the analyzed object along the direction of the laser beam.

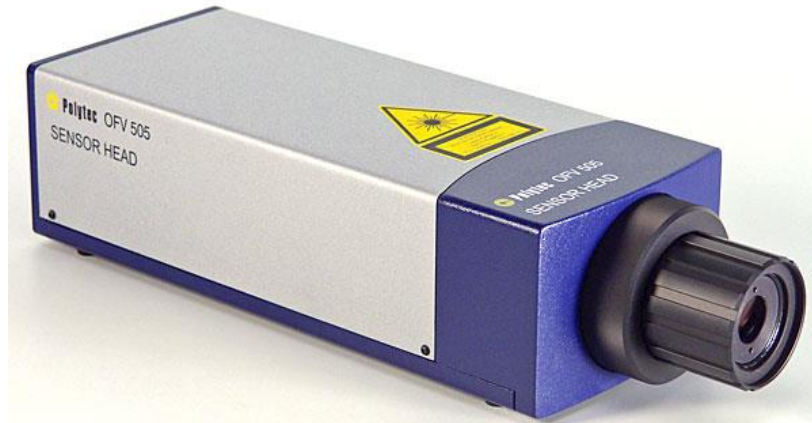


Figure 4.1 – Sensor head of Laser Doppler Vibrometer (source: Polytech.com)

The advantage of LDV technology than other similar instrument like accelerometer is that the LDV offer the possibility to reach very small object like MEMS where result impossible to attach physical elements such as accelerometer. Therefore, LDV work without contact with test objects. Another advantage is that LDV measures the natural frequency of an object without mass loading. These advantages make the LDV indispensable for MEMS devices.

The disadvantage of LDV are the high costs of this technology that make it exclusive for some particular applications, like MEMS or other applications in micro or nanoscale.

4.1 LDV operating principle [ref. 4.1]

The operation of LDV takes place thanks to physical phenomenon of Doppler Effect: *“Doppler Effect is the change in frequency or wavelength of a wave for an observer who is moving relative to the wave source”* [ref. 4.1]. This effect takes the name of the Australian physicist Christian Doppler, who described the phenomenon in 1842. The Doppler Effect comes because when the source of the waves is approaching towards the observer that is stationary, each successive wave is emitted from a point closer to the observer than previous wave. Therefore, the observer feels the wave with a higher tone than the emitting frequency. The contrary happens when the wave emitter is turning away from the observer. In this case, the observer feels a wave with a lower frequency. The classical case of Doppler Effect is the pitch of a siren ambulance approaching to an observer.

Generally, a laser Doppler vibrometer measures the difference in term of frequency, between an internal reference beam and a test beam. The most used type of LDV is the helium-neon laser, although laser diodes, fiber laser and Nd:YAG lasers are also used.

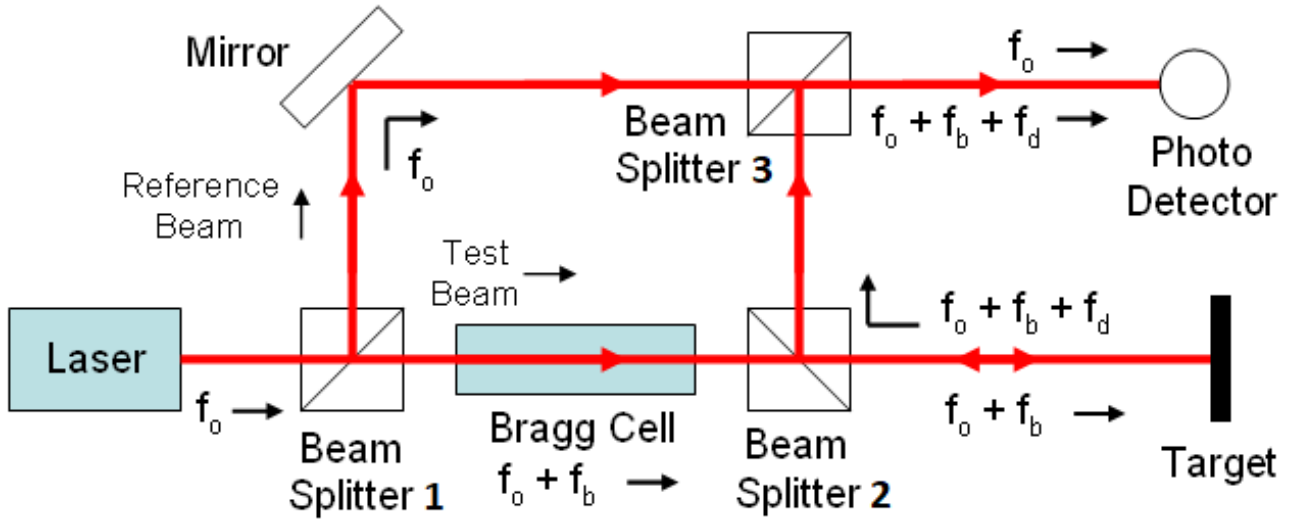


Figure 4.2 – Operating scheme of a Laser Doppler vibrometer (source: Wikipedia)

Figure 4.2 shows the operating scheme of LDV. A laser beam, which has a frequency f_0 , meets the Beam Splitter 1 (BS1). The Beam Splitter is an optical device that splits a beam of light in two parts that preserve the same frequency. Beam Splitters are usually made by polyester, epoxy, or urethane-based adhesives. The BS1 splits the laser beam in a test beam and a reference beam. The test beam then pass through a Bragg Cell, which has the function to add a shift frequency " f_b ". This new frequency " $f_0 + f_b$ " is directed to target. If the target is vibrating, it adds a Doppler shift " f_d " to the beam. This frequency is defined by the formula:

$$f_d = 2 \cdot v(t) \cdot \frac{\cos(\alpha)}{\lambda}$$

Where:

$v(t)$ = velocity of the target as a function of time;

α = angle between laser beam and velocity vector;

λ = wavelength of the laser beam.

The LDV refers to optical laws of interference. When two light beams, with respective intensities " I_1 " and " I_2 " overlap, the total intensity " I_{tot} " is given by:

$$I_{tot} = I_1 + I_2 + \sqrt{(I_1 I_2) \cos \left[\frac{2\pi(r_1 - r_2)}{\lambda} \right]}$$

Where:

$r_1 - r_2$ = path length difference between two beams.

The light reflects on the target, and some beam lights with frequency " $f_0 + f_b + f_d$ ", are directed by the BS2 and BS3 to the photodetector.

The reference beam, which has a frequency " f_0 ", passes through the BS3 and reaches the photodetector.

The photodetector receive both the reference beam " f_0 " and reflected beam " $f_0 + f_b + f_d$ ". Confronting these two beams, and knowing " f_0 " and " f_b ", it is possible to determine the frequency " f_d ". In fact, the initial frequency of the laser beam is very high ($>10^{14}$ Hz), which is higher than the response of the photodetector. The measures is possible because the instrument responds to the difference of beat frequency between two beams, which is " $f_b + f_d$ " (typically in tens of MHz range).

The output signal of the photodetector is a standard frequency modulated signal. It has the Bragg frequency " f_b " as carrier frequency, and Doppler shift " f_d " as modulation frequency. The LDV transforms the Doppler frequency into a voltage proportional to velocity. Furthermore, it is possible to measure also displacements of the target with the LDV. Therefore, the Doppler frequency " f_d " is not transformed into a voltage proportional to velocity, but the LDV counts the light/dark fringes on the detector. Using mathematical interpolation, the LDV could obtain a resolution of 2 nm, while using digital demodulation techniques, the resolution could be around pm range. Instead, it is also possible to demodulate the signal obtaining the velocity of the target. In fact, displacement demodulation is better for low frequency measurements (in Hz range), while velocity demodulation is better for higher frequencies.

4.2 Experimental test on micro cantilever with LDV

The resonance frequencies of both fabricated Cantilever 1 and Cantilever 2 were measured in the laboratories of University of Bristol using a Laser Doppler vibrometer. *Figure 4.3* shows the scheme of the experiment.

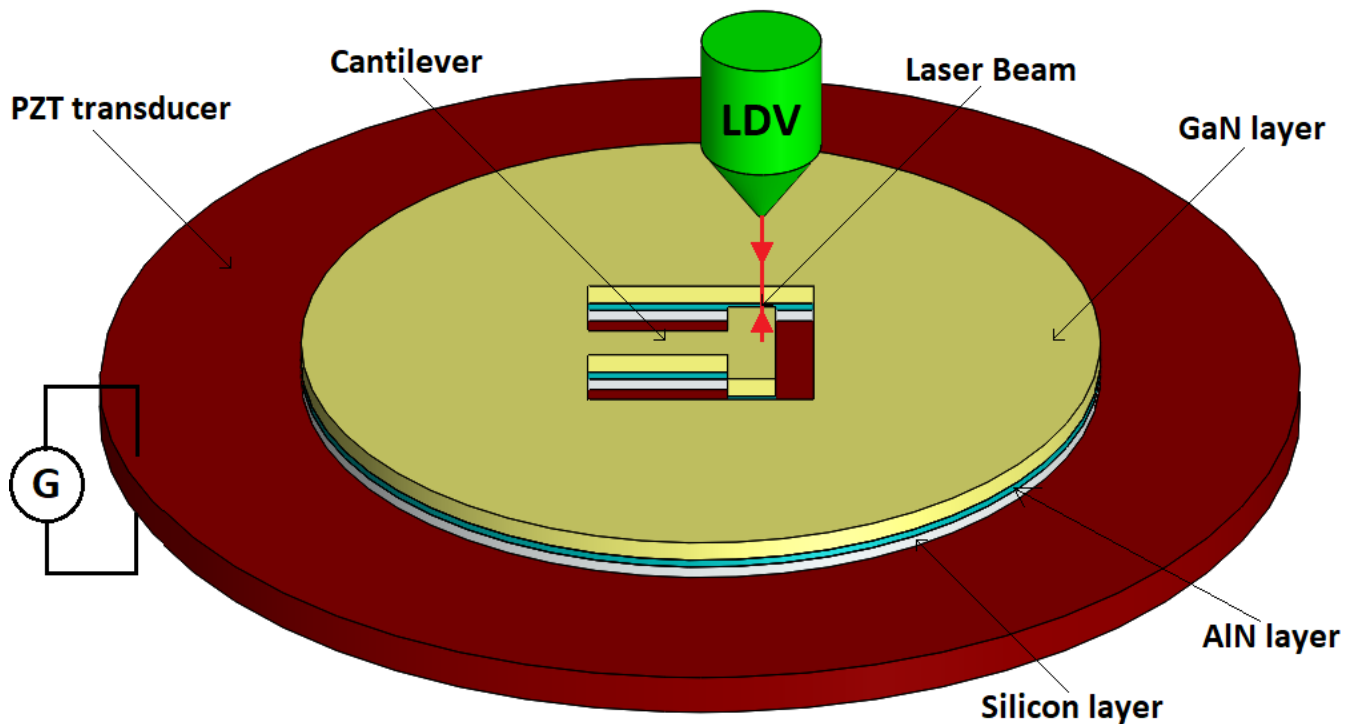


Figure 4.3 – Scheme of experiment setup

A PZT transducer was used to excite the fabricated micro cantilevers by placing the fabricated chip that contains Cantilever 1 and Cantilever 2 over it. The PZT transducer is excited by a sinusoidal signal and makes the cantilever vibrates.

Unfortunately, the experiment was conducted just on micro cantilever in 3-layers configurations. There are no available results in term of resonance frequencies of a 2-layers configuration.

Therefore, in this case, “Cantilever 1” and “Cantilever 2” refer to a 3-layers configuration.

To record the frequencies response, a Graphtec LT-7901 Laser Doppler Vibrometer was used.

The *figure 4.4* shows a photograph of the chip with fabricated cantilevers in zoomed pictures, while in *figure 4.5* and in *figure 4.6* Cantilever 1 and Cantilever 2 are depicted.



Figure 4.4 – Chip with fabricated micro cantilevers

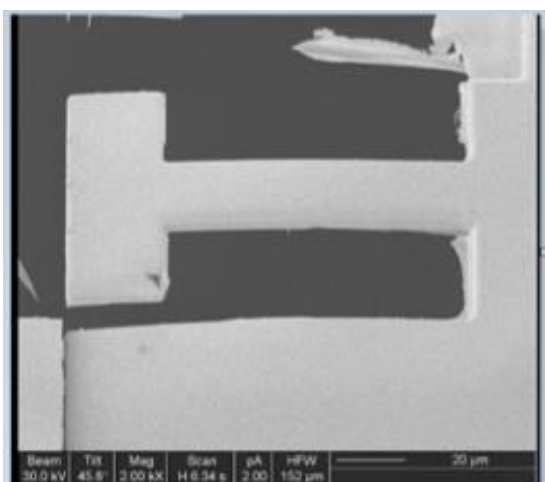


Figure 4.5 – Zoomed Cantilever 1

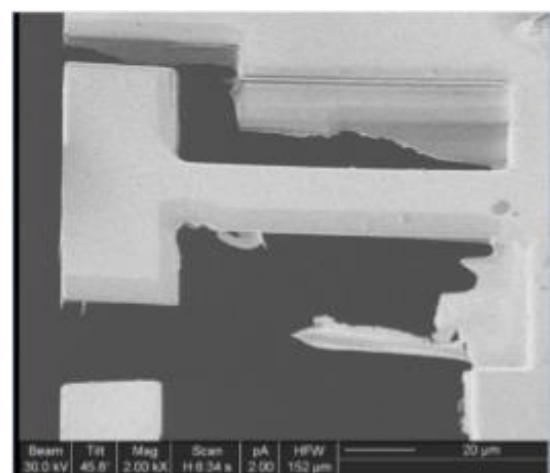


Figure 4.6 – Zoomed Cantilever 2

In order to identify the resonance frequency of the cantilevers, it is necessary to observe the peak of LDV response as a function of the excitation frequency. In fact, in *figure 4.7* and in *figure 4.8* the two graphs of Cantilever 1 and Cantilever 2 are reported:

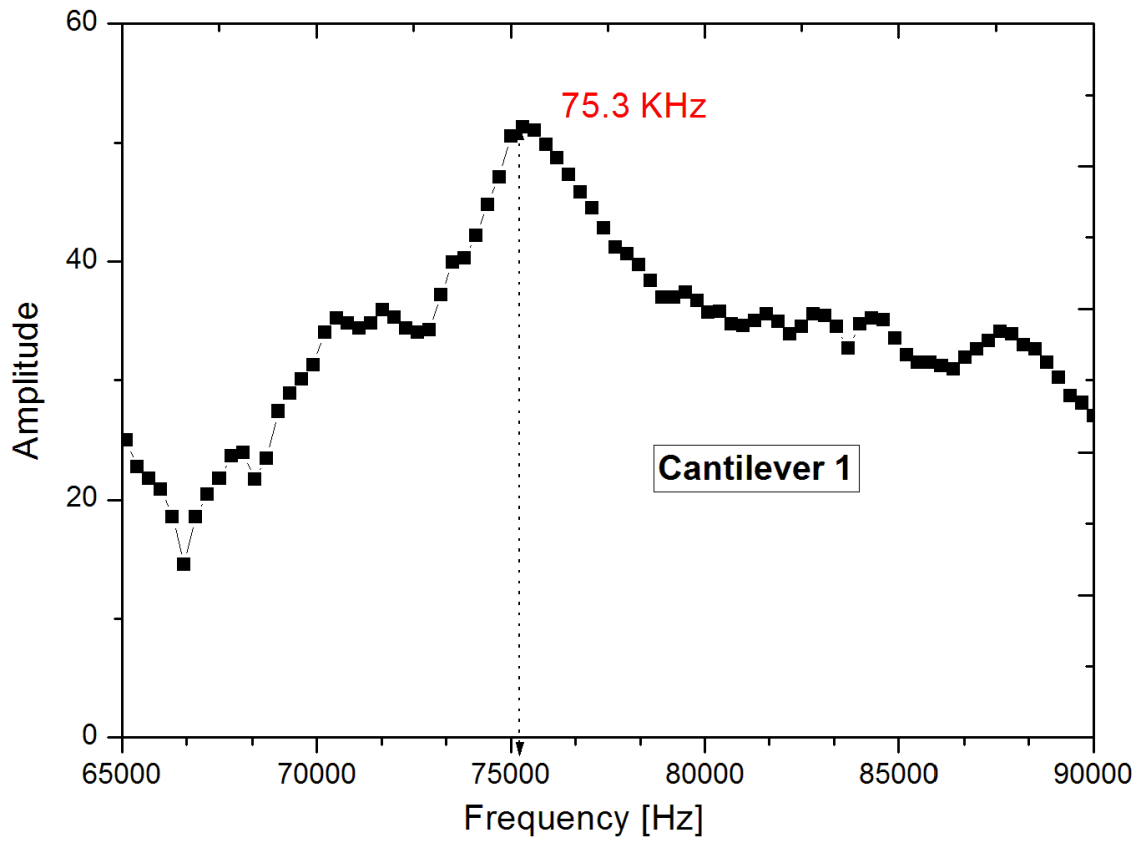


Figure 4.7 – LDV response in function of excitation frequency of Cantilever 1 in 3-layers configuration

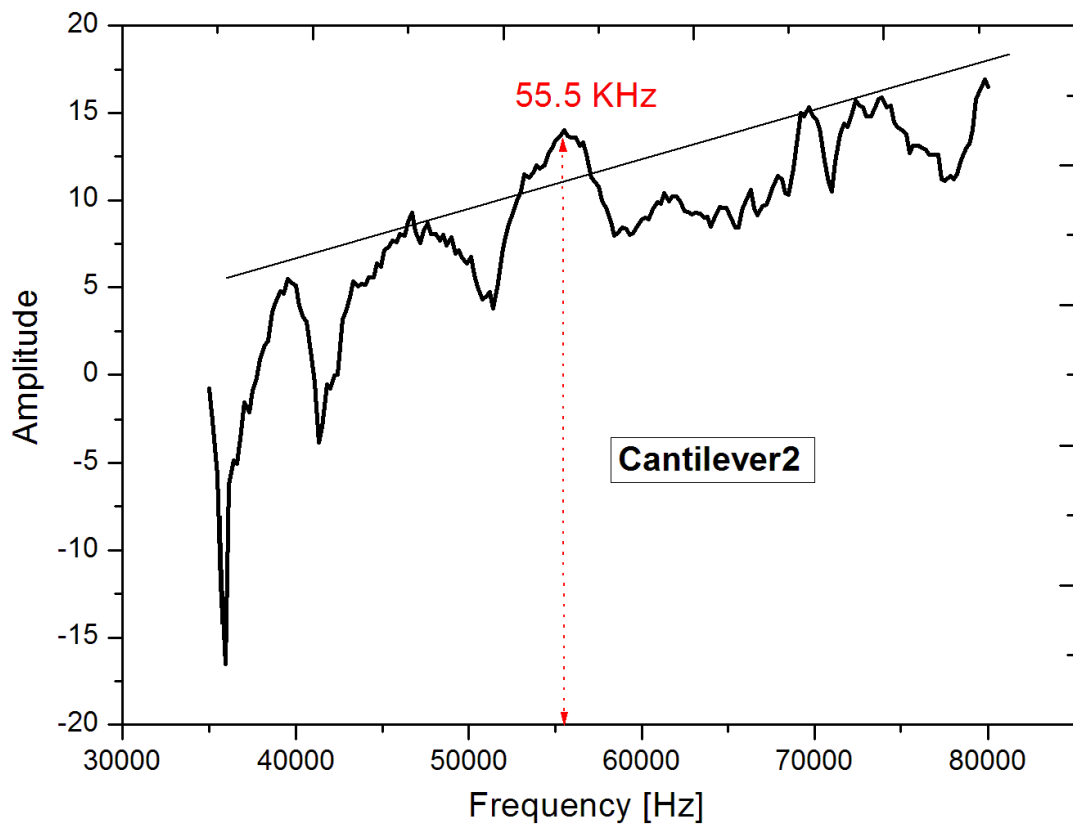


Figure 4.8 – LDV response in function of excitation frequency of Cantilever 2 in 3-layers configuration

The resonance frequency of Cantilever 1 is 75.3 kHz, while the resonance frequency of Cantilever 2 is 55.5 kHz.

5. MATHEMATICAL MODELING OF THE FIRST NATURAL FREQUENCY

To define a mathematical model for the first natural frequency it is possible to define the way in which the micro cantilever beam vibrates. Therefore, two types of mechanical vibrations were studied, which depend on the orientation of the micro cantilever beam in the plan. These two types of orientation, that will be called “Bending 1” and “Bending 2”, are showed in *figure 5.1* and in *figure 5.2*:

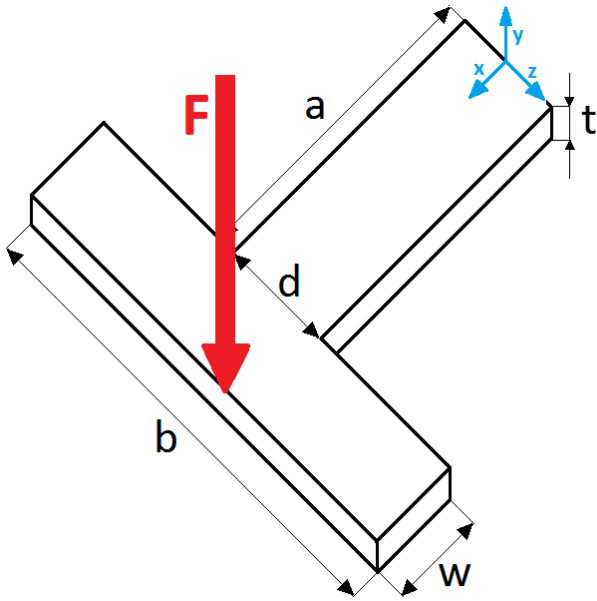


Figure 5.1 – BENDING 1 vibration

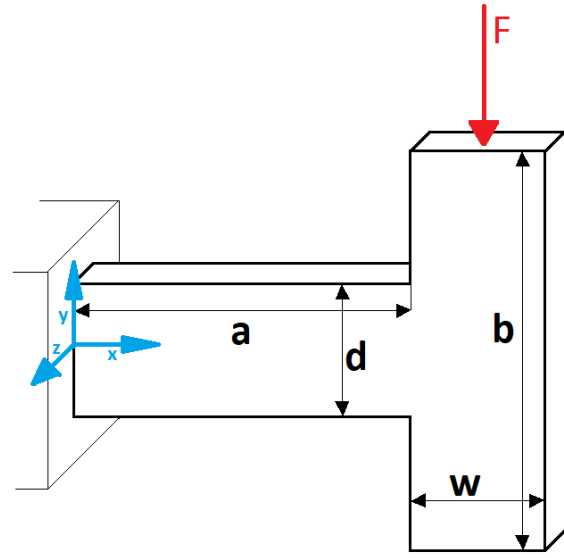


Figure 5.2 – BENDING 2 vibration

The determination of mathematical model starts from the two case of micro cantilever beam. In the *figure 5.1* and in *figure 5.2* there are two representation of fictitious forces F . In both cases, the force F bends the cantilever, in direction of x -axis in Bending 1, and in direction of y -axis in Bending 2.

Geometrical parameters were defined (“ a ”, “ w ”, “ b ”, “ d ”, and the thickness “ t ”), and showed in *figure 5.1* and *figure 5.2*. The Cantilever 1 and Cantilever 2 present the follow dimension:

Cantilever 1 $\rightarrow a = 90\mu m; \quad w = 30\mu m; \quad b = 90\mu m; \quad d = 30\mu m;$

Cantilever 2 $\rightarrow a = 100\mu m; \quad w = 35\mu m; \quad b = 100\mu m; \quad d = 30\mu m;$

The thickness “ t ” of Cantilever 1 and Cantilever 2 will be treated as 2-layers and as 3-layers.

To simplify the mathematical result, the micro cantilever beam were parametrized in three simple dimensionless parameter (α , β and γ). The *figure 5.3* shows in details the dimensionless parameters.

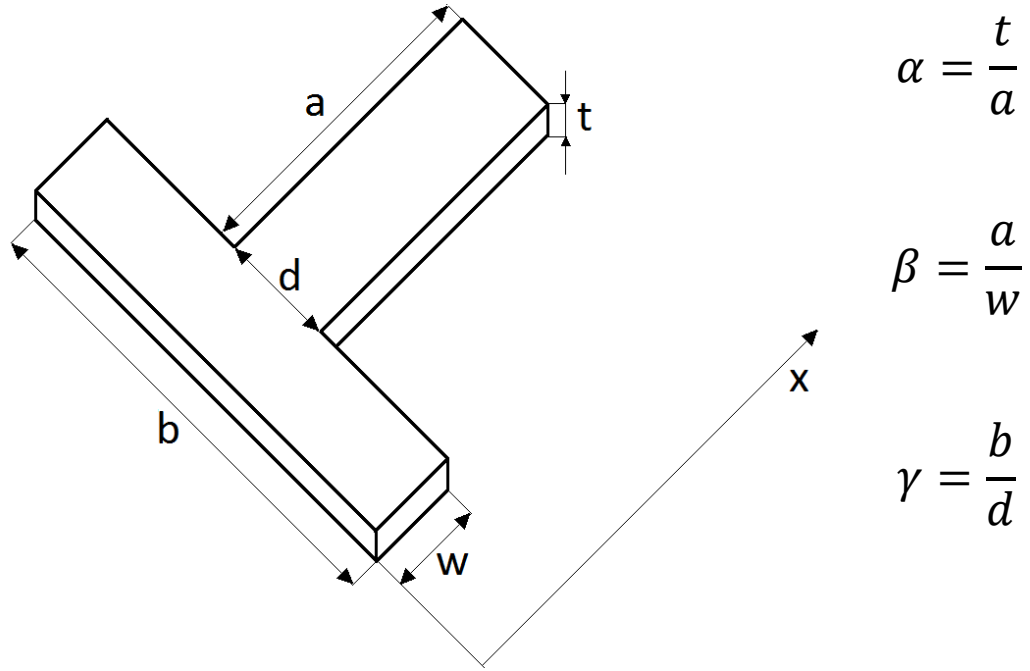


Figure 5.3 – the representation of the micro cantilever beam in dimension

The micro cantilever beam can be model as a generic mass – spring system as in figure 5.4:

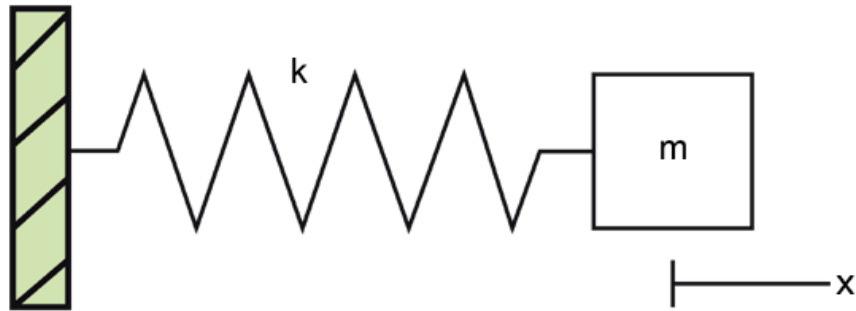


Figure 5.4 – Mass – Spring system

The mass “m” amounts in our micro beam to its mass, while the stiffness “k” represents the structural stiffness of the body of the beam. Figure 5.4 shows a free vibration system without damping. The damping is negligible and there are not external forces applied to the mass. The force applied from the spring to the mass (F_s) is proportional to the amount of the spring is stretching or compressing along the “x” axis. The stiffness “k” is the proportionality constant:

$$F_s = -kx \quad (5.1)$$

The negative sign indicates that the force is always opposing to motion of the mass. During the vibration of this system, the force generated by the mass is proportional to acceleration of the mass, as the Newton’s second law says:

$$\sum F = ma = m\ddot{x} = m \frac{d^2x}{dt^2} \quad (5.2)$$

The sum of all forces on the mass generates the ordinary differential equation:

$$m\ddot{x} + kx = 0 \quad (5.3)$$

Assuming that the initiation of vibration starts by stretching or compressing the spring by the distance of “A” and later releasing, the solution to the equation (5.3) that describes the motion of mass is:

$$x(t) = A\cos(\omega_n t) \quad (5.4)$$

Now it's possible to determine the equation of $\ddot{x}(t)$ deriving two times $x(t)$:

$$\dot{x}(t) = -A\omega_n \sin(\omega_n t)$$

$$\ddot{x}(t) = -A\omega_n^2 \cos(\omega_n t) \quad (5.5)$$

Solving the ordinary differential equation after replacing the equations (5.5) and (5.4) in (5.3), it's possible to obtain the formula that give the calculation of the first natural frequency:

$$\omega_n = \sqrt{\frac{k}{m}} \quad (5.6)$$

The results of equation (5.6) has the unit of measure of [rad/s]. To obtain the unit of measure of [Hz] is just necessary divide the result in [rad/s] by 2π . Knowing the mass and the stiffness of each system it is possible to calculate the frequency at which each system vibrates once set in motion by an initial disturbance.

Regarding the micro cantilever beam in T-shape, it is necessary to define its mass and stiffness to calculate the value of the first natural frequency.

5.1 Determination of the mass “m”

To determine the mass of the cantilever beam, it is sufficient to use the simple formula:

$$m = \rho V \quad (5.7)$$

Where:

ρ = density of material [kg/m³];

V = volume of the object [m³];

The calculation of Bending 1 and Bending 2 will proceed in parallel, while the mass is the same in both cases. The mass of the cantilever was calculated keeping in mind that the micro cantilever beam is composite by a multi-layer. Contemporary to the study of mathematical model, a model on Solidworks® was produced, where it is possible to perform a finite element analysis.

Therefore, there is a double-layer case (2-layers) and a triple-layer case (3-layers):

- **5.1.1 Mass in 2-layers configuration**

This type of cantilever beam is composite by a double layer of different material (GaN + Silicon). These two layers are considered overlapped and perfectly bounded.

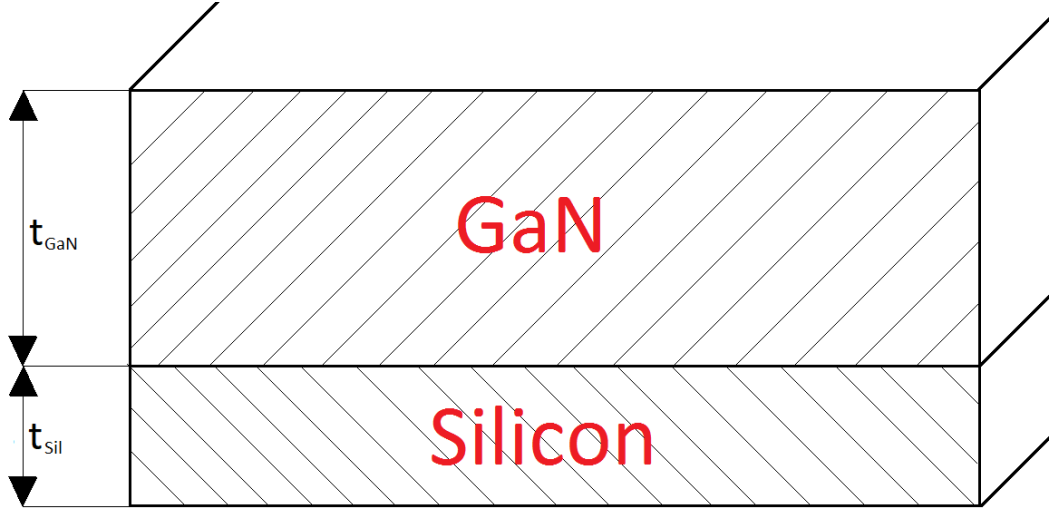


Figure 5.5 – Representation of cross section of 2-layers micro-cantilever

The thicknesses of GaN and Silicon layers are considered respectively 1,5 μm and 0,5 μm . In figure 5.5, there is a representation of cross sectional area of 2-layers model. The dimension of thickness of t_{GaN} or t_{Sil} is comparable with the width. This is just an enlargement of the thickness to show in clear way the two layers. The ratio between thickness “t” and width “d” in real cantilever is for example $2\mu\text{m}/30\mu\text{m}$ in “Cantilever 1”. The calculation for a 2-layers model starts from the simple formula of mass, but using the two different value of density:

$$m_{2-l} = \rho_{\text{GaN}}(adt_{\text{GaN}} + wbt_{\text{Sil}}) + \rho_{\text{Sil}}(adt_{\text{Sil}} + wbt_{\text{Sil}}) \quad (5.8)$$

The process of parametrization of the mass begins reducing the equations until minimum number of dimensional parameters was obtained. For example, parametrizing the thickness t_{GaN} and t_{Sil} :

$$t_{\text{GaN}}/t = p_{\text{GaN}} \quad (5.9)$$

$$t_{\text{Sil}}/t = p_{\text{Sil}} = 1 - p_{\text{GaN}} \quad (5.10)$$

$$t = t_{\text{GaN}} + t_{\text{Sil}} \quad (5.11)$$

Substituting equations (5.9), (5.10) and (5.11) in equation of mass (5.8):

$$\begin{aligned}
m_{2-l} &= \rho_{GaN}(adt_{GaN} + wbt_{GaN}) + \rho_{Sil}(adt_{Sil} + wbt_{Sil}) \\
&= \rho_{GaN}p_{GaN}t(ad + wb) + \rho_{Sil}p_{Sil}t(ad + wb) \\
&= (\rho_{GaN}p_{GaN} + \rho_{Sil}p_{GaN})t(ad + wb) \\
&= \rho^*t(ad + wb) \quad (5.12)
\end{aligned}$$

Where:

$$\rho^* = \rho_{GaN}p_{GaN} + \rho_{Sil}p_{Sil}$$

With some arithmetic calculation, substituting the dimensionless terms (α , β and γ), the final equation of mass was found:

$$m_{2-l} = \rho^* \frac{\alpha}{\beta} a^2 b \left(\frac{\beta}{\gamma} + 1 \right) \quad (5.13)$$

- 5.1.2 Mass in 3-layers configuration

This type of cantilever beam is composite by a triple layer of (GaN + AlN + Silicon). These three materials are overlapped and perfectly bounded between them as in case of 2-layers. In *figure 5.6*, there is a representation of a cross sectional area of 3-layers model. As in previous case of 2-layers model, the dimensions of t_{GaN} , t_{AlN} and t_{Sil} are enlargement to show better the division of three thicknesses. The ratio between thickness “t” and width “d” is for example $1.7\mu\text{m}/30\mu\text{m}$ on Cantilever 1.

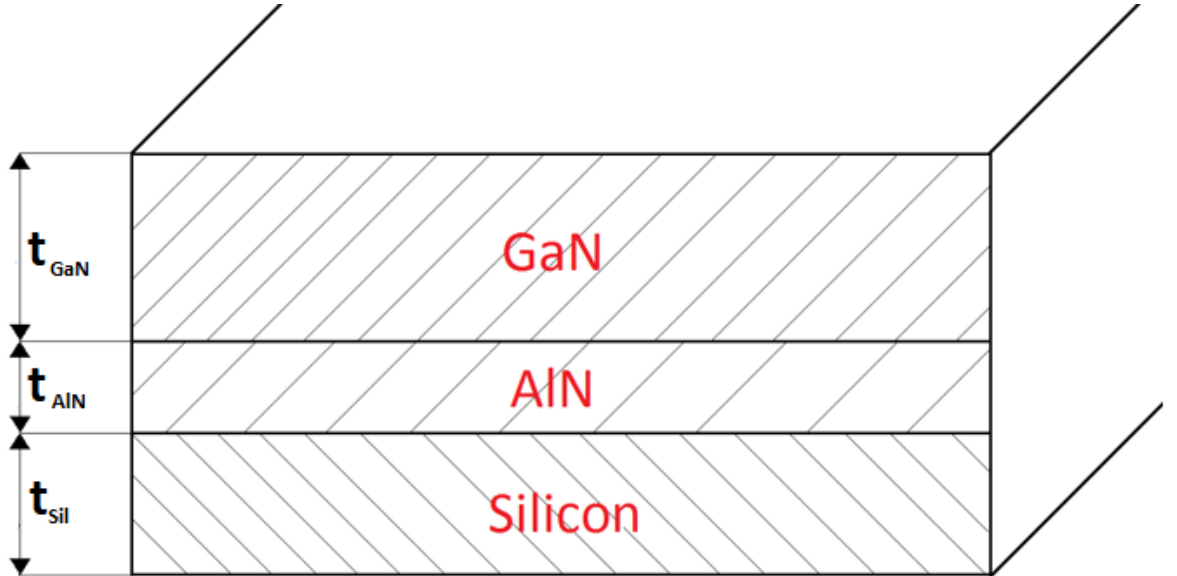


Figure 5.6 – Representation of cross section of 3-layers micro-cantilever

The thicknesses of GaN, AlN and Silicon layers are respectively $1\mu\text{m}$, $0,2\mu\text{m}$ and $0,5\mu\text{m}$. In this case, there is one more layer; therefore, there is another parameter of thickness:

$$t_{GaN}/t = p_{GaN} \quad (5.14)$$

$$t_{AlN}/t = p_{AlN} \quad (5.15)$$

$$t_{Sil}/t = p_{Sil} = 1 - p_{GaN} - p_{AlN} \quad (5.16)$$

$$t = t_{GaN} + t_{AlN} + t_{Sil} \quad (5.17)$$

The equation of mass become:

$$m_{3-l} = \rho_{GaN}(adt_{GaN} + wbt_{GaN}) + \rho_{AlN}(adt_{AlN} + wbt_{AlN}) + \rho_{Sil}(adt_{Sil} + wbt_{Sil}) \quad (5.18)$$

Where:

$$\rho^* = \rho_{GaN}p_{GaN} + \rho_{AlN}p_{AlN} + \rho_{Sil}p_{Sil}$$

Progressing in the same way as in case of 2-layers, the equation of mass was determined:

$$m_{3-l} = \rho^* \frac{\alpha}{\beta} a^2 b \left(\frac{\beta}{\gamma} + 1 \right) \quad (5.19)$$

The equation of 2-layers and 3-layers are the equal about geometrical parameters. Just the term ρ^* changes. Summarizing the calculation of mass in following *Table 1*:

	2-layers	3-layers
MASS [Kg]	$m_{2-l} = m_{3-l} = m = \rho^* \frac{\alpha}{\beta} a^2 b \left(\frac{\beta}{\gamma} + 1 \right)$	
ρ^*	$\rho_{GaN}p_{GaN} + \rho_{Sil}p_{Sil}$	$\rho_{GaN}p_{GaN} + \rho_{AlN}p_{AlN} + \rho_{Sil}p_{Sil}$

Table 5.7 – Calculation of mass in 2-layers and 3-layers model

Once equations of mass were determined, the stiffness will be the next step to calculate.

5.2 Determination of the stiffness “k”

To determine the Stiffness “k” Castigliano’s second theorem was used. It says: “If the strain energy U of a linearly elastic structure can be expressed as a function of generalised force F then the partial derivative of the strain energy with respect to generalised force gives the generalised displacement δ in the direction of F ”:

$$\delta(x) = \frac{\partial U}{\partial F} \quad (5.20)$$

Where:

U = Strain Energy;

F = Load.

In this system, a generic test Force “ F ” was considered.

To study the model is necessary to distinguish the two cases of Bending 1 and Bending 2, because the different orientation of the force that make to bend the micro beam in different way. For simplicity, just the studies of 2-layers model (in figure 5.8) were developed, because studies of 3-layers model (in figure 5.9) will result the same. This is possible because thickness “ t ” is responsible just of moment of inertia. Then in calculating moment of inertia, the differences between 2-layers and 3-layers model will be explained.

- 5.2.1 Stiffness “k” in Bending 1

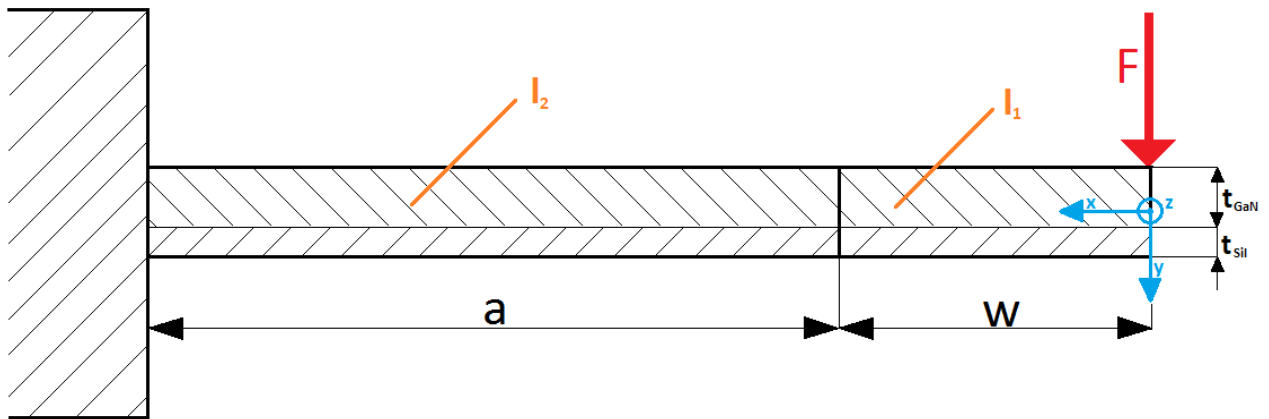


Figure 5.8 – Representation of micro cantilever on x-y plane (Bending 1)

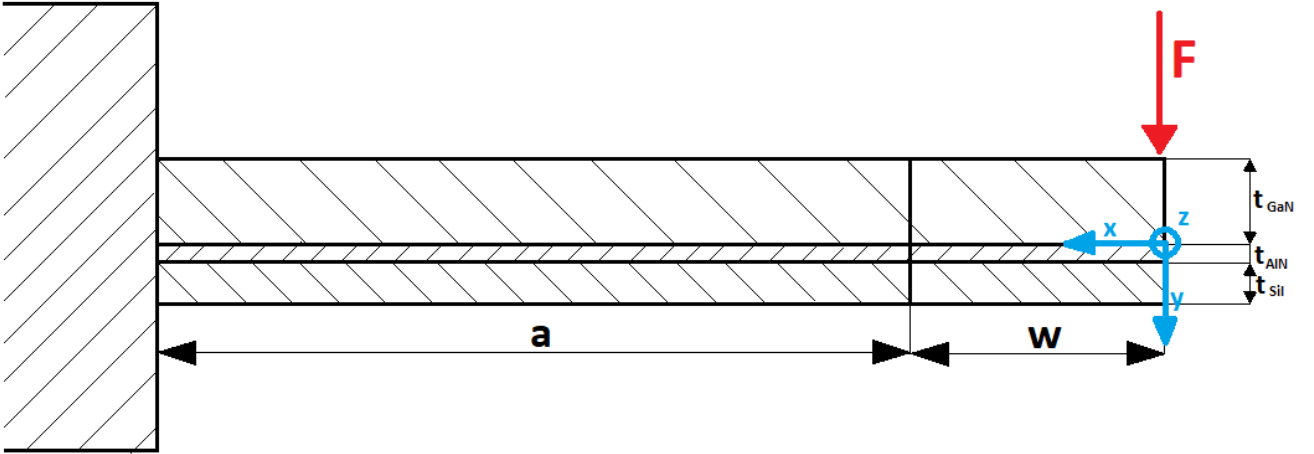


Figure 5.9 – Representation of micro cantilever in 3 layer model (Bending 1)

In figure 5.8, there is a representation of micro cantilever with a single generic concentrated load F in the end. It bends the cantilever in direction of y -axis. To start Castigliano's Theorem is necessary to define the strain energy "U":

$$U = \int_0^w \frac{M^2(x)}{2E^*I_1} dx + \int_w^{w+a} \frac{M^2(x)}{2E^*I_2} dx \quad (5.21)$$

Where:

$M = F \cdot x = \text{Moment}$;

$E^* = \text{Equivalent Young's Modulus}$;

$I_1 = \text{Moment of Inertia of section 1}$

$I_2 = \text{Moment of Inertia of section 2}$

Replacing the Moment in equation (5.21):

$$U = \int_0^w \frac{F^2 x^2}{2E^*I_1} dx + \int_w^{w+a} \frac{F^2 x^2}{2E^*I_2} dx \quad (5.22)$$

Solving the integrals:

$$U = \frac{F^2}{6E^*I_1} w^3 + \frac{F^2}{6E^*I_2} [a^3 + 3a^2w + 3w^2a] \quad (5.23)$$

Castigliano's Method allows to calculate the maximum deflexion $\delta(x = 0)$ at the end of cantilever, where the load F is applied:

$$\begin{aligned}\delta(x=0) &= \frac{\partial U}{\partial F} = \frac{F}{3E^*I_1}w^3 + \frac{F}{3E^*I_2}[a^3 + 3a^2w + 3w^2a] \\ &= \frac{F(I_2w^3 + I_1a^3 + 3I_1a^2w + 3I_1aw^2)}{3E^*I_1I_2}\end{aligned}\quad (5.24)$$

The stiffness “k” is:

$$k = \frac{F}{\delta} \quad (5.25)$$

Replacing the equation (5.24) in (5.25):

$$k = \frac{F}{\delta} = \frac{3E^*I_1I_2}{(I_2w^3 + I_1a^3 + 3I_1a^2w + 3I_1aw^2)} \quad (5.26)$$

The both cross section of the cantilever are rectangular. In the first cross section there is the base “d” and the total height “t”, that is the sum of the single thicknesses of all layers. In the second one, while the thickness remains the same, the base measures “b”. The moments of inertia are different in 2-layers model from 3-layers model. The both moments of inertia I_1 and I_2 , in 2-layers and 3-layers case, could be represented as:

$$I_{1-2layer} = \frac{b(t_{GaN} + t_{SiL})^3}{12} = \frac{bt^3}{12} \quad (5.27)$$

$$I_{1-3layer} = \frac{b(t_{GaN} + t_{AlN} + t_{SiL})^3}{12} = \frac{bt^3}{12} \quad (5.28)$$

$$I_{2-2layer} = \frac{d(t_{GaN} + t_{SiL})^3}{12} = \frac{dt^3}{12} \quad (5.29)$$

$$I_{2-3layer} = \frac{d(t_{GaN} + t_{AlN} + t_{SiL})^3}{12} = \frac{dt^3}{12} \quad (5.30)$$

Replacing “ I_1 ” (5.27 – 2-layers) or (5.28 – 3-layers) and “ I_2 ” (5.29 – 2-layers) or (5.30 – 3-layers) in equation (5.26), after some arithmetic passages:

$$k = \frac{E^*/4 bdt^3}{dw^3 + ba^3 + 3ba^2w + 3baw^2} \quad (5.31)$$

This is the final equation to calculate the stiffness “k”. It depends only from geometrical and material parameters. Introducing dimensionless parameter (α , β and γ), the final equation of stiffness “k” is:

$$k = \frac{E^*/4 b \alpha^3 \beta^3}{1 + \gamma \beta^3 + 3\gamma \beta^2 + 3\gamma \beta} \quad (5.32)$$

The stiffness, represented in this way, depends from all dimensionless parameter, except “b” and “E*”.

- 5.2.2 Stiffness “k” in Bending 2

To obtain the representation in the plan x-z of the micro cantilever, it is necessary to turn the cantilever in *figure 5.8* around x-axis. In Bending 2, the force “F” is parallel to z-axis, while in Bending 1 it was parallel to y-axis. A different distribution of the load, ensure a different bending of the cantilever. For sure, the first natural frequency of Bending 2 will be higher than first natural frequency in Bending 1, because of the higher moment of inertia. In *figure 5.10*, there is the representation of the micro cantilever in plane x-z:

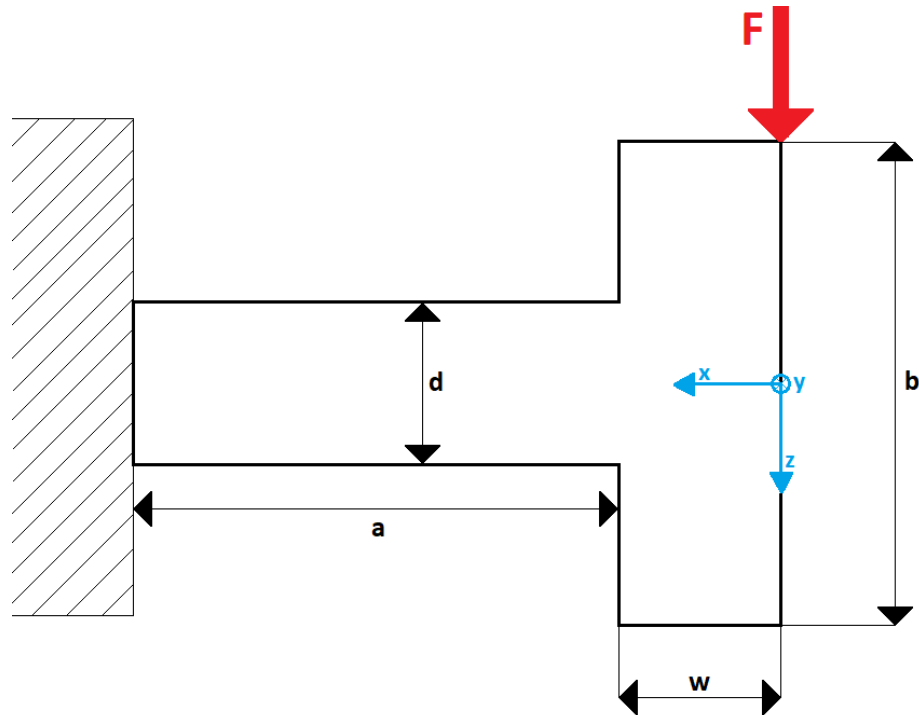


Figure 5.10 – Representation of micro cantilever on x-z plane (Bending 2)

The load is responsible of the bending of the micro cantilever in plan x-z. In fact, proceeding in calculation of the stiffness “k” in the same way of previous case (Bending 1), the same equation (5.26) was determined:

$$k = \frac{F}{\delta} = \frac{3E^* I_1 I_2}{I_2 w^3 + I_1 a^3 + 3I_1 a^2 w + 3I_1 a w^2} \quad (5.26)$$

In this case, the moments of inertia are:

$$I_{1-2layer} = \frac{(t_{GaN} + t_{SiL})b^3}{12} = \frac{tb^3}{12} \quad (5.33)$$

$$I_{1-3layer} = \frac{(t_{GaN} + t_{AlN} + t_{SiL})b^3}{12} = \frac{tb^3}{12} \quad (5.34)$$

$$I_{2-2layer} = \frac{(t_{GaN} + t_{SiL})d^3}{12} = \frac{td^3}{12} \quad (5.35)$$

$$I_{2-3layer} = \frac{(t_{GaN} + t_{AlN} + t_{SiL})d^3}{12} = \frac{td^3}{12} \quad (5.36)$$

Substituting the equations (5.33 – 2-layers) or (5.34 – 3-layers) for “ I_1 ” and (5.35 – 2-layers) or (5.36 – 3-layers) for “ I_2 ” of moment of inertia in equation (5.26):

$$k = \frac{E^*/4 b^3 d^3 t}{d^3 w^3 + b^3 a^3 + 3b^3 a^2 w + 3b^3 a w^2} \quad (5.37)$$

As in previous case, to obtain a dimensionless equation, it is necessary to reduce the equation (5.37) using parameters α , β and γ . The result presents all dimensionless parameters, except “ E^* ”, “ b ” and “ t ”:

$$k = \frac{E^*/4 b^3 \alpha^3 \beta^3}{t^2 (1 + \beta^3 \gamma^3 + 3\beta^2 \gamma^3 + 3\beta \gamma^3)} \quad (5.38)$$

5.3 Determination of First Natural Frequency “ ω_{1f} ”

Once the equations of stiffness in Bending 1 and Bending 2 in both cases of 2-layers and 3-layers was determined, it is possible to combine the equation of stiffness “ k ” and mass “ m ” following the (5.6). Therefore, the equation of first natural frequency in each analyzed case was calculated.

$$\omega_n = \sqrt{\frac{k}{m}} \quad (5.6)$$

The equations (5.32 – Bending 1) or (5.38 – Bending 2) of stiffness “k” and mass “m” was substituted in 5.13 or 5.19 (with appropriate ρ^*) in dimensionless parameters. After some simplifications, the final equations of first natural frequency in both case of Bending 1 and Bending 2 were found:

$$\omega_{1f-Bending1} = \frac{\alpha\beta}{2a} \sqrt{\frac{(E^*/\rho^*)}{\beta^2 + \frac{1}{\beta^2} + \beta(\gamma + 3) + \frac{1}{\beta}(3\gamma + \frac{1}{\gamma}) + 3\gamma + 3}} \quad (5.39)$$

$$\omega_{1f-Bending2} = \frac{d}{2t^2} \alpha^2 \beta \gamma \sqrt{\frac{(E^*/\rho^*)}{\frac{1}{\beta\gamma} + \beta^2\gamma^2 + 3\beta\gamma^2 + 3\gamma^2 + \frac{1}{\beta^2} + \beta\gamma^3 + 3\gamma^3 + 3\frac{\gamma^3}{\beta}}} \quad (5.40)$$

In the *table 5.11* and in *table 5.12*, there is a scheme of all models:

2-LAYERS MODEL

BENDING 1

BENDING 2

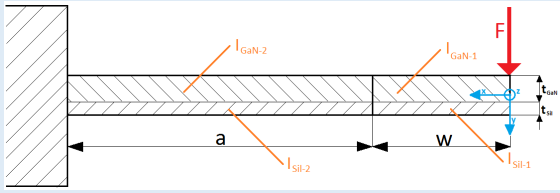
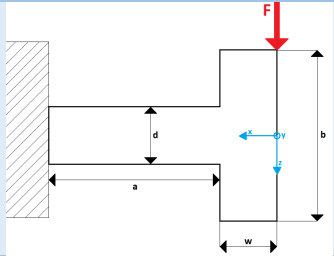
Figure		
Stiffness k [N/m]	$k = \frac{E^*/4 b \alpha^3 \beta^3}{1 + \gamma \beta^3 + 3\gamma \beta^2 + 3\gamma \beta}$	$k = \frac{E^*/4 b^3 \alpha^3 \beta^3}{t^2(1 + \beta^3 \gamma^3 + 3\beta^2 \gamma^3 + 3\beta \gamma^3)}$
Equivalent density ρ^* [kg/m ³]	$\rho^* = \rho_{GaN} p_{GaN} + \rho_{Si} p_{Si}$	$\rho^* = \rho_{GaN} p_{GaN} + \rho_{Si} p_{Si}$
Mass m [kg]	$m_{2-l} = \rho^* \frac{\alpha}{\beta} a^2 b \left(\frac{\beta}{\gamma} + 1 \right)$	$m_{2-l} = \rho^* \frac{\alpha}{\beta} a^2 b \left(\frac{\beta}{\gamma} + 1 \right)$
First Natural Frequency ω_{1f} [rad/s]	$\omega_{1f} = \frac{\alpha\beta}{2a} \sqrt{\frac{(E^*/\rho^*)}{\beta^2 + \frac{1}{\beta^2} + \beta(\gamma + 3) + \frac{1}{\beta}(3\gamma + \frac{1}{\gamma}) + 3\gamma + 3}}$	$\omega_{1f} = \frac{d}{2t^2} \alpha^2 \beta \gamma \sqrt{\frac{(E^*/\rho^*)}{\frac{1}{\beta\gamma} + \beta^2\gamma^2 + 3\beta\gamma^2 + 3\gamma^2 + \frac{1}{\beta^2} + \beta\gamma^3 + 3\gamma^3 + 3\frac{\gamma^3}{\beta}}}$

Table 5.11 – Scheme of 2-layers model in Bending 1 and Bending 2

3-LAYERS MODEL

BENDING 1

BENDING 2

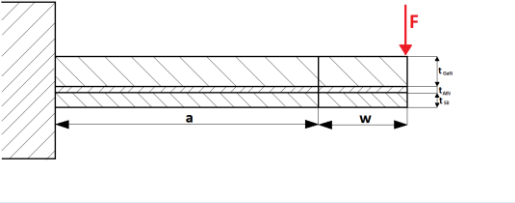
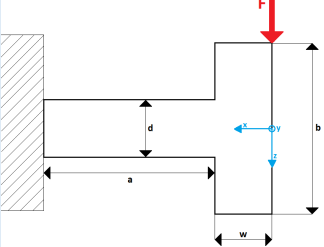
Figure		
Stiffness k [N/m]	$k = \frac{E^*/4 b \alpha^3 \beta^3}{1 + \gamma \beta^3 + 3\gamma \beta^2 + 3\gamma \beta}$	$k = \frac{E^*/4 b^3 \alpha^3 \beta^3}{t^2(1 + \beta^3 \gamma^3 + 3\beta^2 \gamma^3 + 3\beta \gamma^3)}$
Equivalent density ρ^* [kg/m ³]	$\rho^* = \rho_{GaN} p_{GaN} + \rho_{AlN} p_{AlN} + \rho_{SiI} p_{SiI}$	$\rho^* = \rho_{GaN} p_{GaN} + \rho_{AlN} p_{AlN} + \rho_{SiI} p_{SiI}$
Mass m [kg]	$m_{3-l} = \rho^* \frac{\alpha}{\beta} a^2 b \left(\frac{\beta}{\gamma} + 1 \right)$	$m_{3-l} = \rho^* \frac{\alpha}{\beta} a^2 b \left(\frac{\beta}{\gamma} + 1 \right)$
First Natural Frequency ω_{1f} [rad/s]	$\omega_{1f} = \frac{\alpha \beta}{2a} \sqrt{\frac{(E^*/\rho^*)}{\beta^2 + \frac{1}{\beta^2} + \beta(\gamma + 3) + \frac{1}{\beta} \left(3\gamma + \frac{1}{\gamma} \right) + 3\gamma + 3}}$	$\omega_{1f} = \frac{d}{2t^2} \alpha^2 \beta \gamma \sqrt{\frac{(E^*/\rho^*)}{\frac{1}{\beta \gamma} + \beta^2 \gamma^2 + 3\beta \gamma^2 + 3\gamma^2 + \frac{1}{\beta^2} + \beta \gamma^3 + 3\gamma^3 + 3\frac{\gamma^3}{\beta}}}$

Table 5.12 – Scheme of 3-layers model in Bending 1 and Bending 2

Each formula of first natural frequency can be rearranged in:

$$\frac{a \omega_{1f-Bending1}}{\sqrt{\frac{E^*}{\rho^*}}} = \frac{\alpha \beta}{2} \sqrt{\frac{1}{\beta^2 + \frac{1}{\beta^2} + \beta(\gamma + 3) + \frac{1}{\beta} \left(3\gamma + \frac{1}{\gamma} \right) + 3\gamma + 3}} \quad (5.41)$$

Plausible ranges of dimensionless parameters of real fabrication of micro cantilever beam are:

$$\begin{aligned} 0.05 &\leq \alpha \leq 0.1 \\ 4 &\leq \beta \leq 20 \\ 1 &\leq \gamma \leq 10 \end{aligned}$$

Variations of the bending frequency with dimensionless parameters are represented in *figure 5.13*, *figure 5.14* and *figure 5.15*:

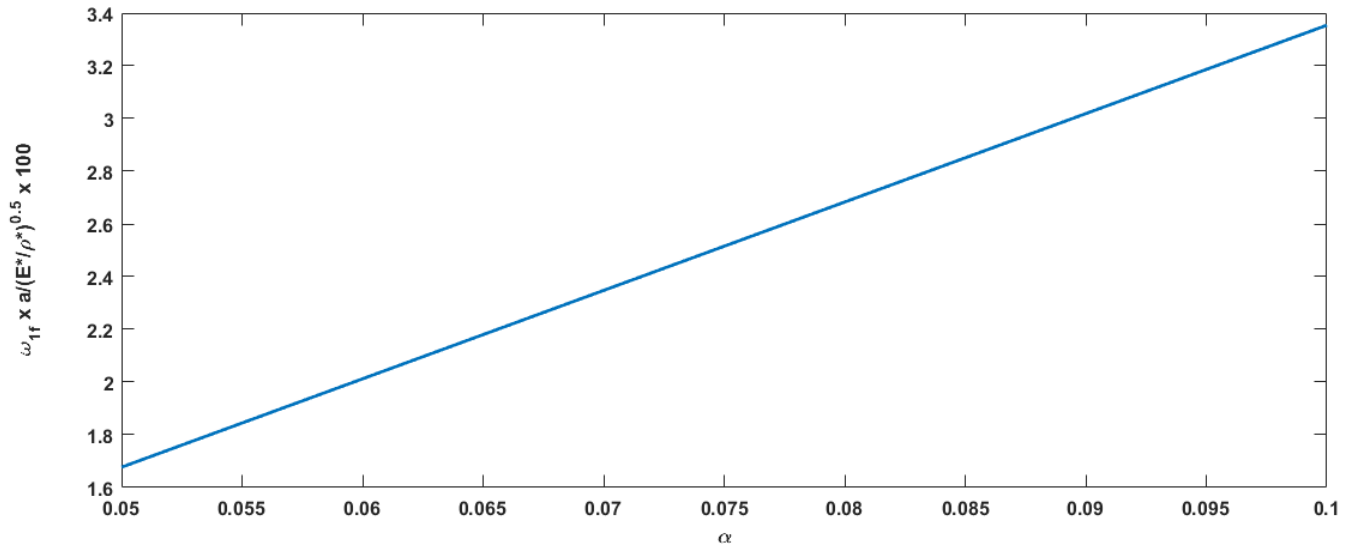


Figure 5.13 – Variation of first natural frequency in Bending 1, varying α and blocking β and γ

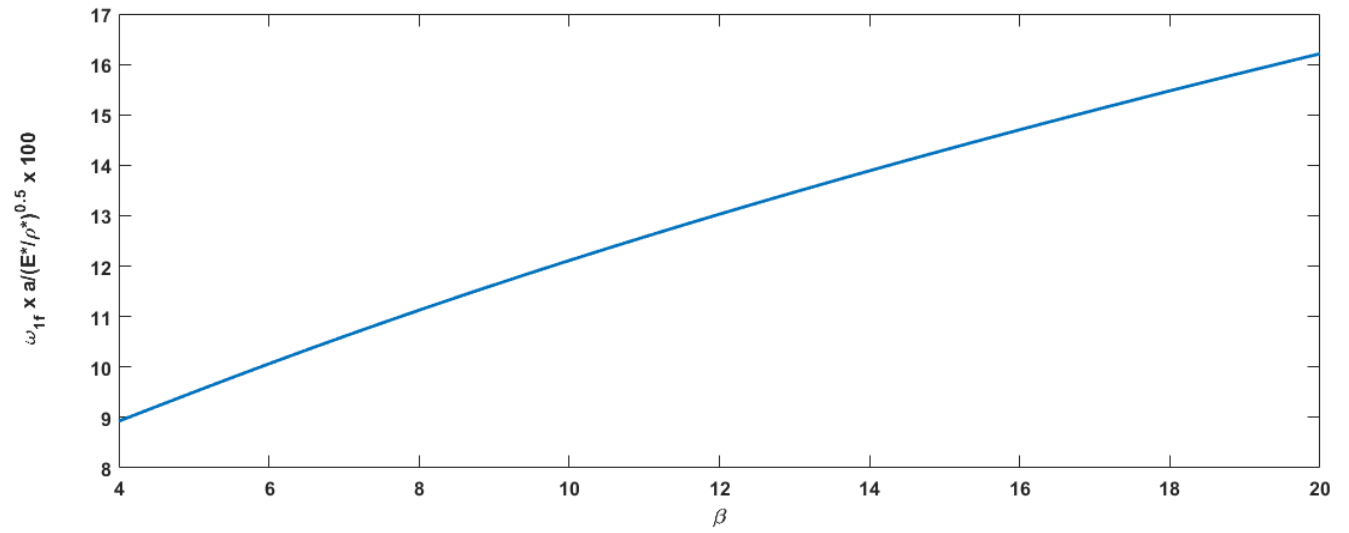


Figure 5.14 – Variation of first natural frequency in Bending 1, varying β and blocking α and γ

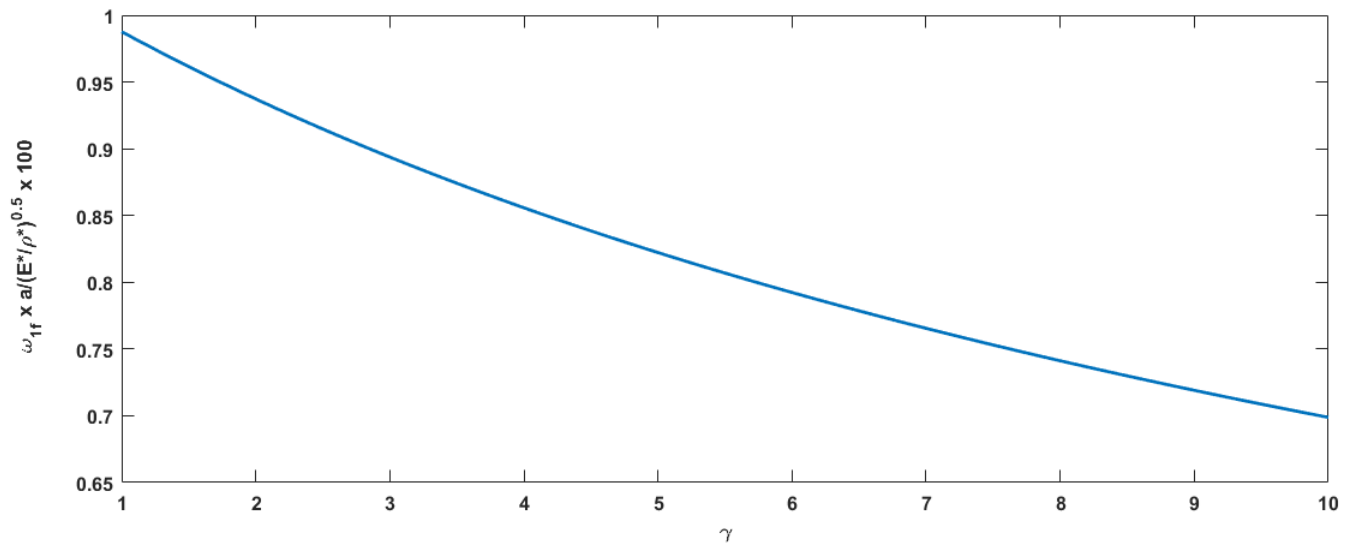


Figure 5.15 – Variation of first natural frequency in Bending 1, varying γ and blocking α and β

As regards Bending 2, the rearranged formula is:

$$\frac{2t^2 \omega_{1f-Bending2}}{d \sqrt{\frac{E^*}{\rho^*}}} = \alpha^2 \beta \gamma \sqrt{\frac{1}{\frac{1}{\beta \gamma} + \beta^2 \gamma^2 + 3\beta \gamma^2 + 3\gamma^2 + \frac{1}{\beta^2} + \beta \gamma^3 + 3\gamma^3 + 3\frac{\gamma^3}{\beta}}} \quad (5.42)$$

With same defined ranges of dimensionless parameters, doing the same proceeding, the three charts in figure 5.16, figure 5.17 and figure 5.18 results:

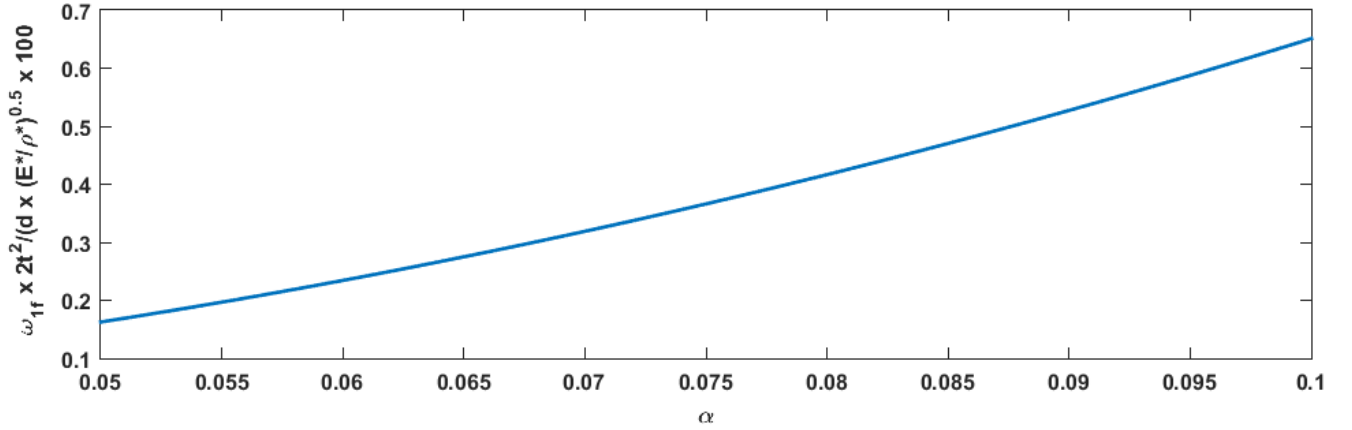


Figure 5.16 – Variation of first natural frequency in Bending 2, varying α and blocking β and γ

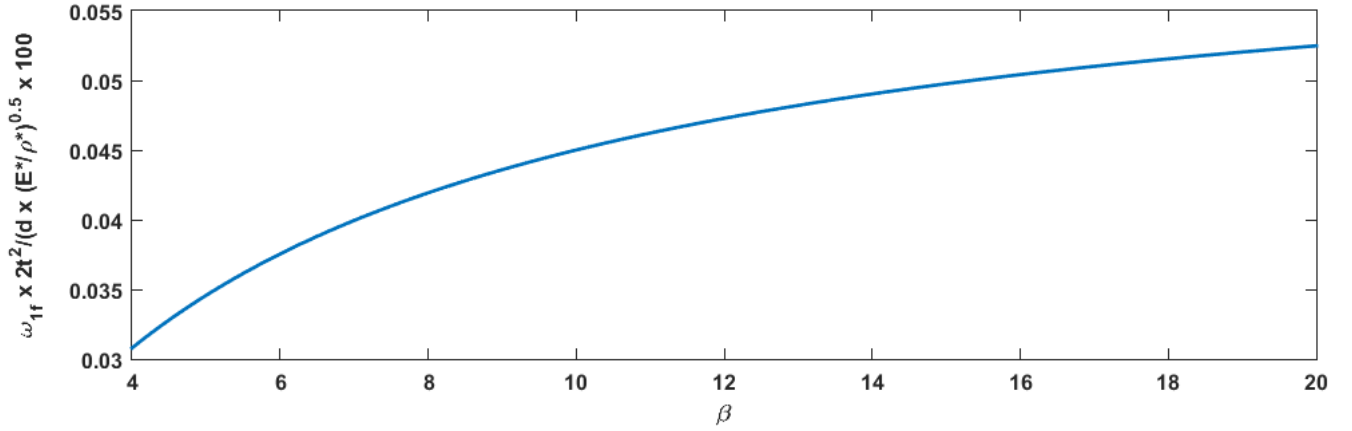


Figure 5.17 – Variation of first natural frequency in Bending 2, varying β and blocking α and γ

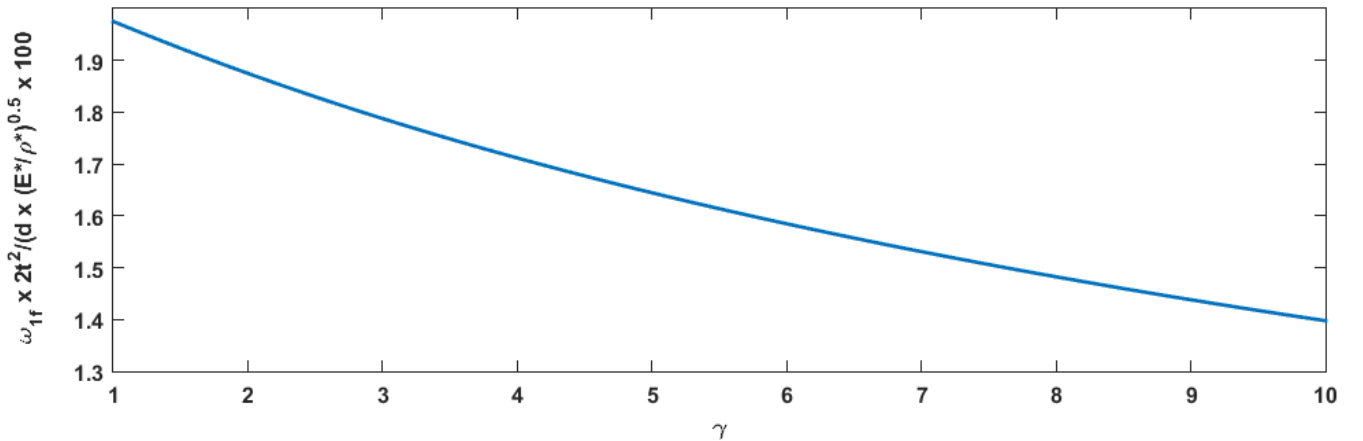


Figure 5.18 – Variation of first natural frequency in Bending 2, varying γ and blocking α and β

5.4 Determination of equivalent Young's modulus

The Young's modulus, known as elastic modulus, is the measure of stiffness of a solid material. It defines the relationship between stress (σ) and strain (ε) in a material:

$$E = \frac{\sigma}{\varepsilon} = \frac{F/A}{\Delta L/L_0} = \frac{FL_0}{A\Delta L}$$

Where:

σ = Stress;

ε = Strain;

Applying a load in a solid material, elastic deformation occurs if the material returns to original shape after removing the load. If the ratio between load and deformation remains constant, the stress-strain curve remain linear.

Theoretically, a rigid material has and infinite Young's modulus, but in presence of high Young's modulus, the material could be approximated as rigid. In opposite, in presence of low Young's modulus, the material is defined as soft.

The Young's modulus is not always the same in all orientation of the plan of a generic material. Many metals, for example, could be defined as isotropic, and their mechanical properties are the same in all orientation. Nevertheless, if they have impurities, it could become anisotropic, where the mechanical properties, including Young's Modulus, depend on direction of the force vector. The anisotropy can be seen as well in composites materials.

Until now, the Young's modulus "E" was used in calculation of stiffness "k" and consequently in first natural frequency " ω_{1f} " as "E* ". "E*" represents an equivalent Young's modulus, because the micro cantilever has 2-layers in first case and 3-layers in second case. The materials of micro cantilevers are GaN and Silicon in 2-layers case and GaN, AlN and Silicon in 3-layers case.

The materials are different. For example, in both cases there is Silicon. GaN and especially AlN are more rigid than silicon, so they have high Young's moduli. In *table 5.19*, there are the Young's Modulus of GaN, AlN and Silicon that will be used in following numerical simulations.

E_{GaN}	181 GPa
E_{AlN}	320 GPa
E_{Sil}	150 GPa

Table 5.19 – Young's Modulus of GaN, AlN and Silicon

However, the micro cantilevers are multilayer, so it is necessary to define an equivalent Young's modulus that considers the interaction between different materials, and defines a single equivalent material that contains the right mix of mechanical properties of all materials.

Before analysing the mathematical model to calculate the equivalent Young's Modulus, it is important to consider some simplified hypotheses:

- Each layer is considered perfect, without impurities and superficial defects.
- All materials that make up the multilayer are isotropic.
- The layers are blocked and glued between them. There is no possibility of sliding between different layers.

All these simplified hypotheses imply calculation errors. In fact, especially as regards superficial defects, there is the problem in fabrication of GaN-AlN-Silicon micro cantilevers: the substrate (originally not provided) of silicon results always with defects due to etching process that do not remove it completely. Therefore, the thickness of $0,5\ \mu\text{m}$ is not constant. These problems guarantee different values of mass, thickness and equivalent Young's Modulus of micro cantilevers. Therefore, the results of first natural frequency will have inside the cumulative errors of mass, thickness and Young's modulus.

In this mathematical model, two methods to define the equivalent Young's Modulus " E^* " were used. They are an approximate method, and more sophisticated Oberst's equation.

- 5.4.1 Approximate method for equivalent Young's modulus

The approximate method provides a weighted average of the single Young's modulus of each material of the multilayer on their cross sectional area. This model was called "approximated model", because it is a first calculation to test the model. This method in fact does not expect interaction between materials. It is a coarse method to calculate in quick way the equivalent Young's Modulus.

In both cases of 2-layers and 3-layers, respectively shown in *figure 5.20*, and in *figure 5.21*, the calculation of the equivalent Young's modulus was made on width " d ". Considering the calculation on width " b " the result will be the same, because the parameters " b " or " d " will be elide.

In this way, the approximate method gives a weighted average of the single Young's modulus on thicknesses of each material of multilayer.

As regards the calculation of the 2-layers case:

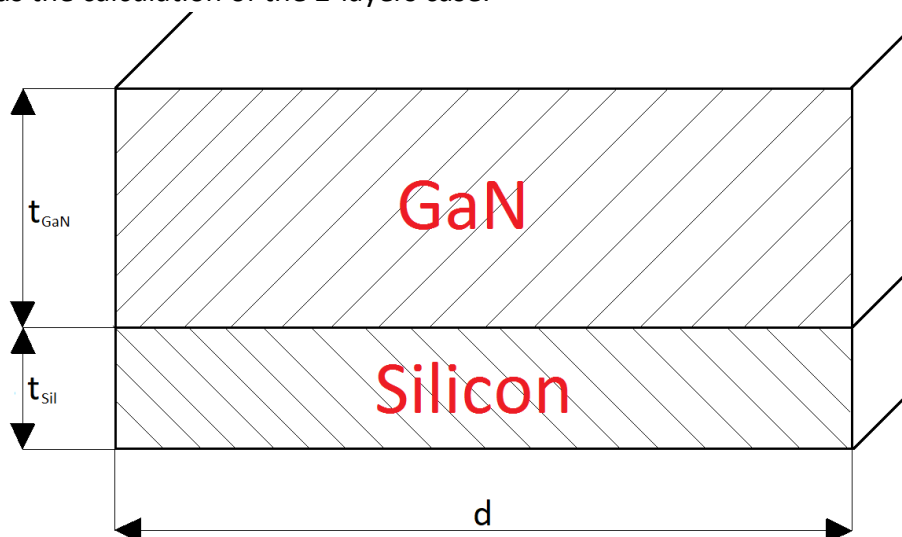


Figure 5.20 – Section of the beam in width " d " in 2-layers case

$$E_{2layer-approx}[d(t_{GaN} + t_{sil})] = E_{GaN}dt_{GaN} + E_{sil}dt_{sil}$$

$$E_{2layer-approx} = \frac{E_{GaN}t_{GaN} + E_{sil}t_{sil}}{(t_{GaN} + t_{sil})} \quad (5.43)$$

Instead, the calculation of the 3-layers case:

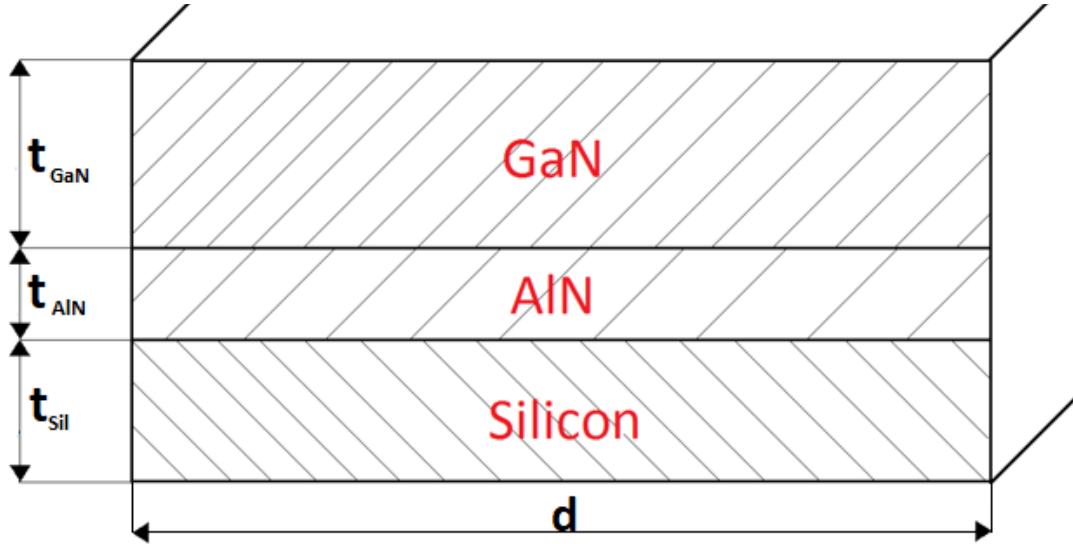


Figure 5.21 – Section of the beam in width “d” in 3-layers case

$$E_{3layer-approx}[d(t_{GaN} + t_{AlN} + t_{sil})] = E_{GaN}dt_{GaN} + E_{AlN}dt_{AlN} + E_{sil}dt_{sil}$$

$$E_{3layer-approx} = \frac{E_{GaN}t_{GaN} + E_{AlN}t_{AlN} + E_{sil}t_{sil}}{(t_{GaN} + t_{AlN} + t_{sil})} \quad (5.44)$$

The value of “E_{approx}” could be replaced in equations (5.39) and (5.40) respectively of first natural frequency in Bending 1 and Bending 2:

Before the Oberst’s Equation was treated, it is necessary to introduce the theory of viscoelastic materials.

- 5.4.2 Controlling vibration using viscoelastic damping [ref. 5.1]:

Viscoelastic materials are rubber-like, and possess stiffness and damping characteristics, that change strongly with frequency of vibration and temperature. However, these materials cannot be used to produce practical structures and machines, because sometimes they result too weak. Therefore, these viscoelastic materials should be added strategically to the structures to improve their characteristics.

The target of damping treatments is to add the viscoelastic material in different way and in such locations to guarantee that when the structure vibrates in the modes of interest, there is the greatest possible cyclic deformation of the damping material, to dissipate vibrational energy during each cycle as possible. This require the knowledge of mechanical behaviour of the structures, and the knowledge of the deformations of viscoelastic materials occurring during vibration. Therefore, it is necessary to know the complex modulus properties of the damping materials. Viscoelastic damping materials could be applied in extension, in shear, in extension/flexure and in shear/flexure. There are applications in which there is a partial coverage of viscoelastic material on structures, but just the case of full coverage of viscoelastic materials was treated.

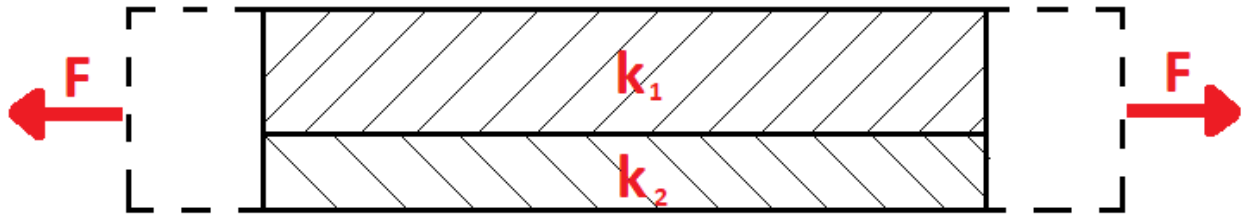


Figure 5.22 – Viscoelastic damping material (k_2) applied in parallel in extension [ref. 5.1]

For example, in deformation in extension (figure 5.22) during vibration, the calculation of equivalent stiffness is relatively simple. It results:

$$k^* = k_1 + k_2(1 + i\eta_2)$$

Where:

$k^* = k(1 + i\eta)$ – The complex stiffness of the composite;

k_1 – The initial stiffness of the structure layer;

$k_2(1 + i\eta_2)$ – The complex stiffness of the parallel viscoelastic layer.

Therefore, the effective stiffness “ k ” and loss factor “ η ” of the combined element are:

$$k = k_1 + k_2$$

$$\eta = \frac{\eta_2}{1 + k_2/k_1}$$

However, in this thesis, the simple case of deformation in extension is not treat. There is necessity to define a flexural solution.

There are two method to treat the flexural case:

- **5.4.2.1 Free layer treatments**

The simplest flexural damping system is the free layer treatment. It consists to apply a thickness of a viscoelastic material on a beam or plate to increase the damping. For sure, these treatments requires consistent values of thicknesses, Young’s moduli and loss factors, otherwise, the treatments result sometimes inefficient from weight point of view.

The flexural rigidity “(EI)*” changes due to new damping material, and it is calculated by Oberst’s equation.

Simple structures, rarely encountered in practice, help to understand basic principles. *Figure 5.23* shows a simple structure with free layer treatment that, according to Oberst, is deformed in flexure only. When the beam is cyclically deformed in flexure, the outer surface results stretched and inner surfaces results compressed. Each fibre of the viscoelastic material is deformed in extension during this deformation of the beam and creates a bending moments, which resists to flexural deformation.

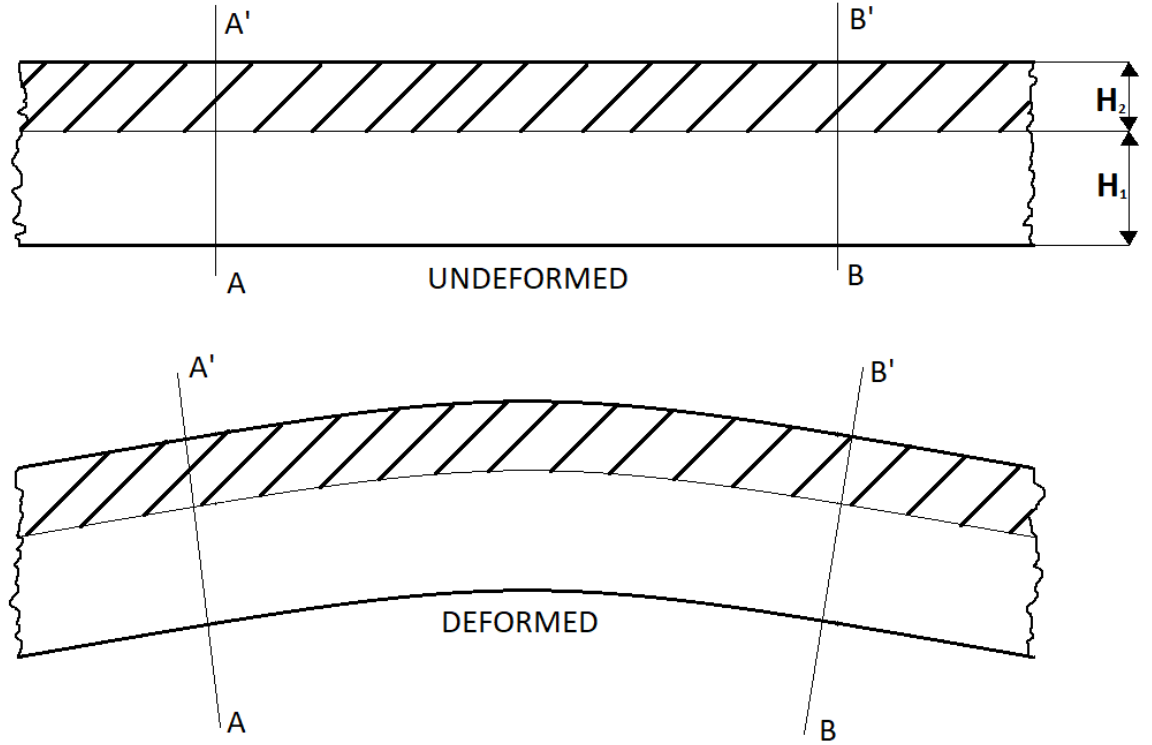


Figure 5.23 – Free layer treatment (thickness H_2) applied on structure layer (thickness H_1) in undeformed and deformed configuration [ref. 5.1]

The simplest form of the Oberst’s equation for a 2-layers, composite by a structure layer plus a viscoelastic damping material is:

$$\frac{(EI)^*}{E_1 I_1} = 1 + \frac{E_2^*}{E_1} \left(\frac{H_2}{H_1} \right)^3 + 3 \left(1 + \frac{H_2}{H_1} \right)^2 \frac{(E_2^*/E_1)(H_2/H_1)}{1 + (E_2^*/E_1)(H_2/H_1)} \quad (5.47)$$

Where “(EI)*” is the effective complex flexural rigidity of the structure beam plus viscoelastic material. “ E_1 ” is the Young’s modulus of the structure and “ E_2^* ” is the complex Young’s modulus of the viscoelastic damping material. H_1 and H_2 , as shown in *figure 5.23*, represent the thickness respectively of the layer structure and the viscoelastic layer.

$I_1 = \frac{b(H_1)^3}{12}$ represents the moment of inertia of structure layer, where

“b” and “H₁” are respectively the width and the thickness of the cross sectional area of the structure layer.

Another way to write the Oberst’s equation is:

$$\frac{(EI)^*}{E_1 I_1} = 1 + e^* h^3 + 3(1 + h)^2 \frac{e^* h}{1 + e^* h} \quad (5.48)$$

Where:

$$h = H_2 / H_1 ;$$

$$e^* = E_2^* / E_1 ;$$

$$I_1 = b H_1^3 / 12 ;$$

- **5.4.2.2 Constrained layer damping treatments**

A complicated flexural damping treatment is when, another elastic material like a metal sheet or plate caps a viscoelastic layer. It is called constrained layer damping treatment. In this case, there are at least three materials in multilayer, where the inner layer is a viscoelastic material (thickness “H₂”), and the two outer layers are, the first made by the initial material of structure (thickness “H₁”), and the last one made by the elastic layer in order to cap the viscoelastic layer (thickness H₃). In this case it is hard to calculate the effective flexural modulus “(EI)*”, because it depends on boundary conditions, modal shape, dimensions and damping material complex modulus.

Figure 5.24 illustrates the deformation of single constrained damping layer pair on a simple beam.

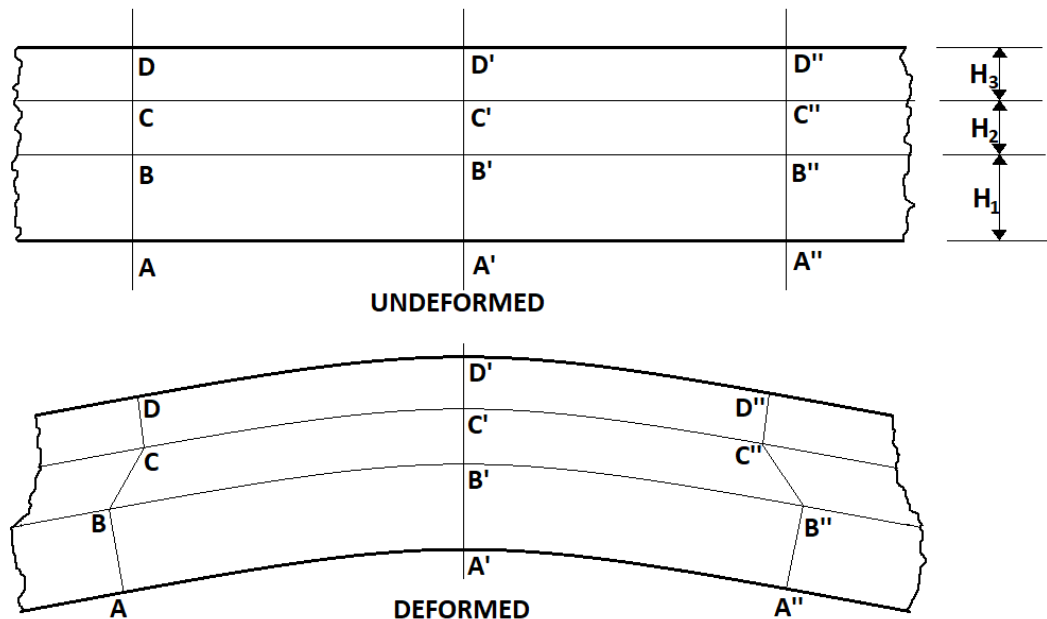


Figure 5.24 – Deformation in a constrained layer treatment [ref. 5.1]

The Ross-Kerwin-Ungar equation (RKU equations) defines the model of constrained layer damping treatments. These equations depends on assumption that flexural deformation of the beam during vibration is spatially sinusoidal in shape. The original model provides that the RKU equations are only applicable for beams having pinned-pinned boundary conditions. Nevertheless, Rao developed exact solutions of this equation, using the Euler-Bernoulli beam theory, providing correction factors for other boundary conditions. The set of RKU equations for a single constrained layer pair damping treatment are usually written in the form (for pinned-pinned boundary condition):

$$(EI)^* = \frac{E_1 H_1^3}{12} + \frac{E_2^* H_2^3}{12} + \frac{E_3 H_3^3}{12} - \frac{E_2^* H_2^2}{12} \left(\frac{H_{31} - D}{1 + g^*} \right) + E_1 H_1 D^2 + E_2^* H_2 (H_{21} - D)^2 + E_3 H_3 (H_{31} - D)^2 - [0.5 E_2^* H_2 (H_{21} - D) + E_3 H_3 (H_{31} - D)] \left(\frac{H_{31} - D}{1 + g^*} \right) \quad (5.49)$$

With:

$$D = \frac{E_2^* H_2 (H_{21} - 0.5 H_{31}) + g^* (E_2^* H_2 H_{21} + E_3 H_3 H_{31})}{E_1 H_1 + 0.5 E_2^* H_2 + g^* (E_1 H_1 + E_2 H_2 + E_3 H_3)}$$

$$H_{21} = 0.5(H_1 + H_2)$$

$$H_{31} = H_2 + 0.5(H_1 + H_3)$$

$$g^* = \frac{G_2^* \lambda^2}{E_3 H_2 H_3 \pi^2}$$

Where:

E_1 = Young's modulus of structure layer;

E_2^* = Young's modulus of damping layer;

E_3 = Young's modulus of elastic layer;

G_2^* = Shear modulus of damping layer.

λ = Semi wavelength of vibration in pinned-pinned boundary condition.

Each term of “(EI)*” represents: the first, second and third term represent the flexural rigidities of three layers of their own neutral axes; the term “D” defines the neutral axis for the composite beam. The parameter “g*” is the “shear parameter” and it varies from a low number to a high number if “G₂*” is small or large. The Young's Modulus “E₂*” is complex as well as “G₂*”, while “E₃” could be complex if a damping material is used as constraining layer.

The simplest form of the RKU equation is the “sandwich configuration”. It requires that “H₁” layer is equal to “H₃”, and the “H₂” is much lower than outer layers. In this case the effect of the inner layer “E₂” is negligible:

$$(EI)^* = 2E_1I_1 + E_1H_1(H_1 + H_2) \frac{g^*}{1 + 2g^*} \quad (5.50)$$

In this case, “I₁” represents the moment of inertia of the structure layer.

Rao’s studies guarantee the solutions of RKU equations with other boundary conditions. In fact, the value of the semi wavelength “λ” used in calculation of “g*”, corresponds to the length of pinned-pinned beam of the same thickness which has the same resonant frequency as the actual beam. The first frequency of pinned-pinned beam is given by:

$$\frac{\rho_1 b H_1 \omega_n^2 \lambda_n^4}{E_1 I_1} = \pi^4$$

Where:

ρ₁ = Density of the structure layer;

b = Width of the beam;

ω_n = The resonant frequency;

The nth modal frequency of the beam with other boundary conditions is given by:

$$\frac{\rho_1 b H_1 \omega_n^2 L^4}{E_1 I_1} = \xi_n^4$$

With:

L = Length of the beam;

$$\lambda_n = \frac{\pi L}{\xi_n}$$

Rao’s studies refers just on first and second mode of vibration. Above the third mode, the corrections are very small. There is a correction factor for each boundary condition. This factor influence just the equation of shear parameter “g*”, because it is the only that depends from semi wavelength “λ”.

The parameter “g*” become for other boundary conditions:

$$g^* = \frac{G_2^* L^2}{E_3 H_2 H_3 \xi_n^2 \sqrt{C_n}}$$

Therefore, the parameter “ λ_n ” become with Rao’s correction factor “ C_n ”:

$$\lambda_n = \frac{\pi L}{\xi_n \sqrt{C_n}}$$

The *table 5.25* summarises some of these corrections obtained from Rao’s studies comparing with RKU equations.

BOUNDARY CONDITIONS	CORRECTION FACTOR “ C_n ”	
	MODE 1	MODE 2+
PINNED-PINNED	1.0	1.0
CLAMPED-CLAMPED	1.4	1.0
CLAMPED-PINNED	1.0	1.0
CLAMPED-FREE	0.9	1.0
FREE-FREE	1.0	1.0

Table 5.25 – Rao’s correction factor for each boundary condition

Constrained layer treatments are more efficient than free layer treatments, but the third layer add weight to the structure. Sometimes if structures are very complicated, they require an analysis by finite element (FEM).

The costs of materials and the costs of working process in free layer treatments result often lower than constrained layer damping treatments.

An important consideration is that when “ H_3 ” approaches to zero, the RKU equation is reduced to Oberst’s equation.

- 5.4.3 Oberst’s equation for equivalent Young’s modulus

An interesting way to write the Oberst’s equation showed in [5.4.2.1] in equation (5.48) is:

$$\frac{(EI)^*}{E_1 I_1} = [A^* + B^* e^*] \quad (5.51)$$

Where:

$$A^* = \frac{(1 - h^2 e^*) + [1 + (2h + h^2) e^*]^3}{2(1 + h e^*)^3}$$

$$B^* = \frac{(1 + 2h - h^2 e^*)^3 - (1 - h^2 e^*)^3}{2(1 + h e^*)^3}$$

With:

$$h = H_2 / H_1;$$

$$e^* = E_2^* / E_1;$$

$$I_1 = b H_1^3 / 12;$$

The subscripts (1) or (2) represents the reference layers.

In this case, Oberst's equation shows the way to calculate a 2-layers case of free layer damping treatment. In theory, in free layer treatments, there is an application of Oberst's equation to calculate multilayer cases based on the two layers procedure. In particular, in 3-layers case:

$$\frac{(EI)^*}{E_1 I_1} = [A_1^* + e_2^* B_1 + e_3^* C_1] \quad (5.52)$$

Where:

$$A_1^* = 4[m^3 + (1 - m)^3]$$

$$B_1 = 4[(m + h_2)^3 - m]$$

$$C_1 = 4[(m + h_2 + h_3)^3 - (m + h_2)^3]$$

$$m = \frac{1 - e_2^* h_2^2 - e_3^* h_3 (2h_2 + h_3)}{2[1 + e_2^* h_2 + e_3^* h_3]}$$

Where:

$$h_2 = H_2 / H_1;$$

$$h_3 = H_3 / H_1;$$

$$e_2^* = E_2^* / E_1;$$

$$e_3^* = E_3^* / E_1;$$

$$I_1 = b H_1^3 / 12$$

It is simple to notice, when “ e_3^* ” and/or “ h_3 ” are zero these equations reduce to Oberst's equation of 2-layers case. This theory can be applied only when two damping layers are bounded on structural base beam. To make the theory work, the outer layer must be softer than inner damping layer, so that the condition “plane section must remain plane” of free layer treatment is not violated. Otherwise, the third layer could be considered as a constraining layer, as discussed in paragraph [5.4.2.2]. In this case, the effectiveness of third layer is reduced.

The variation of the real part of “ $(EI)^*$ ”, “ e ” and “ h ” provides a useful values of the quantities of damping, which could be determined applying a damping layer, where complex properties are known.

Oberst's equation in 2-layers and 3-layers of free layer treatments were applied in T-shape cantilever treated in this thesis. Therefore, there is necessity to make some considerations:

- Both 3-layers case and 2-layers case do not consider damping materials, therefore, null damping on micro cantilever is obtained;
- Without damping, "e*" become "e", because just the real part of the "silicon" and "AlN" layers were considered, and not the complex Young's modulus (typical of damping materials);
- In the same way, as regards 2-layers case, the result gives just the real part of "EI*". Therefore, "EI*" become "EI", as "A*" become "A" and "B*" become "B". As regards 3-layers case, the situation is the same.

As regards 2-layers case, writing again the Oberst's equation:

$$\frac{(EI)}{E_{GaN}I_1} = [A + eB] \quad (5.53)$$

Where:

$$A = \frac{(1 - h^2e) + [1 + (2h + h^2)e]^3}{2(1 + he)^3} \quad (5.54)$$

$$B = \frac{(1 + 2h - h^2e)^3 - (1 - h^2e)^3}{2(1 + he)^3} \quad (5.55)$$

With:

$$h = t_{sil}/t_{GaN};$$

$$e = E_{sil}/E_{GaN};$$

$$I_1 = bt_{GaN}^3/12;$$

As regards 3-layers case, the Oberst's equation:

$$\frac{(EI)}{E_{GaN}I_1} = [A_1 + e_2B_1 + e_3C_1] \quad (5.56)$$

$$A_1 = 4[m^3 + (1 - m)^3] \quad (5.57)$$

$$B_1 = 4[(m + h^2)^3 - m] \quad (5.58)$$

$$C_1 = 4[(m + h_2 + h_3)^3 - (m + h_2)^3] \quad (5.59)$$

$$m = \frac{1 - e_2h_2^2 - e_3h_3(2h_2 + h_3)}{2[1 + e_2h_2 + e_3h_3]} \quad (5.60)$$

Where:

$$h_2 = t_{AlN}/t_{GaN};$$

$$h_3 = t_{SiI}/t_{GaN};$$

$$e_2 = E_{AlN}/E_{GaN};$$

$$e_3 = E_{SiI}/E_{GaN};$$

$$I_1 = bt_{GaN}^3/12$$

The micro cantilever has not the same cross sectional area, but it has, as widely explained, the T-shape. Therefore, there is necessity, implementing Oberst's equation, to calculate again the stiffness "k" in cases of Bending 1 and Bending 2 and in 2-layers and 3-layers cases. Mixing it with mass (that remains the same), the first natural frequency can be calculated in these cases:

• **5.4.3.1 First natural frequency in Bending 1 in 2-layers configuration implementing Oberst's equation**

As in paragraph [5.2.1], on figure 5.26, the strain energy was calculated:

$$U = \int_0^w \frac{M^2(x)}{2(EI)_1} dx + \int_w^{w+a} \frac{M^2(x)}{2(EI)_2} dx \quad (5.61)$$

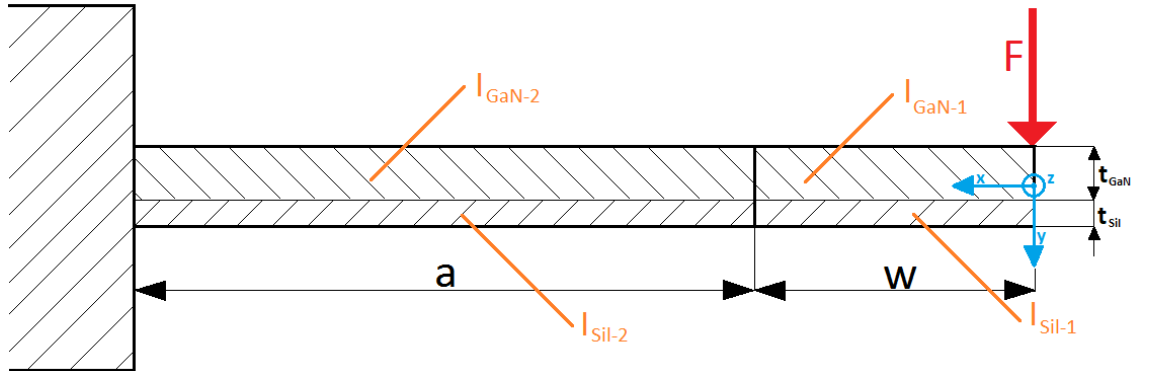


Figure 5.26 – Representation of micro cantilever in 2-layers case on x-y plane (Bending 1)

The values of "EI" could be obtained from the Oberst's equations in (5.53):

$$(EI)_1 = E_{GaN}I_{GaN-1}[A_1 + e_1B_1] \quad (5.62)$$

$$(EI)_2 = E_{GaN}I_{GaN-2}[A_2 + e_2B_2] \quad (5.63)$$

As defined before, the parameters "A₁", "A₂", "B₁", "B₂", "e₁" and "e₂" depend on thicknesses and Young's moduli of materials, that don't change along the x-axis. Therefore, A₁ = A₂ = A and B₁ = B₂ = B and e₁ = e₂ = e.

Replacing (5.62) and (5.63) in (5.61) and solving the integrals:

$$U = \frac{F^2}{6E_{GaN}I_{GaN-1}[A + eB]}w^3 + \frac{F^2}{6E_{GaN}I_{GaN-2}[A + eB]}[a^3 + 3a^2w + 3w^2a] \quad (5.64)$$

From strain energy “U”, the maximum deflection “ δ ” (where the load is applied) was obtained with the same procedure of paragraph [5.2.1]:

$$\delta(x = 0) = \frac{F[I_{GaN-2}w^3 + I_{GaN-1}(a^3 + 3a^2w + 3aw^2)]}{3I_{GaN-1}I_{GaN-2}E_{GaN}[A + eB]} \quad (5.65)$$

The stiffness results:

$$k = \frac{F}{\delta} = \frac{3E_{GaN}[A + eB]I_{GaN-1}I_{GaN-2}}{I_{GaN-2}w^3 + I_{GaN-1}a^3 + 3I_{GaN-1}a^2w + 3I_{GaN-1}aw^2} \quad (5.66)$$

Defining the moment of inertia as:

$$I_{GaN-1} = \frac{b(t_{GaN})^3}{12} = \frac{bp_{GaN}^3t^3}{12} \quad (5.67)$$

$$I_{GaN-2} = \frac{d(t_{GaN})^3}{12} = \frac{dp_{GaN}^3t^3}{12} \quad (5.68)$$

Where:

$$t = t_{GaN} + t_{Si}$$

$$p_{GaN} = t_{GaN}/t$$

Substituting in equation (5.66) the dimensionless parameters and moments of inertia:

$$k = \frac{E_{GaN}/4 p_{GaN}^3[A + eB]b\alpha^3\beta^3}{1 + \gamma\beta^3 + 3\gamma\beta^2 + 3\gamma\beta} \quad (5.69)$$

The first natural frequency, using the mass of 2-layers model defined in [5.1.1], results:

$$\omega_{1f-2layer-Bending1} = \frac{\alpha\beta}{2a} \sqrt{\frac{p_{GaN}^3 \left(\frac{E_{GaN}}{\rho^*} \right) [A + eB]}{\beta^2 + \frac{1}{\beta^2} + \beta(\gamma + 3) + \frac{1}{\beta} \left(3\gamma + \frac{1}{\gamma} \right) + 3\gamma + 3}} \quad (5.70)$$

Rewriting the first natural frequency in (5.39), defined in paragraph [5.3]:

$$\omega_{1f-Bending1} = \frac{\alpha\beta}{2a} \sqrt{\frac{\left(E^* / \rho^* \right)}{\beta^2 + \frac{1}{\beta^2} + \beta(\gamma + 3) + \frac{1}{\beta} \left(3\gamma + \frac{1}{\gamma} \right) + 3\gamma + 3}} \quad (5.39)$$

Comparing the equations (5.70) and (5.39), the value of equivalent Young's modulus "E_{2layer-Oberst}" was determined:

$$E_{2layer-Oberst} = p_{GaN}^3 E_{GaN} (A + eB) \quad (5.71)$$

• 5.4.3.2 First natural frequency in Bending 1 in 3-layers configuration implementing Oberst's equation

In the same way of 2-layers case, the values of "EI" in 3-layers case could be obtained from the Oberst's equation of 3-layers case (in figure 5.27) in equation (5.54):

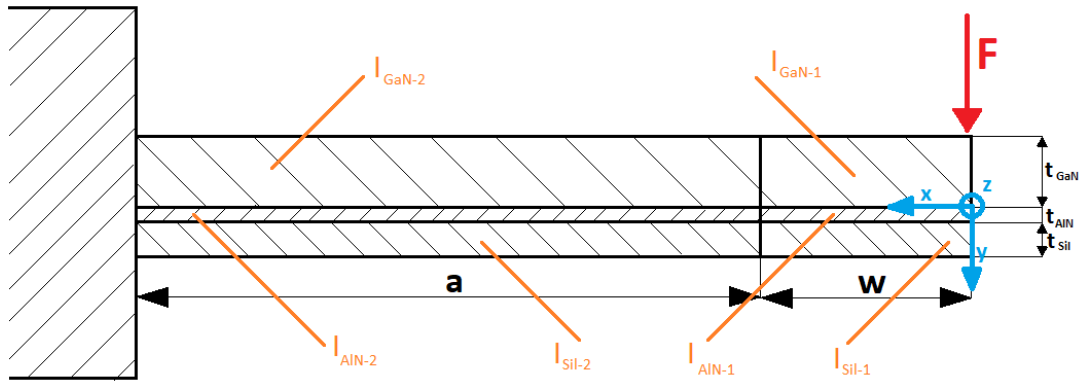


Figure 5.27 – Representation of micro cantilever in 3-layers case on x-y plane (Bending 1)

$$(EI)_1 = E_{GaN} I_{GaN-1} [A_{1-1} + e_2 B_{1-1} + e_3 C_{1-1}] \quad (5.72)$$

$$(EI)_2 = E_{GaN} I_{GaN-2} [A_{1-2} + e_2 B_{1-2} + e_3 C_{1-2}] \quad (5.73)$$

As defined before, the parameters "A₁₋₁", "A₁₋₂", "B₁₋₁", "B₁₋₂", "e₂" and "e₃" depend on thicknesses and Young's moduli of materials, that don't change along the x-axis. Therefore, A₁₋₁ = A₁₋₂ = A₁, B₁₋₁ = B₁₋₂ = B₁, C₁₋₁ = C₁₋₂ = C₁ defined in equations

Substituting the equations (5.66) and (5.67) in the strain energy (that is the same of 2-layers case) in equation (5.61), and solving in the same way of 2-layers case, the equation of first natural frequency was obtained for 3-layers case:

$$\omega_{1f-3layer-Bending1} = \frac{\alpha\beta}{2a} \sqrt{\frac{p_{GaN}^3 \left(\frac{E_{GaN}}{\rho^*} \right) [A_1 + e_2 B_1 + e_3 C_1]}{\beta^2 + \frac{1}{\beta^2} + \beta(\gamma + 3) + \frac{1}{\beta} \left(3\gamma + \frac{1}{\gamma} \right) + 3\gamma + 3}} \quad (5.74)$$

Comparing the equation (5.74) to (5.39), the value of equivalent Young's modulus "E_{3layer-Oberst}" was obtained:

$$E_{3layer-Oberst} = p_{GaN}^3 E_{GaN} (A_1 + e_2 B_1 + e_3 C_1) \quad (5.75)$$

- **5.4.3.3 First natural frequencies in Bending 2 implementing Oberst's equation**
Unfortunately, Oberst's theory is not valid in case where the load is parallel to separation line between two layers of a multilayer, as in the case treated in this thesis, in figure 5.28:

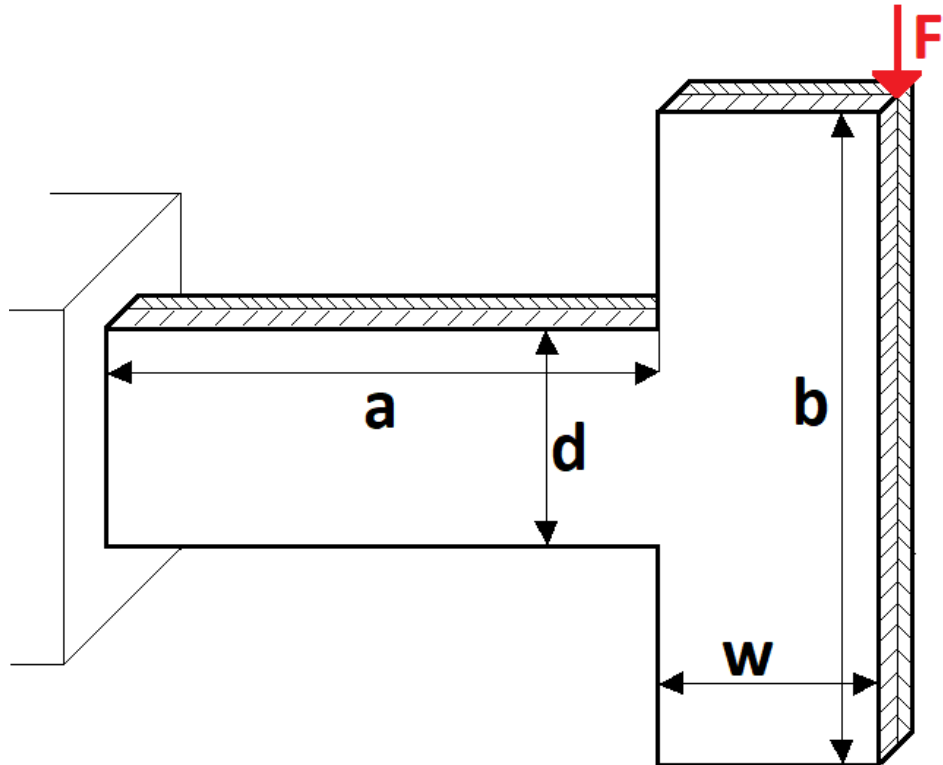


Figure 5.28 – Representation of micro cantilever in 2-layers case on x-z plane (Bending 2)

Therefore, in case of Bending 2 in 2-layers and in 3-layers the Oberst's equation cannot be used. Just the approximate method can be helpful.

6. COMPARISON OF RESULTS OF MATHEMATICAL MODEL, FEM AND EXPERIMENTAL TESTS

In this chapter, the results of the mathematical model explained in chapter 5, will be analyzed comparing it both with the results obtained by FEM in Solidworks and the results obtained from the experimental tests with laser vibrometer in the laboratories of Bristol University.

The experiments were conducted just on two cantilevers (Cantilever 1 and Cantilever 2) with different geometrical dimensions. The inconvenience is that these two cantilevers were made by 3-layers (GaN + AlN + Silicon). As explained in chapter 4, there are not results available for 2-layers model.

6.1 Modeling of the micro cantilever by Finite Element Model (FEM)

A finite element model (FEM) has been defined to check if the simple mathematical models presented in chapter 5 are accurate enough in describing the 2-layers and 3-layers configurations. Solidworks® was used to model the micro cantilever realizing an assembly made by two layers and three layer. About each modelled layer were included in Solidworks the mechanical characteristics, such as Young's Moduli and Poisson ratios. The layers were perfectly bounded each other. Four assembly were realized:

- Cantilever 1 in 2-layers model (GaN + Silicon);
- Cantilever 2 in 2-layers model (GaN + Silicon);
- Cantilever 1 in 3-layers model (GaN + AlN + Silicon);
- Cantilever 2 in 3-layers model (GaN + AlN + Silicon).

After modelling the assembly, "Solidworks Simulation" was used to obtain the results in term of resonance frequencies. The structures are simple; therefore, the maximum number of nodes were used to mesh the model, to reach a good precision.

Each assembly in Solidworks simulation give the first five resonance frequencies. Only two frequencies of the micro cantilevers (Bending 1 and Bending 2) were considered. Other three deformation of the micro cantilevers give the resonance frequencies of other modes, e.g. torsion. *Figures 6.1 and 6.2* show 2 assemblies with their deformations. They represent the Cantilever 1 in case of Bending 1. In the same way, the other assemblies are realized and analysed in "Solidworks Simulation"

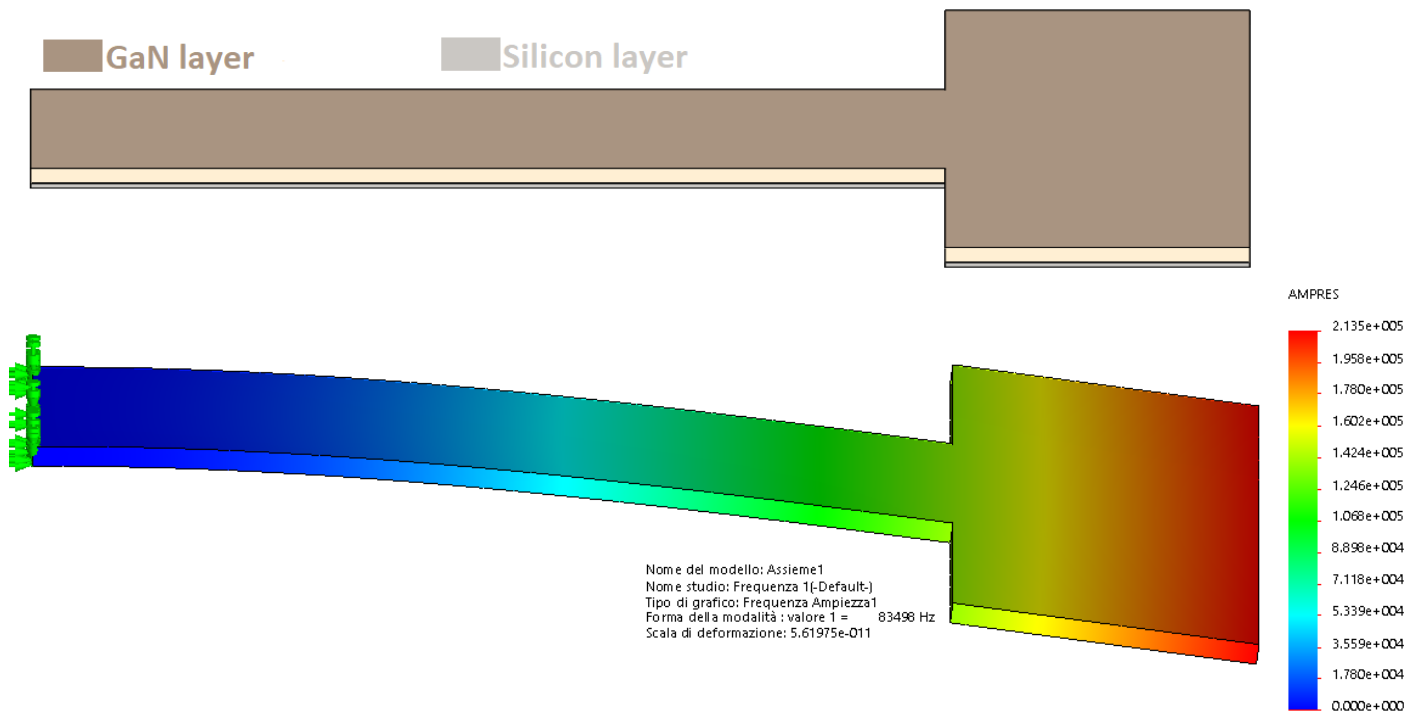


Figure 6.1 – Cantilever 1 in 2-layers configuration in Bending 1

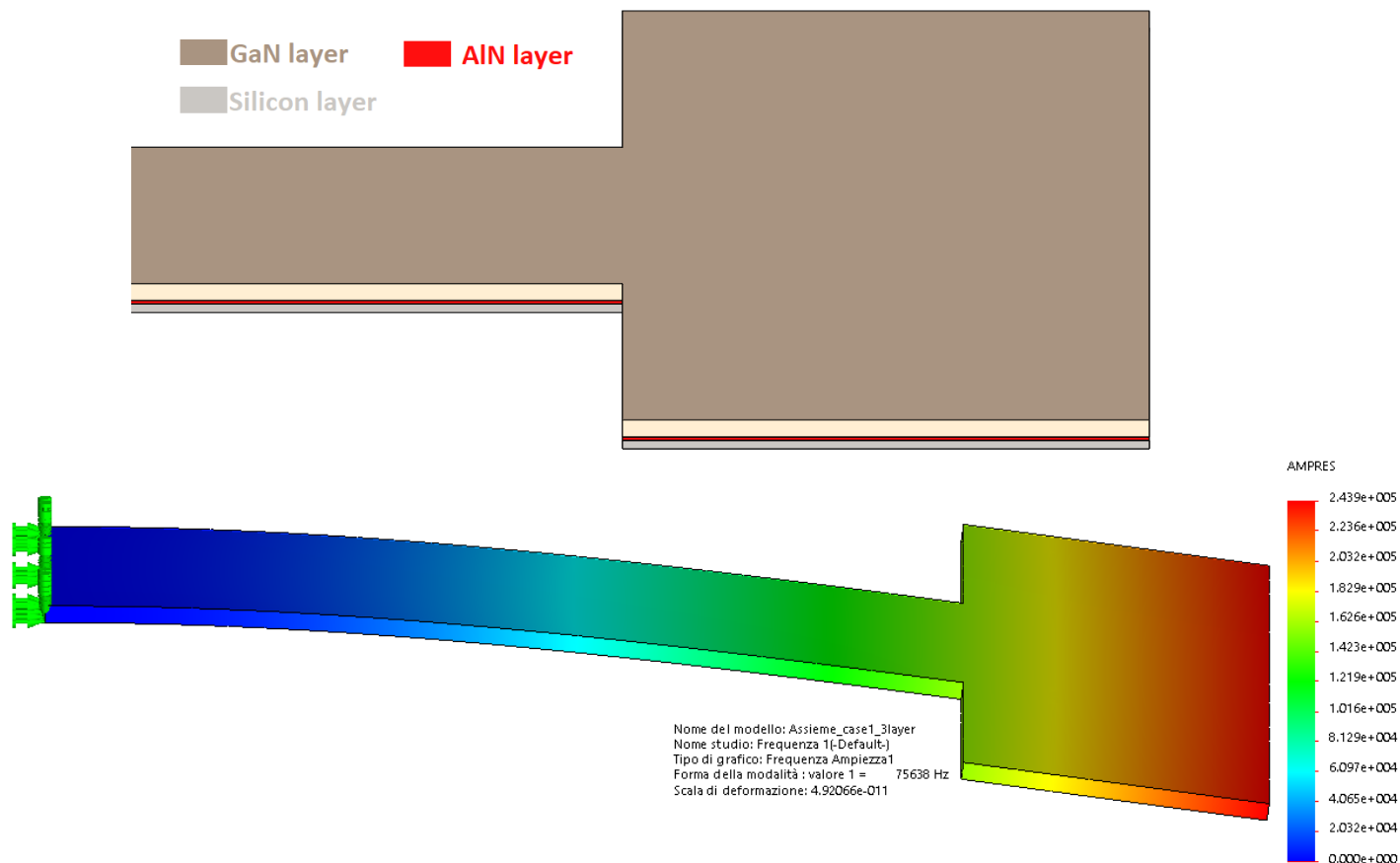


Figure 6.2 – Cantilever 1 in 3-layers configuration in Bending 1

As regards Bending 2, the results obtained in Solidworks are showed in *figures 6.3*. This is just an example of Cantilever 1 in Bending 2. As regards other cases of Bending 2, they however were modelled and analysed.

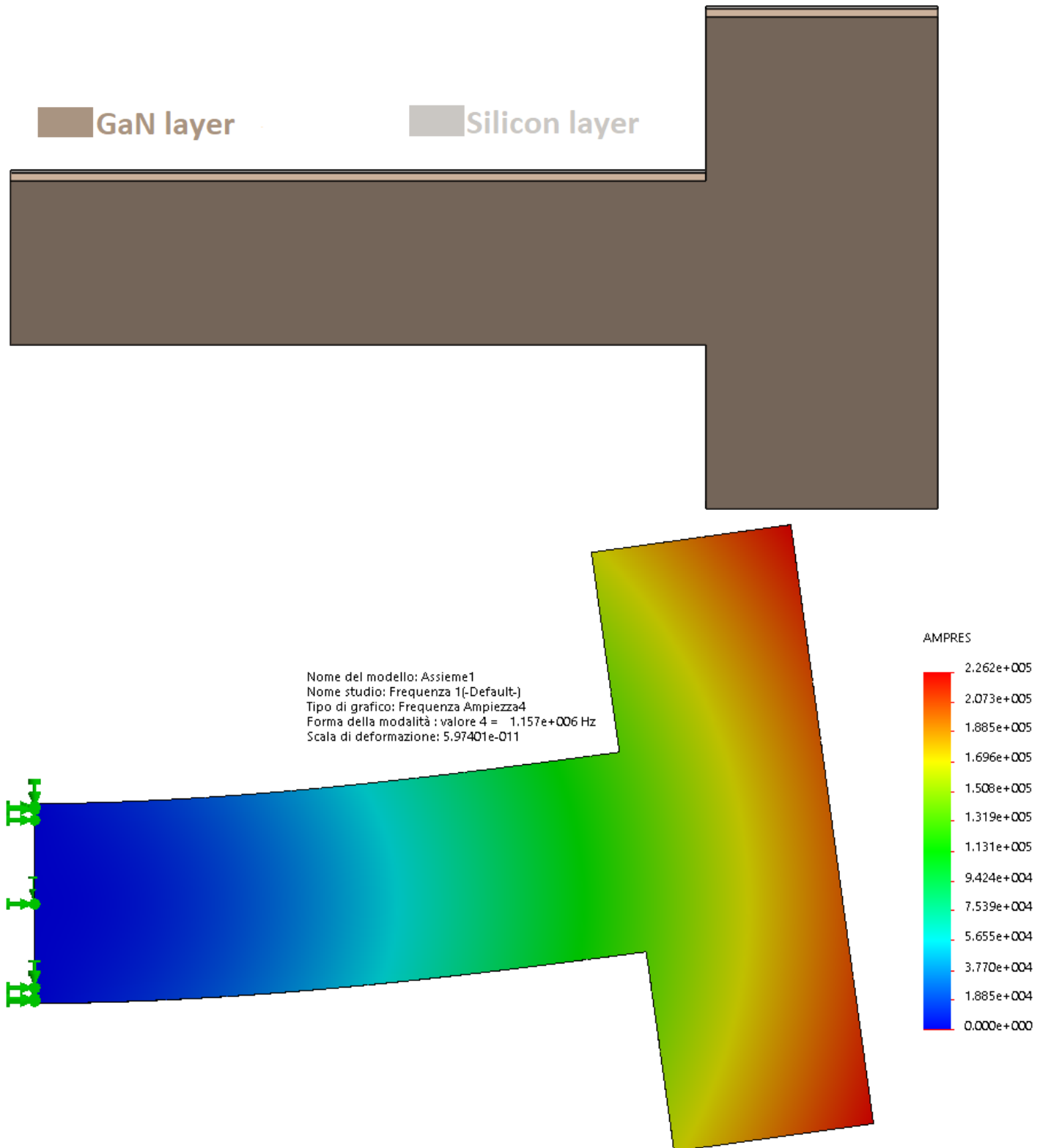


Figure 6.3 – Cantilever 1 in 2-layers configuration in Bending 2

6.2 Comparison of results between experimental test, FEM and mathematical model.

As explained in chapter 4, in laboratories of University of Bristol the experiment of measurements were conducted just on Cantilever 1 and Cantilever 2, both in case of Bending 1. Unfortunately, the experiments were not conducted in case of Bending 2, due to unavailability of the micro cantilevers. Therefore, the experimental results are not available. In this thesis were treated four cases for Bending 1, which include two cases for 2-layers and two cases for 3-layers, and four cases for Bending 2, which include two cases for 2-layers and two cases for 3-layers. Nevertheless, on eight total cases, there are only two available experimental results. In *table 6.9*, there is the comparison between the two experimental results and the same results obtained by FEM in Solidworks. Since they are acceptable, the mathematical model will be compared to FEM for other cases. To calculate the percentage errors, the expression 6.1 was used:

$$\text{Percentage error} = \frac{\text{Experimental result} - \text{FEM result}}{\text{Experimental result}} \times 100 \quad (6.1)$$

BENDING 1			
	RESONANCE FREQUENCY [kHz]		Percentage error [%]
	Experimental	FEM	
Cantilever 1	75.3	75,638	0.45
Cantilever 2	55.5	56,584	1,95

Table 6.9 – Comparison between experimental results and FEM results

The percentage errors between experimental results and FEM results are very low. Therefore, there is excellent agreement so it is possible to compare the mathematical model and FEM results. Obtaining good results in term of mathematical model, the purpose of this thesis will be reached.

Table 6.10, 6.11, 6.12 and 6.13 list the experimental results (where available), FEM results (obtained in Solidworks) and mathematical model results (obtained by formulas in chapter 5, in table 5.12, substituting the equivalent Young's moduli with "E* approximate" and "E* Oberst"). Finally, percentage errors between FEM and mathematical model are given by:

$$\text{Percentage error} = \frac{\text{FEM results} - \text{mathematical model results}}{\text{FEM results}} \times 100 \quad (6.2)$$

BENDING 1 - 2-layers						
	RESONANCE FREQUENCY [kHz]				Percentage error [%] FEM- E*approx	Percentage error [%] FEM- E*Oberst
	Experimental results	FEM results	Mathematical model			
			E* approximate	E* Oberst		
Cantilever 1	N/A	83,498	52,388	51,411	37,26	38,43
Cantilever 2	N/A	62,455	40,053	39,306	35,87	37,07

Table 6.10 – Results in Bending 1 in 2-layers configuration

BENDING 1 - 3-layers						
	RESONANCE FREQUENCY [kHz]				Percentage error [%] FEM- E*approx	Percentage error [%] FEM- E*Oberst
	Experimental results	FEM results	Mathematical model			
			E* approximate	E* Oberst		
Cantilever 1	75.3	75.638	48,872	46,582	35,39	38,41
Cantilever 2	55.5	56.584	37,365	35,614	33,97	37,01

Table 6.11 – Results in Bending 1 in 3-layers configuration

BENDING 2 - 2-layers						
	RESONANCE FREQUENCY [kHz]				Percentage error [%] FEM- E*approx	Percentage error [%] FEM- E*Oberst
	Experimental results	FEM results	Mathematical model			
			E* approximate	E* Oberst		
Cantilever 1	N/A	1157	787,661	-	31,92	-
Cantilever 2	N/A	871,76	602,243	-	30,92	-

Table 6.12 – Results in Bending 2 in 2-layers configuration

BENDING 2 - 3-layers						
	RESONANCE FREQUENCY [kHz]				Percentage error [%] FEM- E*approx	Percentage error [%] FEM- E*Oberst
	Experimental results	FEM results	Mathematical model			
			E* approximate	E* Oberst		
Cantilever 1	N/A	1270,2	864,471	-	31,94	-
Cantilever 2	N/A	957,05	660,972	-	30,94	-

Table 6.13 – Results in Bending 2 in 3-layers configuration

The mathematical model have errors between 30% and 35% compared to FEM results. Therefore, the mathematical model does not ensure a good correspondence.

There is the necessity to re-define the mathematical model, searching possible errors that could solve the problem of the good correspondence between results.

7. THE LIMITS OF MATHEMATICAL MODEL

This chapter will re-analyze the mathematical model, searching for possible errors. In first step, mathematical model in case of a simple cantilever (with no T-shape) was compared to Euler-Bernoulli theory, verifying if they correspond in term of results.

7.1 Evidence with Euler – Bernoulli theory

Euler – Bernoulli (E-B) beam theory for a rectangular cross section was considered. Varying the parameter of T-shape beam (α , β and γ), it is possible to obtain a beam with a rectangular cross section, the same of Euler – Bernoulli beam theory. Comparing the two results in term of first natural frequency, it is possible to verify if mathematical model is correct, and eventually, could be determined possible errors.

There is necessity to define the Euler – Bernoulli beam theory.

- 7.1.1 Euler – Bernoulli beam theory

Euler – Bernoulli theory found its truth on two important assumption:

- The cross section of the beam do not deform in important manner if a transverse or axial load is applied;
- The cross section of the beam, during deformation, is assumed to remain normal and planar to the deformed axis of the beam.

In *figure 7.1* there is a generic beam of Euler – Bernoulli theory:

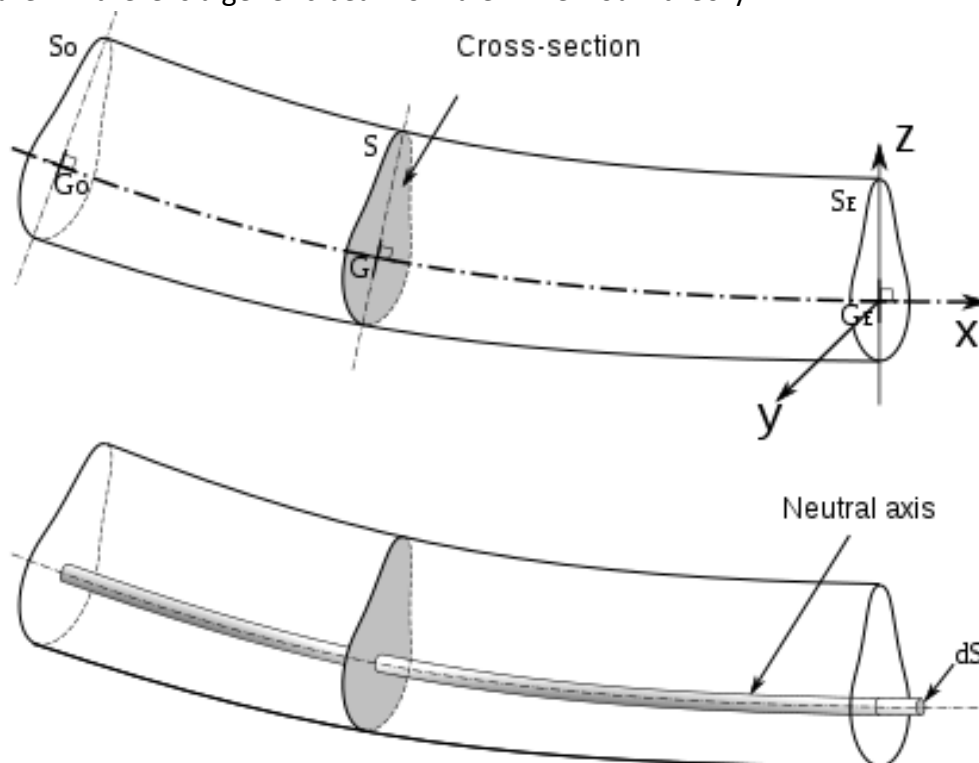


Figure 7.1 – Generic beam for Euler – Bernoulli theory (source: Wikipedia)

The equation of Euler – Bernoulli in dynamic case is:

$$\frac{\partial^2}{\partial x^2} \left(EI \frac{\partial^2 v}{\partial x^2} \right) = -\mu \frac{\partial^2 v}{\partial t^2} + q(x) \quad (7.1)$$

Where:

$v(x)$ = deflection of the beam in z-axis;

E = Young's modulus of material;

I = moment of inertia of section;

q = distributed load;

In case the beam is homogeneous, and E and I are independent from x , the beam equation of Euler – Bernoulli become:

$$\left(EI \frac{\partial^4 v}{\partial x^4} \right) = -\mu \frac{\partial^2 v}{\partial t^2} + q(x) \quad (7.2)$$

In this thesis, also if cantilevers are not homogenous, because made by composites material, the method that permits to determine an equivalent Young's modulus, make the system homogenous, as if it were made from a single equivalent material. Therefore, the equation (7.2) can be used.

The beam could have many configurations, like free-free, cantilever beam ecc. In this thesis, cantilever beam were analyzed. *Figure 7.2* shows the modes of vibrations of a cantilever beam.

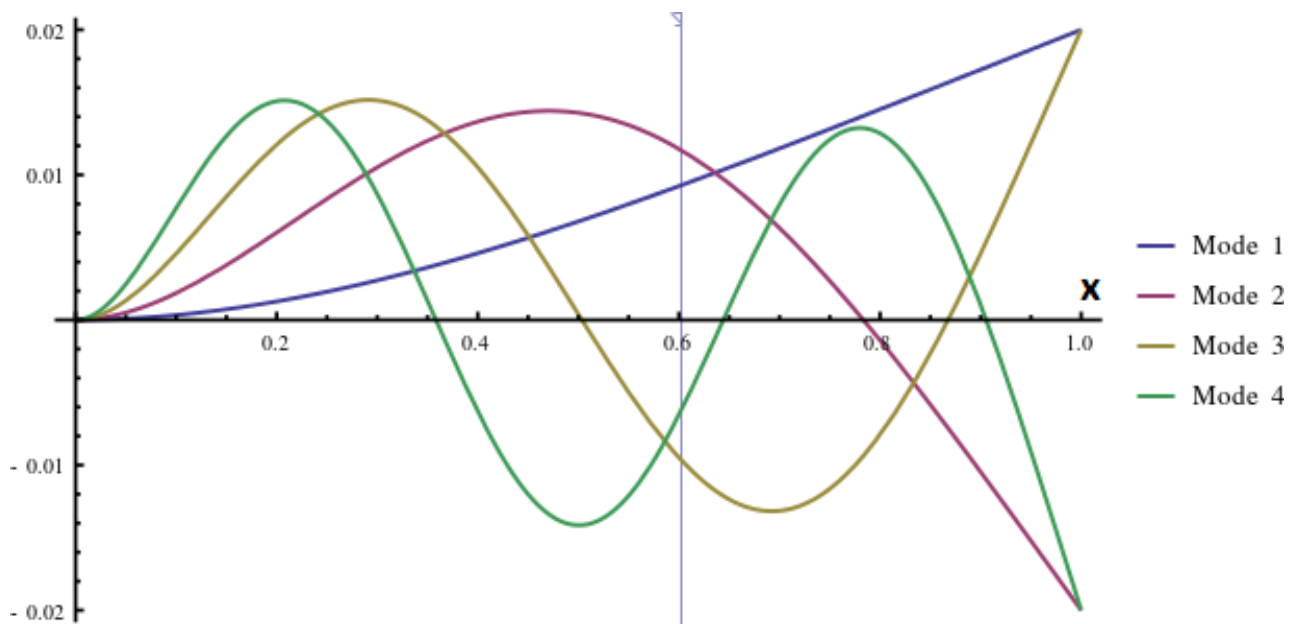


Figure 7.2 – Modes of resonance vibrations for a cantilever beam (source: Wikipedia)

To find the natural frequencies, there is necessity to define the boundary conditions to apply in equation (7.2):

$$v = 0, \quad \frac{dv}{dx} = 0 \quad \text{at } x = 0 \quad (7.3)$$

$$\frac{d^2v}{dx^2} = 0, \quad \frac{d^3v}{dx^3} = 0 \quad \text{at } x = L \quad (7.4)$$

Applying the boundary conditions (in equation 7.3 and 7.4) in Euler – Bernoulli equation, it is possible to determine non-trivial solutions solving numerically the nonlinear equation:

$$\cosh(\beta_n L) \cos(\beta_n L) + 1 = 0 \quad (7.5)$$

The first solution of equation (7.5), which represents the configuration of first natural frequency:

$$\frac{\beta_1 L}{\pi} = 0.59686 \quad (7.6)$$

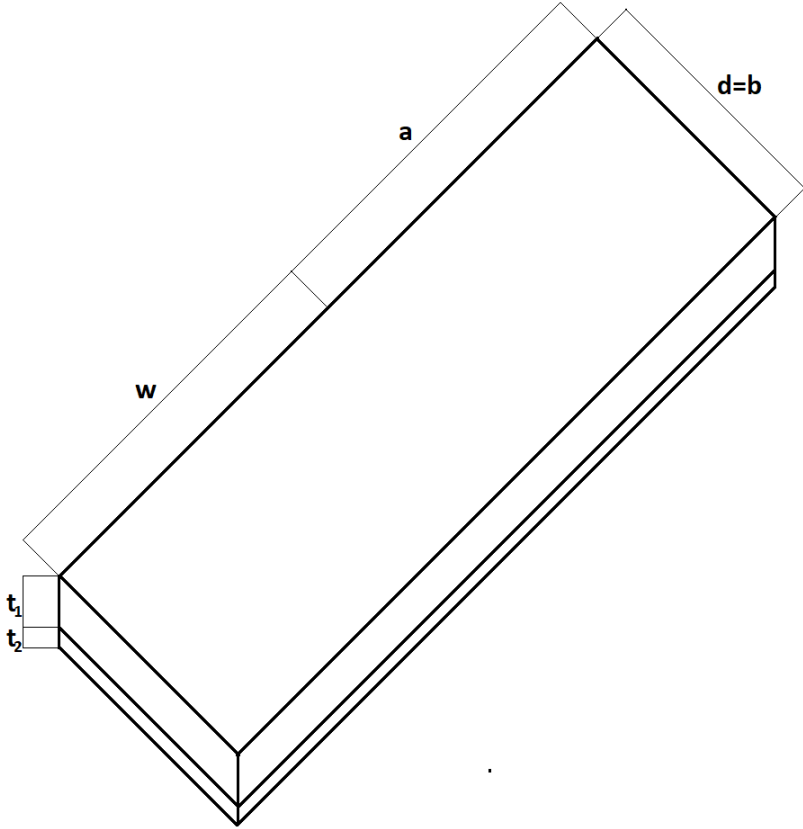
Therefore, the first natural frequency for a cantilever beam could be determined by formula:

$$\omega_1 = \beta_1^2 \sqrt{\frac{EI}{\mu}} \quad (7.7)$$

- **7.1.2 Correspondence between mathematical model, FEM and Euler – Bernoulli beam theory**

To make this comparison, just the Cantilever 1 was used in case of Bending 1.

Assuming the parameters $\beta=1$ and $\gamma=1$ the Cantilever 1 become a generic beam with a rectangular and constant cross sectional area. Furthermore, the beam was considered in a 2-layers configuration, where both layers are made by the same material (GaN). This new beam will be called “Cantilever 1.1” (in figure 7.3 with its geometrical data):



$$E = E_{GaN}$$

$$\beta = 1 \rightarrow a = w = 90\mu m$$

$$\gamma = 1 \rightarrow b = d = 30\mu m$$

$$t_1 = 1.5\mu m \quad t_2 = 0.5\mu m$$

$$t_1 + t_2 = t = 2\mu m$$

Figure 7.3 – Cantilever 1.1 with its geometrical parameters

The formula of mathematical model to calculate the first natural frequency (in equation 5.39) was:

$$\omega_{1f-Bending1} = \frac{\alpha\beta}{2a} \sqrt{\frac{(E^*/\rho^*)}{\beta^2 + \frac{1}{\beta^2} + \beta(\gamma + 3) + \frac{1}{\beta}(3\gamma + \frac{1}{\gamma}) + 3\gamma + 3}} \quad (5.39)$$

Substituting in this equation the parameters $\beta=1$ and $\gamma=1$, and substituting to parameter α the value $\alpha=t/a$, the formula in (7.10) was obtained:

$$\omega_{1f-Cantilever\ 1.1} = \frac{1}{8} \frac{t}{a^2} \sqrt{\frac{E}{\rho}} \quad (7.8)$$

The results is 26,649 kHz.

Modeling Cantilever 1.1 in Solidworks, and making dynamical analysis, the value of the first resonance frequency is 54,909 kHz. The result is showed in figure 7.4.

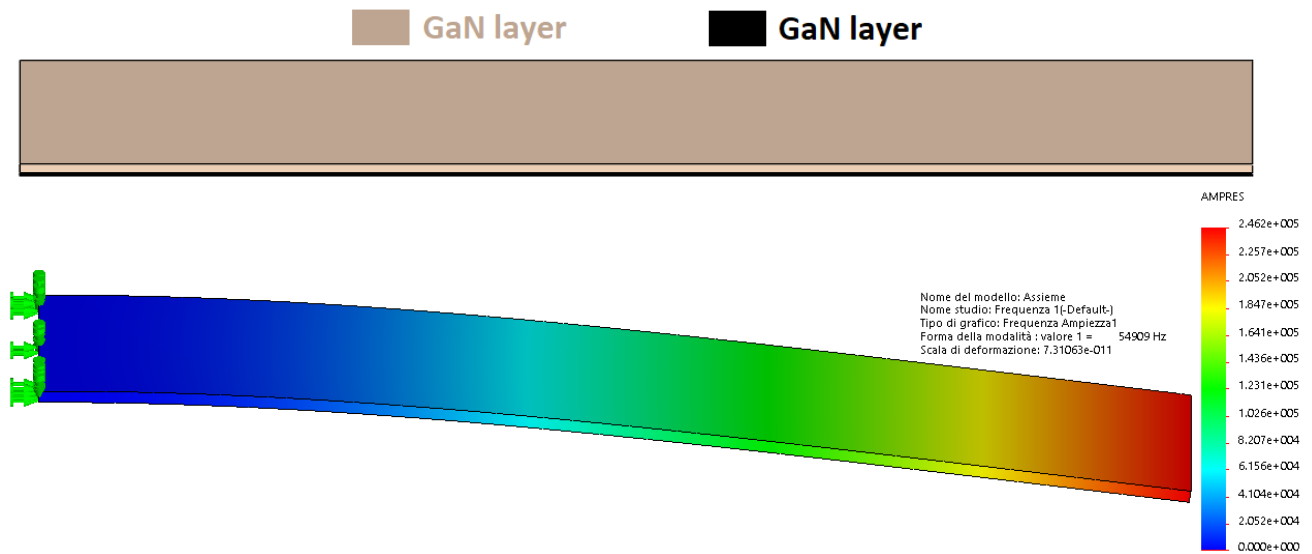


Figure 7.4 – Cantilever 1.1 in 2-layers made by the same material

Applying the final formula (7.7) of Euler-Bernoulli beam theory for a cantilever:

$$\omega_{1f-Cantilever\ 1.1\ E-B} = \beta_1^2 \sqrt{\frac{EI}{\mu}} \quad (7.9)$$

Where:

$$\frac{\beta_1 2a}{\pi} = 0.59686 \rightarrow \beta_1 = \frac{0.59686 * \pi}{2a} = \frac{Z}{2a} \quad (7.10);$$

$$I = \frac{dt^3}{12} \quad (7.11);$$

$$\mu 2a = \rho 2a t d \rightarrow \mu = \rho t d \quad (7.12);$$

$$Z = 0.59686 * \pi = 1.8751$$

Substituting the equations (7.10), (7.11) and (7.12), equation (7.9) becomes:

$$\omega_{1f-Cantilever\ 1.1\ E-B} = \frac{Z^2}{8\sqrt{3}} \frac{t}{a^2} \sqrt{\frac{E}{\rho}} \quad (7.13)$$

The result of equation (7.13) is 54,096 kHz.

Comparing the two equations, (7.8 – Obtained by mathematical model) and (7.13 – Obtained by Euler – Bernoulli beam theory), it is possible to notice that the last part of equations are the same. Theoretically, they must be equal, but:

$$1 \neq \frac{Z^2}{\sqrt{3}} \quad (7.14)$$

Table 7.5 lists the results obtained by mathematical model, FEM and Euler – Bernoulli beam theory on Cantilever 1.1:

CANTILEVER 1.1			
	Mathematical model	FEM	Euler – Bernoulli beam theory
First Resonance Frequency	26,649 kHz	54,909 kHz	54,096 kHz

Table 7.5 – Results on Cantilever 1.1 in mathematical model, FEM and Euler – Bernoulli beam theory

As expected, the results of FEM and Euler-Bernoulli are congruent. However, the mathematical model differs much from these result, as confirmed by (7.16).

The initial formula to calculate the resonance frequency in mathematical model, showed in equation 5.6 is:

$$\omega_n = \sqrt{\frac{k}{m}} \quad (5.6)$$

The stiffness “k” of this formula was calculated from Castigliano’s Method, which of course is not arguable. The possible error could be given by the mass. In fact, in its calculation, the whole mass of the micro cantilever beam was considered. The equation (5.6) come from a mass-spring system in figure 7.5:

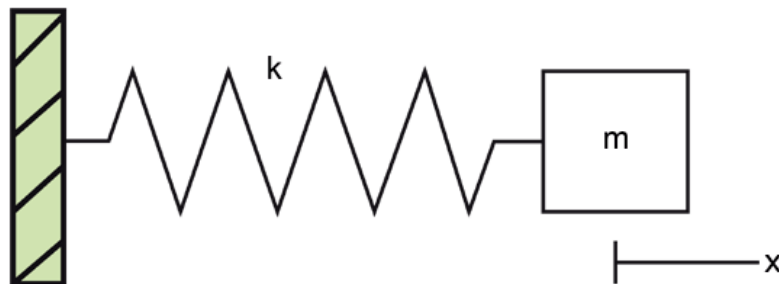


Figure 7.5 – Mass-Spring system

Into mass-spring system, the mass is considered concentrated in one single point in the end of the beam, while the mass of spring is considered negligible.

The micro cantilevers has the mass distributed along the beam, therefore an equivalent mass (to be however applied in the end of cantilever) could be calculated to simulate the distributed mass of the micro cantilever.

- **7.1.3 Calculation of equivalent mass of “Cantilever 1.1”**

The figure 7.6 show a scheme of Cantilever 1.1:

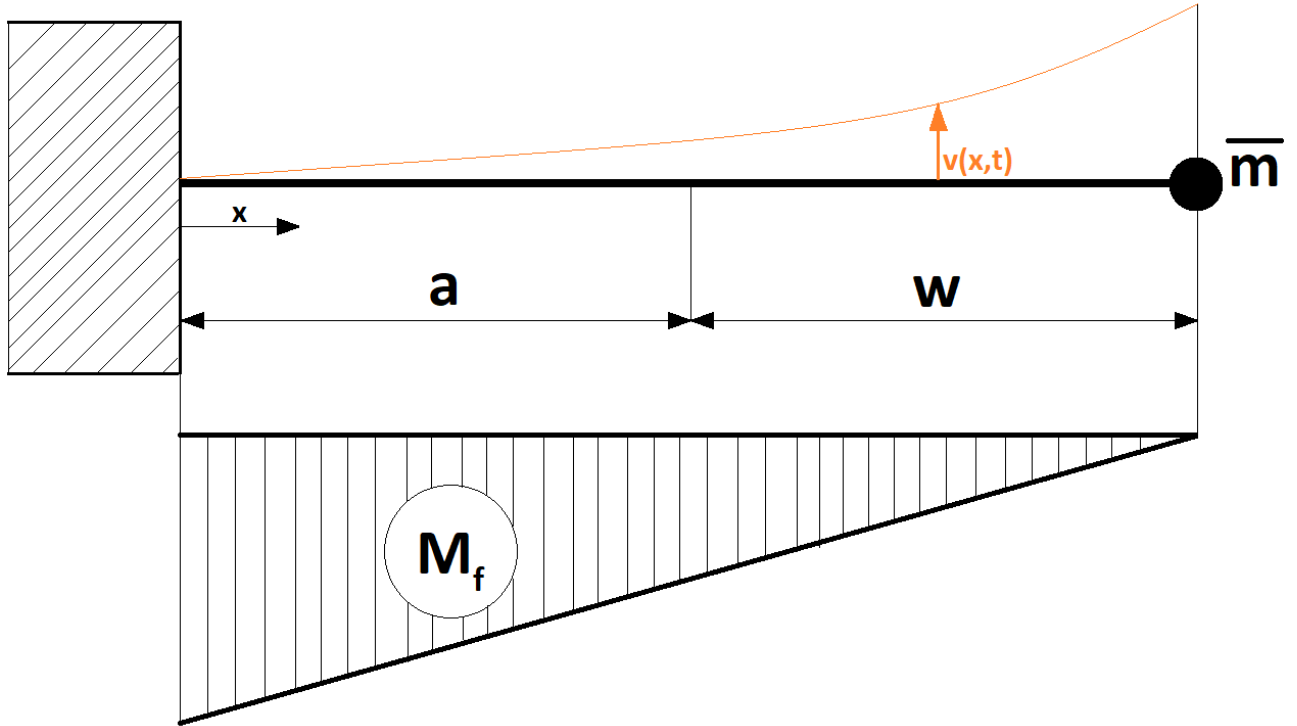


Figure 7.6 – Scheme of Cantilever 1.1 with equivalent mass concentrated in the end, with trend of bending moment

The mass along the length $L = a + w$ is negligible (as in case of mass-spring system, where the mass of spring is negligible). In the end of the cantilever there is applied an equivalent mass " \bar{m} ", which approximates the distributed mass of the real cantilever.

To calculate the equivalent mass it is possible to match the kinetic energy of the cantilever with distributed mass with kinetic energy with concentrated mass.

The kinetic energy of distributed mass:

$$T_{distributed} = \int_0^L \frac{1}{2} \mu \dot{v}^2(x, t) dx \quad (7.15)$$

Where:

$\dot{v}(x, t)$ = speed of deformation of the beam;

μ = mass per unit of length;

The speed of deformation of the beam is defined as:

$$v(x, t) = v_0 \sin(\omega t) \cdot \phi(x) \quad (7.16)$$

$$\dot{v}(x, t) = v_0 \omega \cos(\omega t) \cdot \phi(x) \quad (7.17)$$

Where:

$\Phi(x)$ = deformation of cantilever;

Substituting the equation (7.17) in (7.15):

$$\begin{aligned} T_{distributed} &= \int_0^L \frac{1}{2} \mu v_0^2 \omega^2 \cos^2(\omega t) \phi^2(x) dx \\ &= \frac{1}{2} \mu v_0^2 \omega^2 \cos^2(\omega t) \int_0^L \phi^2(x) dx \quad (7.18) \end{aligned}$$

The kinetic energy of concentrated mass:

$$T_{concentrated} = \frac{1}{2} \bar{m} \dot{v}^2(L) = \frac{1}{2} \bar{m} v_0^2 \omega^2 \cos^2(\omega t) \cdot \phi^2(L) \quad (7.19)$$

To determine the function of deformation of cantilever, the bending moment " M_f " was defined:

$$M_f = EI \frac{\partial^2 \phi}{\partial x^2} = EI \phi''(x) \quad (7.20)$$

Assuming that the graph of bending moment is linear, the deformation of cantilever is:

$$\phi''(x) = 1 - \frac{x}{L} \quad (7.21)$$

Equation (7.21) represents the trend of the graph of bending moment showed in *figure 7.6*. Integrating the equation (7.21) twice:

$$\phi'(x) = x - \frac{x^2}{L} + C_1 \quad (7.22)$$

$$\phi(x) = \frac{x^2}{2} - \frac{x^3}{6L} + C_2 \quad (7.23)$$

To determine the two constant value " C_1 " and " C_2 ", boundary conditions were applied:

$$\phi'(0) = 0 \rightarrow C_1 = 0$$

$$\phi(0) = 0 \rightarrow C_2 = 0$$

Finally the deformation of cantilever is:

$$\phi(x) = \frac{x^2}{2} - \frac{x^3}{6L} \quad (7.24)$$

Matching the kinetic energy of distributed mass with kinetic energy of concentrated mass, and substituting the value of “ $\Phi(x)$ ” of equation (7.24):

$$\begin{aligned} T_{distributed} &= T_{concentrated} \\ \frac{1}{2} \mu v_0^2 \omega^2 \cos^2(\omega t) \int_0^L \phi^2(x) dx &= \frac{1}{2} \bar{m} v_0^2 \omega^2 \cos^2(\omega t) \cdot \phi^2(L) \\ \mu \int_0^L \phi^2(x) dx &= \bar{m} \phi^2(L) \\ \mu \int_0^L \left(\frac{x^2}{2} - \frac{x^3}{6L} \right)^2 dx &= \bar{m} \frac{L^4}{9} \\ \mu \left[\frac{L^5}{20} + \frac{L^5}{252} - \frac{L^5}{36} \right] &= \bar{m} \frac{L^4}{9} \quad (7.25) \end{aligned}$$

Isolating the equivalent mass “ \bar{m} ” in equation (7.25):

$$\bar{m} = \frac{33}{140} \mu L \quad (7.26)$$

Where:

$$\mu L = m_{cantilever\ 1.1} = \rho L t d \rightarrow \mu = \rho t d \quad (7.27)$$

$$a = w \rightarrow L = a + w \rightarrow L = 2a \quad (7.28)$$

The final equation, substituting before the equation (7.28) in (7.27) and later (7.27) in (7.26), become:

$$\bar{m} = \frac{33}{70} \rho t d a \quad (7.29)$$

- 7.1.4 New mathematical model in “Cantilever 1.1” and comparison with FEM results

To define the new mathematical model on Cantilever 1.1, it is necessary to define the stiffness “ $k_{1.1}$ ”. Equation (5.6) then gives the first natural frequency.

The stiffness “ $k_{1.1}$ ” of the Cantilever 1.1 is based on section 5.2.1. The result of stiffness so far obtained is:

$$k = \frac{3E^* I_1 I_2}{I_2 w^3 + I_1 a^3 + 3I_1 a^2 w + 3I_1 a w^2} \quad (5.26)$$

In case of Cantilever 1.1, $a=w$, and $I_1 = I_2 = I$ because of the cross sectional area do not change along x-axis. Therefore, the stiffness of Cantilever 1.1 becomes:

$$k_{1.1} = \frac{3EI^2}{Ia^3 + Ia^3 + 3Ia^3 + 3Ia^3} = \frac{3EI}{8a^3} \quad (7.30)$$

The first natural frequency is:

$$\omega_{1f-Cantilever\ 1.1} = \sqrt{\frac{k_{1.1}}{m}} = \sqrt{\frac{3E}{8a^3} \frac{dt^3}{12} \frac{70}{33\rho t da}} = \sqrt{\frac{35}{528} \frac{t}{a^2}} \sqrt{\frac{E}{\rho}} \quad (7.31)$$

The result of this equation is 54,889 kHz.

Table 7.7 reports the comparison between NEW mathematical model, FEM and Euler – Bernoulli beam theory.

CANTILEVER 1.1			
	NEW Mathematical model	FEM	Euler – Bernoulli beam theory
First Resonance Frequency	54,889 kHz	54,909 kHz	54,096 kHz

Table 7.7 – Comparison between NEW mathematical model, FEM and Euler – Bernoulli beam theory

As shown in table 7.7, the NEW mathematical model give congruent results when compared to FEM or Euler – Bernoulli beam theory.

The last check to make is to consider a change on Cantilever 1.1. The same geometric dimensions were kept, but a sandwich made by two layers of different material was considered. For simplicity GaN + Silicon were considered. In figure 7.8 there is the result obtained by FEM. This example will be called “Cantilever 1.2”

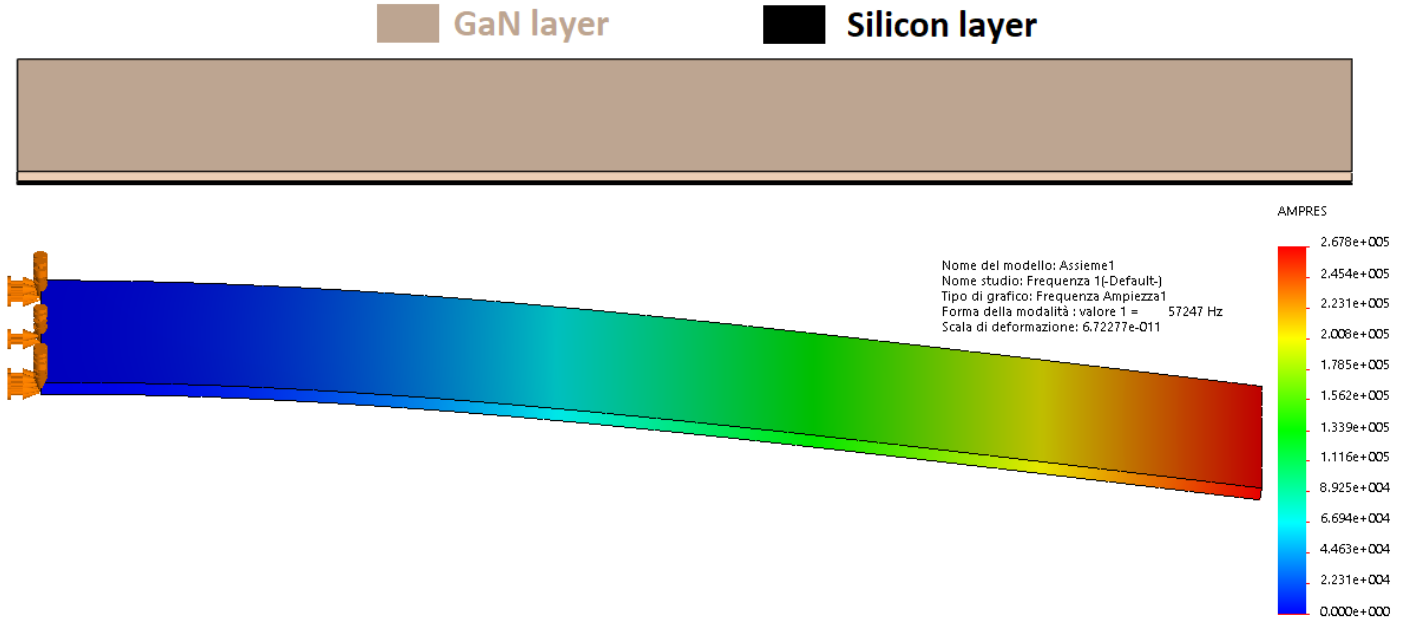


Figure 7.8 – Cantilever 1.2 in two layer made by GaN + Silicon

In this case, in equations of stiffness “ $k_{1.2}$ ” and equivalent mass “ \overline{m} ”, it is just necessary to introduce the parameter of equivalent density “ ρ^* ” and equivalent Young’s modulus “ E^* ”. About thickness, the cantilever is the same of figure 7.3, where:

$$t_1 = t_{GaN} = 1.5\mu m \quad t_2 = t_{Sil} = 0.5\mu m$$

$$t = t_{GaN} + t_{Sil} = 2\mu m$$

Finally, the equation (7.32) becomes:

$$\omega_{1f-Cantilever\ 1.2} = \sqrt{\frac{k_{1.2}}{\overline{m}}} = \sqrt{\frac{3E^* dt^3}{8a^3} \frac{70}{12} \frac{1}{33\rho^* t da}} = \sqrt{\frac{35}{528} \frac{t}{a^2} \frac{E^*}{\rho^*}} \quad (7.32)$$

As regards equivalent density, it is possible to use the equation:

$$\rho^* = \frac{\rho_{GaN} t_{GaN} + \rho_{Sil} t_{Sil}}{t} \quad (7.33)$$

As regards equivalent Young’s modulus, it is possible to use both method of “Approximate Young’s modulus” (in paragraph 5.4.1) and “Oberst’s equivalent Young’s modulus” (in paragraph 5.4.2.1). The two equations are:

$$E_{approximate}^* = \frac{E_{GaN} t_{GaN} + E_{Sil} t_{Sil}}{(t_{GaN} + t_{Sil})} \quad (7.34)$$

$$E_{Oberst}^* = p_{GaN}^3 E_{GaN} (A + eB) \quad (7.35)$$

Where:

$$A = \frac{(1 - h^2 e) + [1 + (2h + h^2)e]^3}{2(1 + he)^3}$$

$$B = \frac{(1 + 2h - h^2 e)^3 - (1 - h^2 e)^3}{2(1 + he)^3}$$

With:

$$h = t_{sil} / t_{GaN};$$

$$e = E_{sil} / E_{GaN};$$

$$I_1 = dt_{GaN}^3 / 12;$$

$$p_{GaN} = t_{GaN} / t$$

In *table 7.9*, the comparison of results of NEW mathematical model with FEM and Euler – Bernoulli beam theory is presented:

CANTILEVER 1.2					
	NEW Mathematical model		FEM	Euler – Bernoulli beam theory	
	E* approximate	E* Oberst		E* approximate	E* Oberst
First Resonance Frequency	58,429 kHz	57,340 kHz	57,247 kHz	57,584 kHz	56,511 kHz
Percentage Error with respect to FEM	2,06%	0,16%	-	0,58%	1,29%

Table 7.9 – Results in term of first resonance frequency on Cantilever 1.2

Also in this case, the results give an important response. In fact, the mathematical model not only is similar to the FEM, but confirms also that the Oberst's equation to calculate the equivalent Young's modulus is more precise than approximate method. In fact, the accuracy of the calculation respect to FEM pass from a percentage error of 2,06% to 0,16%.

7.2 Calculation of the Equivalent mass in T-shape cantilever

The same procedure has been applied to determine the equivalent mass of the T-shape cantilever. The scheme of Cantilever with its bending moment is showed in *figure 7.10*:

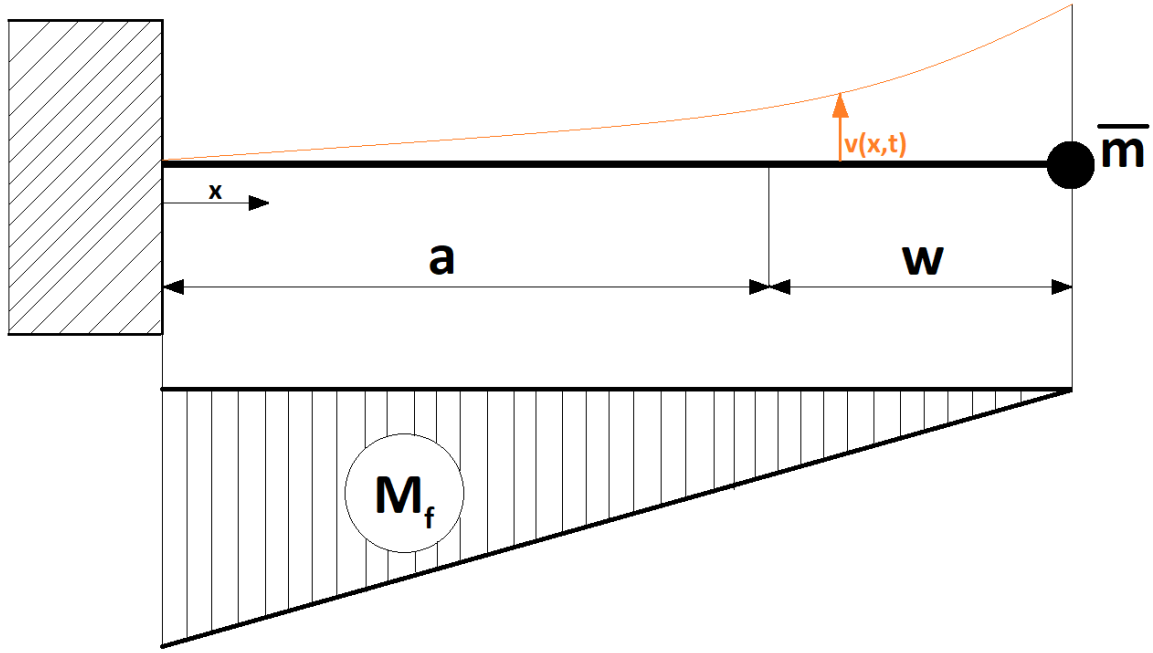


Figure 7.10 – Scheme of cantilever in T-shape with equivalent mass concentrated in the end, with trend of bending moment

The kinetic energy of distributed mass is:

$$T_{distributed} = \int_0^a \frac{1}{2} \mu_1 \dot{v}^2(x, t) dx + \int_a^{a+w} \frac{1}{2} \mu_2 \dot{v}^2(x, t) dx \quad (7.36)$$

Where:

$v(x, t)$ = speed of deformation of the beam;

$$\mu_1 a = \rho a t d \rightarrow \mu_1 = \rho t d \quad (7.37)$$

$$\mu_2 w = \rho w t b \rightarrow \mu_2 = \rho t b \quad (7.38)$$

The deformation of the beam could be defined as in equation (7.16) and in (7.17). Substituting these equations in (7.36):

$$\begin{aligned} T_{distributed} &= \int_0^a \frac{1}{2} \mu_1 v_0^2 \omega^2 \cos^2(\omega t) \phi^2(x) dx + \int_a^{a+w} \frac{1}{2} \mu_2 v_0^2 \omega^2 \cos^2(\omega t) \phi^2(x) dx \\ &= \frac{1}{2} v_0^2 \omega^2 \cos^2(\omega t) \left[\int_0^L \mu_1 \phi^2(x) dx + \int_a^{a+w} \mu_2 \phi^2(x) dx \right] \quad (7.39) \end{aligned}$$

The same function calculated from bending moment, in the case of Cantilever 1.1 analysed in paragraph [7.1.3] was used. Therefore, the results are in equation (7.24). Substituting it and equations of mass per unit of length (7.37 and 7.38) in equation (7.39), and solving the integrals:

$$\begin{aligned}
T_{distributed} &= \frac{1}{2} v_0^2 \omega^2 \cos^2(\omega t) \left[\mu_1 \int_0^a \phi^2(x) dx + \mu_2 \int_a^w \phi^2(x) dx \right]; \\
&= \frac{1}{2} v_0^2 \omega^2 \cos^2(\omega t) \left[\mu_1 \int_0^a \left(\frac{x^2}{2} - \frac{x^3}{6L} \right)^2 dx + \mu_2 \int_a^w \left(\frac{x^2}{2} - \frac{x^3}{6L} \right)^2 dx \right]; \\
&= \frac{1}{2} v_0^2 \omega^2 \cos^2(\omega t) \left\{ \mu_1 \left[\frac{a^5}{20} + \frac{a^7}{252(a+w)^2} - \frac{a^6}{36(a+w)} \right] \right. \\
&\quad + \mu_2 \left[\frac{(a+w)^2}{20} + \frac{(a+w)^7}{252(a+w)^2} - \frac{(a+w)^6}{36(a+w)} - \frac{a^5}{20} - \frac{a^7}{252(a+w)^2} \right. \\
&\quad \left. \left. + \frac{a^6}{36(a+w)} \right] \right\}; \\
&= \frac{1}{2} v_0^2 \omega^2 \cos^2(\omega t) \left\{ \rho t d \left[\frac{a^5}{20} + \frac{a^7}{252(a+w)^2} - \frac{a^6}{36(a+w)} \right] \right. \\
&\quad + \rho t b \left[\frac{(a+w)^2}{20} + \frac{(a+w)^5}{252} - \frac{(a+w)^6}{36} - \frac{a^5}{20} - \frac{a^7}{252(a+w)^2} \right. \\
&\quad \left. \left. + \frac{a^6}{36(a+w)} \right] \right\}; \\
&= \frac{1}{2} v_0^2 \omega^2 \cos^2(\omega t) \left\{ \rho t \left[\left(\frac{a^5}{20} + \frac{a^7}{252(a+w)^2} - \frac{a^6}{36(a+w)} \right) (d-b) \right. \right. \\
&\quad \left. \left. + \frac{11}{420} b(a+w)^5 \right] \right\}; \quad (7.40)
\end{aligned}$$

The kinetic energy of the concentrated mass is:

$$\begin{aligned}
T_{concentrated} &= \frac{1}{2} \bar{m} \dot{v}^2(L) = \frac{1}{2} \bar{m} v_0^2 \omega^2 \cos^2(\omega t) \cdot \phi^2(L) \\
&= \frac{1}{2} \bar{m} v_0^2 \omega^2 \cos^2(\omega t) \cdot \left[\frac{(a+w)^4}{9} \right] \quad (7.41)
\end{aligned}$$

Equating “ $T_{distributed}$ ” in equation (7.40) with “ $T_{concentrated}$ ” in (7.41), and isolating the “ \bar{m} ”:

$$T_{distributed} = T_{concentrated}$$

$$\begin{aligned}
\frac{1}{2} v_0^2 \omega^2 \cos^2(\omega t) \left\{ \rho t \left[\left(\frac{a^5}{20} + \frac{a^7}{252(a+w)^2} - \frac{a^6}{36(a+w)} \right) (d-b) \right. \right. \\
\left. \left. + \frac{11}{420} b(a+w)^5 \right] \right\} &= \frac{1}{2} \bar{m} v_0^2 \omega^2 \cos^2(\omega t) \cdot \left[\frac{(a+w)^4}{9} \right]
\end{aligned}$$

$$\bar{m} = \frac{9\rho t}{(a+w)^4} \left[\left(\frac{a^5}{20} + \frac{a^7}{252(a+w)^2} - \frac{a^6}{36(a+w)} \right) (d-b) + \frac{11}{420} b(a+w)^5 \right] \quad (7.42)$$

7.3 NEW mathematical model in T-shape cantilever

Once the equation that define the equivalent mass of micro cantilever in T-shape was found, a NEW mathematical model to calculate the first natural frequency was defined. Obviously, this NEW mathematical model will be valid on both Cantilever 1 and Cantilever 2, and generally in each T-shape cantilever. In equation will appear the value of equivalent Young's modulus "E*" and the value of equivalent density "p*". As regards these values, it is possible to use all method treated in chapter 5, for example the approximate method or Oberst's equation to calculate the equivalent Young's modulus.

The NEW mathematical model rises as in precedent case from the equation (5.6):

$$\omega_{1f} = \sqrt{\frac{k}{\bar{m}}} \quad (5.6)$$

The NEW mathematical model will be applied on Bending 1 and on Bending 2. In both cases, the equivalent mass do not change, and its value was represented in equation (7.44). Just the parameter of stiffness "k" is different, because it depends from different moments of inertia. As regards Bending 1, the value of stiffness "k_{Bending1}" is the same calculated in paragraph [5.2.1], in equation (5.31):

$$k_{Bending1} = \frac{E^*/4 bdt^3}{dw^3 + ba^3 + 3ba^2w + 3baw^2} \quad (5.31)$$

As regards Bending 2, the value of stiffness "k_{Bending2}" is the same calculated in paragraph [5.2.2] in equation [5.37]:

$$k_{Bending2} = \frac{E^*/4 b^3d^3t}{d^3w^3 + b^3a^3 + 3b^3a^2w + 3b^3aw^2} \quad (5.37)$$

In next chapter, the mathematical model will be tested (comparing it with FEM and experimental results) in all combinations of Cantilever 1 and Cantilever 2 as follow:

- Bending 1 in 2-layers with approximate method and Oberst's equation to calculate equivalent Young's modulus;
- Bending 1 in 3-layers with approximate method and Oberst's equation to calculate equivalent Young's modulus;
- Bending 2 in 2-layers with approximate method to calculate equivalent Young's modulus;
- Bending 2 in 3-layers with approximate method to calculate equivalent Young's modulus.

8. COMPARISON OF RESULTS OF NEW MATHEMATICAL MODEL, FEM AND EXPERIMENTAL TESTS

Table 8.1, 8.2, 8.3 and 8.4 list the results in term of first natural frequency in Bending 1 and Bending 2, comparing experimental results, FEM results and NEW mathematical model results. There are also percentage error calculated as in paragraph [6.2] in equation (6.2).

BENDING 1 - 2-layers						
	RESONANCE FREQUENCY [kHz]				Percentage error [%] FEM- E*approx	Percentage error [%] FEM- E*Oberst
	Experimental results	FEM results	NEW Mathematical model			
			E* approximate	E* Oberst		
Cantilever 1	N/A	83,498	84,760	83,180	1,51	0,38
Cantilever 2	N/A	62,455	63,540	62,356	1,74	0,16

Table 8.1 – Results in Bending 1 in 2-layers configuration

BENDING 1 - 3-layers						
	RESONANCE FREQUENCY [kHz]				Percentage error [%] FEM- E*approx	Percentage error [%] FEM- E*Oberst
	Experimental results	FEM results	NEW Mathematical model			
			E* approximate	E* Oberst		
Cantilever 1	75,3	75,638	79,071	75,367	4,54	0,36
Cantilever 2	55,5	56,584	59,276	56,499	4,75	0,15

Table 8.2 – Results in Bending 1 in 3-layers configuration

BENDING 2 - 2-layers						
	RESONANCE FREQUENCY [kHz]				Percentage error [%] FEM- E*approx	Percentage error [%] FEM- E*Oberst
	Experimental results	FEM results	NEW Mathematical model			
			E* approximate	E* Oberst		
Cantilever 1	N/A	1157	1274,4	-	10,15	-
Cantilever 2	N/A	871,76	955,404	-	9,59	-

Table 8.3 – Results in Bending 2 in 2-layers configuration

BENDING 2 - 3-layers

	RESONANCE FREQUENCY [kHz]				Percentage error [%] FEM- E*approx	Percentage error [%] FEM- E*Oberst
	Experimental results	FEM results	NEW Mathematical model			
			E* approximate	E* Oberst		
Cantilever 1	N/A	1270,2	1398,7	-	10,12	-
Cantilever 2	N/A	957,05	1048,6	-	9,57	-

Table 8.4 – Results in Bending 2 in 3-layers configuration

Table 8.5 and 8.6 summarize the calculation of NEW mathematical model in 2-layers and 3-layers configurations:

2-LAYERS MODEL

BENDING 1

BENDING 2

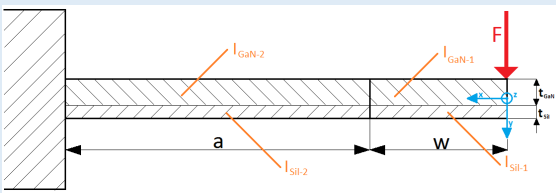
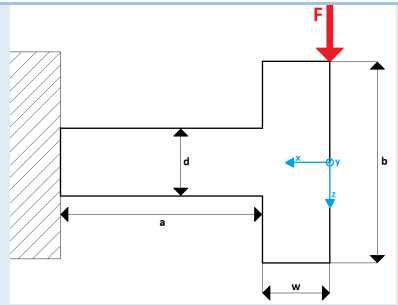
Figure		
Stiffness k [N/m]	$k = \frac{E^*/4 b a^3 \beta^3}{1 + \gamma \beta^3 + 3 \gamma \beta^2 + 3 \gamma \beta}$	$k = \frac{E^*/4 b^3 a^3 \beta^3}{t^2 (1 + \beta^3 \gamma^3 + 3 \beta^2 \gamma^3 + 3 \beta \gamma^3)}$
Equivalent Young's modulus with approximate method	$E_{approx} = \frac{E_{GaN} t_{GaN} + E_{Si} t_{Si}}{(t_{GaN} + t_{Si})}$	
Equivalent Young's modulus with Oberst's equation	$E_{Oberst} = p_{GaN}^3 E_{GaN} (A + eB)$	-
Equivalent density ρ^* [kg/m ³]	$\rho^* = \rho_{GaN} p_{GaN} + \rho_{Si} p_{Si}$	
Equivalent mass [kg]	$\bar{m} = \frac{9 \rho^* t}{(a + w)^4} \left[\left(\frac{a^5}{20} + \frac{a^7}{252(a + w)^2} - \frac{a^6}{36(a + w)} \right) (d - b) + \frac{11}{420} b (a + w)^5 \right]$	
First Natural Frequency ω_{1f} [rad/s]	$\omega_{1f-Bending1} = \sqrt{\frac{k}{\bar{m}}}$	$\omega_{1f-Bending2} = \sqrt{\frac{k}{\bar{m}}}$

Table 8.5 – Scheme of calculation of NEW mathematical mode in 2-layers

3-LAYERS MODEL

BENDING 1

BENDING 2

Figure		
Stiffness k [N/m]	$k = \frac{E^*/4 b \alpha^3 \beta^3}{1 + \gamma \beta^3 + 3\gamma \beta^2 + 3\gamma \beta}$	$k = \frac{E^*/4 b^3 \alpha^3 \beta^3}{t^2(1 + \beta^3 \gamma^3 + 3\beta^2 \gamma^3 + 3\beta \gamma^3)}$
Equivalent Young's modulus with approximate method	$E_{approx} = \frac{E_{GaN} t_{GaN} + E_{AlN} t_{AlN} + E_{Si} t_{Si}}{(t_{GaN} + t_{AlN} + t_{Si})}$	
Equivalent Young's modulus with Oberst's equation	$E_{Oberst} = p_{GaN}^3 E_{GaN} (A_1 + e_2 B_1 + e_3 C_1)$	-
Equivalent density ρ^* [kg/m ³]	$\rho^* = \rho_{GaN} p_{GaN} + \rho_{AlN} p_{AlN} + \rho_{Si} p_{Si}$	
Equivalent mass [kg]	$\bar{m} = \frac{9\rho^* t}{(a+w)^4} \left[\left(\frac{a^5}{20} + \frac{a^7}{252(a+w)^2} - \frac{a^6}{36(a+w)} \right) (d-b) + \frac{11}{420} b(a+w)^5 \right]$	
First Natural Frequency ω_{1f} [rad/s]	$\omega_{1f-Bending1} = \sqrt{\frac{k}{\bar{m}}}$	$\omega_{1f-Bending2} = \sqrt{\frac{k}{\bar{m}}}$

Table 8.6 – Scheme of calculation of NEW mathematical model in 3-layers

9. CONCLUSIONS

The goal of the thesis was to determine a mathematical model that could calculate the first natural frequency without using LDV or FEM. The precision of the results obtained, can be considered very satisfactory. Thanks to the mathematical model it is possible to calculate in quick way the first natural frequency.

In Bristol University laboratories, the 2-layers configuration was not produced, however, it is evident to notice that the 2-layers configurations presents higher value of first natural frequency due to increase of mass of AlN in 3-layers case. AlN was added to decrease defects density of GaN, because the two materials presents the same crystalline structure.

The layers of Silicon originally were not considered, but the fabrication method of the T-shape cantilever in chapter 3, leaves a thin layer of Silicon due to imperfection in etching process.

The results obtained by FEM are very coherent with results of experimental model. Therefore, due the absence of experimental results on 2-layers configurations, the results of mathematical model were compared to FEM results.

Before a mathematical model was produced, some hypotheses were made. For example, the 2 or 3 layers of the cantilevers are perfectly bounded and overlapped, and the separation line between layers results always defined without imperfection. Due to fabrication method, the separation line could not be without imperfection. That generates the differences in results between LDV measures and FEM.

The first mathematical model considers the whole mass of cantilever applied in the end of it.

These certainly does not correspond to reality, because mass is distributed along the beam.

Therefore, a calculation of an equivalent mass, to be integrated in a NEW mathematical model, was required to increase the accuracy in calculations.

The percentage errors of the NEW mathematical model result lower than first mathematical model that considers the whole mass of the beam. In fact, as the tables 8.1, 8.2, 8.3 and 8.4 show, the percentage errors in 2-layers and 3-layers are respectively 0,38% in Cantilever 1 and 0,16% in Cantilever 2 in both case of Bending 1.

As regards Bending 2, the percentage errors are higher than Bending 1 due to higher value of first natural frequency than Bending 1. In fact, the Bending 2 of the micro cantilevers result as an unnatural bending that rarely could occurred, and do not respect

Another important result is realized in calculations of E^* in approximate method and Oberst's method. The Oberst's equation give results visibly more precise than approximate method.

Unfortunately, this occurs only in Bending 1, while in Bending 2 the Oberst's method could not be applied because the load that bends the beam is parallel with separation line between layers.

The future prospects of this study could be the possibility to integrate in mathematical model that the micro cantilever could be inserted in a liquid environment that produces a superficial pressure on the cantilevers. Therefore, it is possible to calculate how the first natural frequency varies if the cantilevers are immersed in a liquid. This future study is required because these T-shape cantilevers are produced for Bio-MEMS applications, also because GaN is very resistant in harsh environment. Another possibility for the future could be a change in micro cantilever design, to reach a certain first natural frequency, for example in application such as micro-antenna to send signals. The mathematical model represents a support for these future prospects, because it is applicable very quickly in any T-shape cantilever in single-layer or multi-layers configurations.

REFERENCES

[ref. 1.1] - R. Ghodssi; P. Lin (2011). MEMS Materials and Processes Handbook. Berlin: Springer. ISBN 978-0-387-47316-1

[ref. 2.1] - Piezoelectric GaN Sensor Structures - IEEE ELECTRON DEVICE LETTERS, VOL. 27, NO. 5, MAY 2006

[ref. 2.2] - Improved Emission Efficiency of 210-nm Deep-ultraviolet Aluminum Nitride Light-emitting Diode - Yoshitaka Taniyasu† and Makoto Kasu, www.ntt-review.jp

[ref. 3.1] - Fabrication of GaN cantilevers on silicon substrates for microelectromechanical devices - S. Davies, T. S. Huang, M. H. Gass, A. J. Papworth, T. B. Joyce, and P. R. Chalker – Appl. Phys. Lett. 84, 2566 (2004)

[ref. 3.2] - GaN on Patterned Silicon (GPS) Technique for GaN-based Integrated Microsensors - Zhenchuan Yang, Ruonan Wang, Deliang Wang, Baoshun Zhang, Kevin J. Chen, and Kei May Lau - 0-7803-9269-8 2005 IEEE

[ref. 4.1] - Giordano, Nicholas (2009). College Physics: Reasoning and Relationships. Cengage Learning. pp. 421–424. ISBN 0534424716.

[ref. 5.1] - David I. G. Jones (2001). Handbook of Viscoelastic Vibration Damping. ISBN: 978-0-471-49248-1